



저작자표시-비영리-변경금지 2.0 대한민국

이용자는 아래의 조건을 따르는 경우에 한하여 자유롭게

- 이 저작물을 복제, 배포, 전송, 전시, 공연 및 방송할 수 있습니다.

다음과 같은 조건을 따라야 합니다:



저작자표시. 귀하는 원저작자를 표시하여야 합니다.



비영리. 귀하는 이 저작물을 영리 목적으로 이용할 수 없습니다.



변경금지. 귀하는 이 저작물을 개작, 변형 또는 가공할 수 없습니다.

- 귀하는, 이 저작물의 재이용이나 배포의 경우, 이 저작물에 적용된 이용허락조건을 명확하게 나타내어야 합니다.
- 저작권자로부터 별도의 허가를 받으면 이러한 조건들은 적용되지 않습니다.

저작권법에 따른 이용자의 권리는 위의 내용에 의하여 영향을 받지 않습니다.

이것은 [이용허락규약\(Legal Code\)](#)을 이해하기 쉽게 요약한 것입니다.

[Disclaimer](#)

공학박사학위논문

**고에너지 물질의 파이로테크닉 연소
모사를 위한 충격-폭발 천이 현상 해석**

**Hydrodynamic analysis on shock to detonation
transition aimed at characterizing pyrotechnic
combustion of energetic materials**

2017년 2월

서울대학교 대학원

기계항공공학부

김 보 훈

Abstract

Hydrodynamic Analysis on Shock to Detonation Transition aimed at Characterizing Pyrotechnic Combustion of Energetic Materials

Bohoon Kim

Mechanical and Aerospace Engineering

The Graduate School

Seoul National University

An accurate and reliable prediction of reactive flow is a challenging task when characterizing an energetic material subjected to an external shock impact as the detonation transition time is on the order of a micro second. The present study aims at investigating the size effect behavior of a heavily aluminized cyclotrimethylene-trinitramine (RDX) which contains 35% of aluminum by using a detonation rate model that includes ignition and growth mechanisms for shock initiation and subsequent detonation. A series of unconfined rate stick tests and two-dimensional hydrodynamic simulations are conducted to construct the size effect curve which represents the relationship between detonation velocity and inverse radius of the charge.

A sympathetic detonation (SD) is a detonation of an explosive charge by a nearby explosion. Most of times it is unintended while the impact of blast

fragments or strong shock waves from the initiating donor explosive is the cause of SD. We investigate the SD of a cylindrical explosive charge (64% RDX, 20% Al, 16% HTPB) contained in a steel casing. The constitutive relations for high explosive are obtained from a thermo-chemical code that provides the size effect data without the rate stick data typically used for building the rate law and equation of state. A full size SD test of eight pallet-packaged artillery shells is performed that provides the pressure data while the hydrodynamic model with proper constitutive relations for reactive materials and the fragmentation model for steel casing is conducted to replicate the experimental findings. The work presents a novel effort to accurately model and reproduce the sympathetic detonation event with a reduced experimental effort.

A pyrotechnic system consisting of donor/acceptor pair separated by a gap relies on shock attenuation characteristics of the gap material and shock sensitivity of the donor and acceptor charges. Despite of its common use, numerical study of such pyrotechnic train configuration is seldom reported because proper modeling of the full process requires precise capturing of the shock wave attenuation in the gap prior to triggering a full detonation of high explosive and accurate description of the high strain rate dynamics of the explosively loaded inert confinements. We apply a hybrid particle level-set based multimaterial hydrocode with reactive flow models for pentolite donor and heavily aluminized RDX as acceptor charge. The complex shock

interaction, critical gap thickness, acoustic impedance, and Go / No-go characteristics of the pyrotechnic system are quantitatively investigated.

A full scale hydrodynamic simulation which necessary to accurately reproduce shock-induced detonation is conducted to analyze the reacting flow of an energetic component system. An explosive train configuration composed of donor (HNS+HMX) / bulkhead (STS) / acceptor (RDX) / pyrotechnic propellant (BKNO3) was considered to measure the release pressure wave into 10 cc enclosed chamber for quantifying the inherent oscillatory flow induced by the interferences between shock and rarefaction waves. The pressure fluctuation measured from experiment and calculation was investigated to further validate a peculiar peak at a specific characteristic frequency ($\omega_c = 8.3$ kHz) representing intrinsic oscillation in the chamber. Since the present methodology for analyzing the energetic component system involving detonation of high explosives, deflagration of propellant, and deformation of confinement system is quite straight forward, one needs to properly implement the outlined formulation into a shock physics code for a full scale hydrodynamic simulation involving such energetic components.

***Keywords:* Hydrodynamics, Shock-to-detonation transition, Energetic materials, Rate stick, Size effect, Detonation model, Gap test, Critical thickness, Shock sensitivity, Attenuation, Pyrotechnics, Closed bomb test**

Student Number: 2012-30168

LIST

ABSTRACT.....	i
LIST.....	iv
LIST OF FIGURES.....	vi
LIST OF TABLES.....	xii
PREFACE.....	xiii
CHAPTER 1	
INTRODUCTION.....	1
CHAPTER 2	
A REACTIVE FLOW MODEL FOR ENERGETIC MATERIALS.....	7
2.1 Background and objective.....	7
2.2 Unconfined rate stick tests.....	8
2.3 A reactive flow model.....	11
2.4 Rate stick simulation.....	19
2.5 Conclusion.....	28
CHAPTER 3	
SIMULATING SYMPATHETIC DETONATION.....	29
3.1 Background and objective.....	29
3.2 Sympathetic detonation test.....	32

3.3 Methods and mathematical formulation.....	34
3.4 Results and discussions.....	48
3.5 Conclusion.....	63
CHAPTER 4	
ANALYSIS ON SHOCK ATTENUATION IN GAP TEST.....	64
4.1 Background and objective.....	64
4.2 Numerical approach.....	65
4.3 Modeling constants.....	74
4.4 Results and validations.....	76
4.5 Conclusion.....	95
CHAPTER 5	
PYROTECHNIC COMBUSTION IN CLOSED BOMB CHAMBER.....	96
5.1 Background and objective.....	96
5.2 Numerical approach.....	102
5.3 Results and validations.....	127
5.4 Conclusion.....	156
CHAPTER 6	
CONCLUSION.....	158
REFERENCES.....	161

LIST OF FIGURES

Fig. 2.1 A rate stick packed in a cylindrical mono-cast Nylon tube.....	9
Fig. 2.2 Captured position versus trigger time plotted for a 30 mm diameter case (m : the slope between each pin, $m_{15}=7.09$).....	10
Fig. 2.3 Computational domain of a 2-D cylindrical duct for unconfined rate stick simulation.....	22
Fig. 2.4 Convergence of detonation wave front shown with grid resolution.....	23
Fig. 2.5 Structure of detonation wave representing the reaction zone of heavily aluminized RDX.....	24
Fig. 2.6 Density contours for unconfined rate stick simulation of 0 (top), 0.075 mm ⁻¹ (middle), and 0.125 mm ⁻¹ (bottom) inverse radius cases with density range 0.1~2.4 g/cc.....	25
Fig. 2.7 Propagation of detonation front in 0 and 0.125 mm ⁻¹ unconfined rate sticks.....	26
Fig. 2.8 Size effect curve for the unconfined rate stick tests for heavily aluminized RDX.....	27
Fig. 3.1 Stacked high explosives for sympathetic detonation showing (a) initial configuration, (b) donor casing impacting neighbors after donor initiation, (c) fragmentation and subsequent chain initiation.....	30

Fig. 3.2 Experimental setup of sympathetic detonation of pallet-packaged 155 mm shell.....	33
Fig. 3.3 JWL pressure profiles of unreacted and reacted EOS with respect to the relative volume	39
Fig. 3.4 Density contours for the unconfined rate stick of PBXN-109 at $t=12.5 \mu\text{s}$ with density range 0.1-2.5 g/cc.....	41
Fig. 3.5 Size effect curves for the unconfined rate stick of PBXN-109.....	42
Fig. 3.6 Time trace of product and reactant mass fraction of PBXN-109.....	42
Fig. 3.7 Mott distribution for varying the values of $\gamma=3, 5, 10, 50$	48
Fig. 3.8 Computational setup for eight pallet sympathetic detonation: 8 lives / 3 lives + 5 mockups.....	50
Fig. 3.9 Pressure contours of sympathetic detonation with 8 live rounds. Detonation wave propagation of PBXN-109 and effective plastic strain in the AISI 9260 are shown at (a) $t_1=90 \mu\text{s}$, (b) $t_2=120 \mu\text{s}$, and (c) $t_3=160 \mu\text{s}$ with pressure range 0-0.05 Mbar for PBXN-109 and strain range 0-1 for AISI 9260.....	51
Fig. 3.10 Pressure contours of sympathetic detonation with 3 lives + 5 mockups. Detonation wave propagation of PBXN-109 are shown at (a) $t_1=90 \mu\text{s}$, (b) $t_2=120 \mu\text{s}$, and (c) $t_3=160 \mu\text{s}$ after initiation with pressure range 0-0.05 Mbar for PBXN-109 and strain range 0-1 for AISI 9260.....	51
Fig. 3.11 Initiation process induced by shock-metal impact with three different contours and times for PBXN-109. (a) Burned mass fraction range 0-1.0, (b)	

Density range 0-2.0 g/cm ³ , and (c) Pressure range 0-5.0 GPa at 6.0 μs, 60.0 μs, and 120.0 μs.....	52
Fig. 3.12 Time trace of measured pressure profiles at (a) 15 m and (b) 20 m distance probes.....	55
Fig. 3.13 Comparison of calculated broken pieces of AISI 9260 casing with collected fragments	57
Fig. 3.14 3D computational geometry of 155 mm cased high-explosive.....	58
Fig. 3.15 Time sequence of fragmentation process and created broken pieces of AISI 9260 case of 155 mm artillery shell	59
Fig. 3.16 Time history of expansion velocities of AISI 9260 in microsecond scale.....	61
Fig. 3.17 Number of fragments recorded with respect to time	61
Fig. 3.18 Histogram of AISI 9260 fragment masses in fragmentation simulation	62
Fig. 3.19 Time history of kinetic energy of AISI 9260 casing in KJ.....	62
Fig. 4.1 Calculated shock pressure attenuation in Pentolite(donor)-PMMA(gap).....	76
Fig. 4.2 Calculated results for Gap-Acceptor configuration at 6 μs: (a) density, (b) velocity, and (c) pressure.....	80
Fig 4.3. Mesh refinement test via particle velocity.....	81
Fig 4.4 Gap test configuration	82
Fig. 4.5 Shown reaction progress and pressure for donor (bottom)/acceptor	

(top), density for PMMA (middle). (a) 25 mm Gap and (b) 26 mm Gap at times $t = 7, 8, 10, 12, 13,$ and $15 \mu\text{s}$	84
Fig. 4.6 Shape evolution of PMMA during shock attenuation: (a) Initial PMMA thickness of 25 mm and (b) Initial PMMA thickness of 26 mm at times 8, 14, 20, and $26 \mu\text{s}$	87
Fig. 4.7 Time trace of consecutive pressure profiles of LSGT simulation with 25 mm and 26 mm gap thickness	88
Fig. 4.8 Jump in the acoustic impedances.....	89
Fig. 4.9 Pressure and acoustic impedance of LSGT configuration (Donor, Gap, Acceptor).....	92
Fig. 4.5 Timed images of acoustic impedance ($Z = \rho c$) at Go case of LSGT simulation at times $t = 10, 15, 20, 25,$ and $30 \mu\text{s}$	94
Fig. 5.1 Reaction rate profile for BKNO3's burning based on Arrhenius law with temperature rise	125
Fig. 5.2 SEM images in several length scale for particle size analysis.....	129
Fig. 5.3 Small scale gap test configuration.....	129
Fig. 5.4 Go (broken) and No-go (preserved) results of small scale gap test.....	130
Fig. 5.5 Shown reaction progress for donor (top) and acceptor (bottom), pressure and density for PMMA (middle) and BRASS (both shides). (a) 11 mm Gap and (b) 12 mm Gap at times $t = 2.0, 3.5, 7.0, 9.0, 10.0,$ and $11.0 \mu\text{s}$	134

Fig. 5.6 Time trace of attenuating pressure profiles through PMMA gap of SSGT simulation.....	135
Fig. 5.7 Configuration of an explosive train used in the pyrotechnic initiator (HNS+HMX - STS - Al-RDX).....	137
Fig. 5.8 Simulated results for Go and No-go events in a pyrotechnic device.....	139
Fig. 5.9 Hugoniot curve for STS-304 in the p-p plane from calculation and experiment.....	140
Fig. 5.10 Shock pressure trajectory in detonator-bulkhead-acceptor of pyrotechnic initiator.....	140
Fig. 5.11 Test specimen (upper) and computational domain (lower) for closed bomb test	142
Fig. 5.12 CBT chamber pressure histories for Go / No-go reaction	145
Fig. 5.13 Measured raw and filtered pressure profiles.....	145
Fig. 5.14 Power spectral densities of closed bomb test data.....	146
Fig. 5.15 Timed images of pressure contour at 3.8 mm (left), and 4.0 mm (right) bulkhead thickness of the explosive train configuration.....	148
Fig. 5.16 Shock pressure trajectory in donor / bulkhead / acceptor of the explosive train configuration.....	149
Fig. 5.17 Shock impedance matching of STS and RDX.....	149
Fig. 5.18 Shown schlieren (top) and pressure (bottom) fields for entire PMD-chamber assembly that shows the detonator (HNS+HMX), bulkhead (STS),	

acceptor (RDX), and propellant (BKNO3). Right lower corner is a cross cut of the actual device after single use for comparison with numerical prediction of deformed boundaries.....153

Fig. 5.19 Shape comparison of deformed boundaries of STS with zero level-set lines.....155

Fig. 5.20 Comparison of pressure fluctuation between test and calculation in closed bomb chamber155

LIST OF TABLES

Table 2.1 Comparison of the pressure sensitivity of selective energetic materials.....	18
Table 2.2 Equation of state coefficients and rate law parameters for the heavily aluminized RDX.....	18
Table 2.3 Chapman-Jouguet values of the heavily aluminized RDX.....	21
Table 2.4 Comparison of the fully developed detonation velocity for different charge radius.....	28
Table 3.1 Chapman-Jouguet conditions for PBXN-109.....	38
Table 3.2 Modeling parameters of constitutive relations for PBXN-109.....	49
Table 3.3 Modeling constants for AISI 9260.....	49
Table 4.1 Material properties for PMMA.....	75
Table 4.2 Modeling constants for Pentolite and heavily aluminized RDX.....	75
Table 4.3 Comparison of shock attenuation.....	77
Table 4.4 Initial parameters for a gap-acceptor problem.....	78
Table 4.5 LSGT experimental result.....	83
Table 5.1 C-J conditions for HNS, HMX, RDX, and BKNO ₃	120
Table 5.2 Material properties for PMMA, STS, and BRASS.....	122
Table 5.3 Modeling constants for HNS, HMX, RDX, and BKNO ₃	126
Table 5.4 SSGT experimental result.....	131
Table 5.5 SSGT results for 97.5% RDX.....	136
Table 5.6 Closed bomb test result.....	143

PREFACE

This thesis is based on the following publications and manuscripts.

Chapter 2

B. Kim, J. Park, K. Lee and J.J. Yoh, "A reactive flow model for heavily aluminized cyclotrimethylene-trinitramine," *Journal of Applied Physics*, Vol. 116, 023512, 2014.

Chapter 3

B. Kim, M. Kim, T. Sun and J.J. Yoh, "Simulating sympathetic detonation using the hydrodynamic models and constitutive equations," *Journal of Mechanical Science and Technology*, Vol. 30, No. 12, 2016.

Chapter 4

B. Kim, J. Park and J.J. Yoh, "Analysis on shock attenuation in gap test configuration for characterizing energetic materials," *Journal of Applied Physics*, Vol. 119, 145902, 2016.

B. Kim, M. Kim and J.J. Yoh, "Shock to detonation transition analysis using experiments and models," *Proceedings of the Combustion Institute*, 2016.

Chapter 5

B. Kim, M. Kim and J.J. Yoh, "Shock to detonation transition analysis using experiments and models," *Proceedings of the Combustion Institute*, 2016.

B. Kim, S. Jang and J.J. Yoh, "Hydrodynamic simulation of energetic materials in a train configuration," *Journal of Computational Physics*, (in preparation).

The chapters are reproduced with permission of the co-authors and the publishers.

CHAPTER 1

INTRODUCTION

An energetic material is a reactive source of high amount of stored chemical energy that can be released, usually accompanied by the production of high temperature and high pressure. It can breakdown very quickly to generate the blast power because a complex compound composed of the fuel (e.g. carbon or hydrogen) and the oxidizing agent (e.g. oxygen) in the molecular structure of the explosives. It is converted from the chemical enthalpy to the pressure and thermal energy dramatically when external shock is applied. So, the energetic materials are used mostly in the systems that require a large force for a very short time such as explosives (bombs, mines), propellants (rocket motors), pyrotechnic compositions (gas generators), and fuels.

Explosive materials may be categorized by the speed at which they expand. Materials that detonate (the front of the chemical reaction moves faster through the material than the speed of sound) are said to be "high explosives" and materials that deflagrate are said to be "low explosives". Explosives may also be categorized by their sensitivity. Sensitive materials that can be initiated by a relatively small amount of heat or pressure are primary explosives and materials that are relatively insensitive are secondary or

tertiary explosives. Therefore, it is important to understand the physical phenomena of ignition sensitivity and flame development of explosives.

In general, the shock-induced reaction can be classified to be either low-order explosion (deflagration) or high-order explosion (detonation). The shock to detonation transition (SDT) within a short time scale ($\sim 10^{-5}$ sec) is observed in the chemical reactions of an energetic material subjected to an external shock impact. The rate of reaction of certain high explosives and solid propellants under a deflagration to detonation transition (DDT) is normally slower than SDT phenomena, being approximately $10^{-3}\sim 10^{-2}$ sec. Since in most SDT events, the response time for high explosives to undergo any sort of thermal response such as dissociation or dissipation is slow. Instead, the pressure dependence of initiation is most dominant in the developing detonation waves observed in the impact initiated detonation phenomena.

Examples of major explosive compositions to be addressed in this study are RDX (cyclotrimethylene-trinitramine, $C_3H_6N_6O_6$) and HMX (cyclotetramethylene-tetranitramine, $C_4H_8N_8O_8$). RDX and HMX can be used in their pure form, but most explosives require mechanical properties, not pure. The energetic materials are often mixed with other (generally) inert materials. For example, an energetic material containing more than 30% of aluminum is used as a multipurpose explosive requiring the large blast effect and high pressure environment. Thermobarics is a type of explosive that

utilizes additional ingredient (e.g. aluminum, boron) to generate an intense, high-temperature explosion, and in practice the blast wave typically produced by such a weapon is of a significantly longer duration than a conventional condensed explosive. Thus, the aluminized high explosives are an effectual means to increase brisance effect which is the shattering capability based on not only 1st detonation of explosive substances but also 2nd burning of Al. For this reason, an explosive manufactured with a massive Al element becomes the latest trend in the defense industry.

To determine the suitability of an explosive substance for a particular use, its physical properties must first be known. The usefulness of an explosive can only be appreciated when the properties and the factors affecting them are fully understood. There are a variety of methods for the initiation of explosives, including heat, shock impact, electrostatic impulse, friction, mechanical insult, or any combination of these energy inputs. (This study is limited to the shock-induced initiation to analyze the shock-to-detonation transition phenomena.) Various experiments are routinely performed to understand the ignition or initiation of explosives subjected to a shock impact. Although experiments provide valuable information on the reaction behavior and shock sensitivity of explosives, many tests have not provided much insight into the basic physicochemical processes such as sensitivity to initiation, velocity of detonation, blast effect, pressure of products of explosion, and oxygen balance. Because of the high costs and safety bounds

for the experiment, there is a growing demand for the development of computational methods of shock initiation to provide both an understanding and predictive capability.

For numerically capturing of such SDT event that is dominantly pressure sensitive, Lee-Tarver model[1] and JWL++(Jones-Wilkins-Lee++) model[2] have been widely in use. Lee-Tarver considers generation of hotspots and their effect on initiation, and it consists of the equations of states for both product and reactant. The model requires predetermination of excessive number of parameters (12 unknowns) to both empirically and ad hoc, making it difficult to be universal for a general energetic material. JWL++ model shows simplification to Lee-Tarver, neglecting the initiation step and using only a single growth step for detonating explosive. Despite the need for better model that combines the strengths of these approaches, methodology to determine the unknowns of such SDT rate laws has yet been accomplished to date. Further the present state of free parameter determination in the context of either Lee-Tarver or JWL++ is cumbersome and quite qualitative. The present study aims at developing an improved reactive flow model including both ignition and growth steps of a detonation transition due to mechanical (pressure) stimulus. The suggested model can overcome certain limitations of aforementioned models for SDT simulation. In addition, the free unknown parameters of the model are analyzed theoretically for minimizing ambiguity

of numerical iterations. The procedure involves quantitative and accurate determination of the model parameters.

The reactive flow models of SDT must be combined into a proper shock physics program called hydrocodes [3] to allow calculation of the dynamic response of explosives subjected to an external shock impact. Hydrocodes are programs that use a variety of solution techniques to solve time-dependent, non-linear hyperbolic problems in solid, and gas dynamics. Calculation of hydrocodes generally requires a large number of meshes through the reactive area of the explosive to solve the sharp detonation structures and ZND to CJ properties. SDT model is very mesh-time intensive because thousands of m/s in velocity and tens of GPa in pressure are generated within the width of the reaction zones of RDX and HMX which are very small, ~ 0.1 mm for HMX-based explosives and ~ 0.5 mm for RDX-based explosives. A pressure-based detonation model aimed at accurately simulating the detonation response of high explosives and propellants subjected to an external impact are proposed. In addition, physical approach for determining the free parameters of a KYP model is explained. The proposed burn rate model preserves physical meaning of the conservation law, and has its potential to overcome limitations set by other reactive flow models. The present analysis also describes a useful means for pre-determining four unknowns of the model before engaging the rate model into a full hydrocode for a direct numerical simulation of the complex SDT phenomena.

The present study aims at developing a new reactive flow model that includes ignition and growth mechanisms for detonating energetic materials. The suggested model is shown to overcome certain limitations of the existing models while free parameters of the model are determined based on theoretical means. The pressure sensitivity parameters associated with explosive growth phase of a list of high explosives are carefully calibrated to enhance the accuracy of the proposed model. And it is applied to several SDT problems:

- Rate stick test
- Sympathetic detonation
- Large-scale gap test
- Small-scale gap test
- Pyrotechnic combustion
- Closed bomb test

CHAPTER 2

A Reactive Flow Model for Energetic Materials

2.1 Background and objective

We characterize a multi-purpose high explosive which is comprised of 50 % RDX (cyclotrimethylene-trinitramine, $C_3H_6N_6O_6$) and 35 % aluminum powder with 15 % HTPB (hydroxyl-terminated polybutadiene) binder, and its initial density after pressing is 1.78 g/cc. To simulate the shock-to-detonation transition (SDT) that is dominantly driven by pressure, Lee-Tarver [1] and JWL++ (Jones-Wilkins-Lee++) [2] models are used in general. Lee-Tarver considers generation of hotspots and their effect during initiation. The model requires predetermination of parameters both empirically and ad hoc, making it difficult to be universal for generalized energetic material. The JWL++ model offers simplification to [1] by ignoring the initiation step and using only the single growth step for a detonating explosive. The methodology to determine model parameters are somewhat qualitative, and the reactive flow model would need to be recalibrated each time a new explosive is formulated. Once calibrated for one explosive, it does not manifest as to how to change the unknown parameters for other explosives.

Souers *et al.* [3] provided a useful approach to determine the unknown parameters of JWL++ model. They provided an analytical approach that

allows prediction of the rate constants in terms of the size effect measurements. The method is restricted to a growth step only, and an empirical fit to a diameter effect is required to constrain unknown parameters, indicating that there are still additional unknowns to be determined.

The present study aims at developing a modified reactive flow model that includes both ignition and growth steps while attempting to overcome limitations of aforementioned JWL++ model. In addition, the unknown parameters are handled theoretically to minimize ambiguity of the numerical iterations. In order to validate the reactive flow response of a heavily aluminized RDX, the unconfined rate stick tests have been carried out.

2.2 Unconfined rate stick test

A series of unconfined rate stick tests for heavily aluminized RDX is performed, where the detonation velocities were measured as a function of cylindrical charge diameter. The steady detonation wave is observed by utilizing a charge length sufficiently long enough to damp out any booster overdrive or initiation transients which can persist for up to five times the charge diameter. A charge length-to-diameter ratio of 10 is chosen to adequately capture the fully developed detonation velocities in all tests.

The samples are prepared by compacting the heavily aluminized RDX into a precisely machined mono-cast Nylon. Electronic pins were utilized for measurement of the propagation velocity of detonation wave. If the installed

pin is exposed to a high temperature-pressure shock wave, the pin breaks and signal generator transmits a signal. Then a high speed counter, a Time-to-Digital Converter (TDC) measures the arrival time of the shock wave, sensing an ascending (or descending) waveform of input pulses. We used pin CA-1041 (DYNASEN Inc.) and a high speed counter Lec-4208 (LeCroy Inc.) as the wide range real-time TDC. The TDC is designed to cover the time measurements performed in real time, and requiring a wide dynamic range with high resolution.

A rate stick packed in a cylindrical mono-cast Nylon of 90 mm diameter is shown in Fig. 2.1. 16 different diameters used were 13.5 mm, 14.0 mm, 15.0 mm, 16.0 mm, 17.0 mm, 18.0 mm, 20.0 mm, 25.0 mm, 30.0 mm, 35.0 mm, 40.0 mm, 45.0 mm, 50.0 mm, 70.0 mm, 90.0 mm, and 110.0 mm. We considered a wide range of diameters to secure enough data to establish the size effect behavior of heavily aluminized RDX.

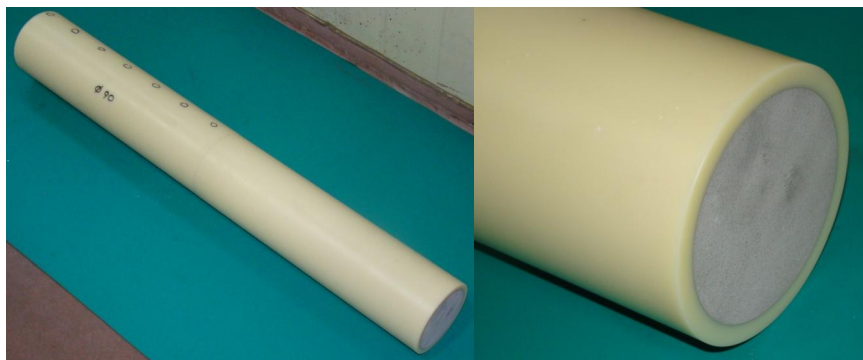


Fig. 2.2 A rate stick packed in a cylindrical mono-cast Nylon tube.

The propagation of the detonation front along the length of each charge was measured using 5 equally spaced sensor probes. The TDC with a bandwidth of 1 GHz or frequency resolution of 1 ns (10^{-9} sec) was used during each test. The measured probe data for 30 mm diameter test is shown on a plot of probe position versus trigger time in Fig. 2.2. The time-distance diagram proves that all initiation transients have in fact dampened and that the self-sustained propagation velocity is constant by the end of a charge with $L/D = 10$ because the time dependent slope of the pin position is steadily maintained. The probe data minimizing the influence of initiation transients were used to get a fully developed detonation velocity.

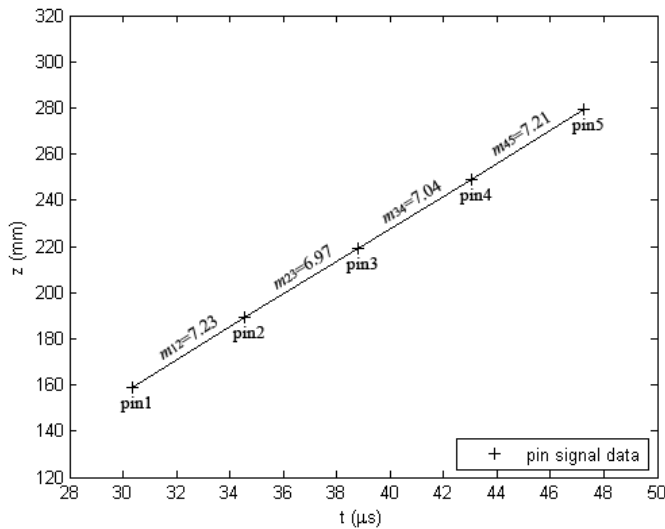


Fig. 2.2 Captured position versus trigger time plotted for a 30 mm diameter case (m : the slope between each pin, $m_{15}=7.09$)

The chemical kinetic information comes from the size effect data where the change in steady state or fully developed detonation velocity, U_s , is given in terms of radius, R_0 . The detonation velocity is plotted as a function of the inverse radius, $1/R_0$, and the curve is extrapolated back to zero to obtain the infinite radius detonation velocity, D .

2.3 A reactive flow model

The rate of product mass fraction consists of ignition and growth terms [4] such that

$$\frac{d\lambda}{dt} = I(1-\lambda)^b (\eta - a)^x + G_1(1-\lambda)^c \lambda^d P^y + G_2(1-\lambda)^e \lambda^g P^z, \quad \eta = \frac{\rho}{\rho_0} - 1 \quad (1)$$

Here λ is the burned mass fraction, and constants $I, b, a, x, G_1, c, d, y, G_2, e, g, z$ are the unknown parameters. λ is reaction progress variable ($\lambda = 0$ unreacted state and $\lambda = 1$ reacted state). P is the pressure, t is time, ρ_0 and ρ are the initial and current densities, respectively. The Mie-Gruneisen EOS [5] in Eq. (2) is for the unreacted solid HE, and the isentropic JWL EOS [6] in Eq. (3) is used for the reacted gaseous product.

$$P_{unreacted} = P_H + \Gamma \rho (e - e_H) \quad (2)$$

$$P_{reacted} = A e^{-R_1(\rho_0/\rho)} + B e^{-R_2(\rho_0/\rho)} + C (\rho_0/\rho)^{-(1+\omega)} \quad (3)$$

Here P_H , e_H are pressure and internal energy of a reference state that follows the Hugoniot curve, and Γ is the Gruneisen gamma. P_H and e_H can be expressed as follows:

$$P_H = C_0^2 \left(\frac{1}{\rho_0} - \frac{1}{\rho} \right) / \left[\frac{1}{\rho_0} - S \left(\frac{1}{\rho_0} - \frac{1}{\rho} \right) \right]^2 \quad (4)$$

$$e_H = C_0^2 \left(\frac{1}{\rho_0} - \frac{1}{\rho} \right)^2 / 2 \left[\frac{1}{\rho_0} - S \left(\frac{1}{\rho_0} - \frac{1}{\rho} \right) \right]^2 \quad (5)$$

C_0 , S are the bulk sound speed and linear Hugoniot slope coefficient, respectively. Also the shock speed relations are

$$S = dU_{shock} / dU_{particle} \quad (6)$$

$$C_0 = (\partial P / \partial \rho)^{1/2} \quad (7)$$

$$U_{shock} = C_0 + S U_{particle} \quad (8)$$

where U_{shock} is the shock wave velocity, $U_{particle}$ is the material particle velocity.

A , B , C , R_1 , R_2 are the material dependent JWL parameters with ω being the Gruneisen coefficient of Eq. (3). Equations (2) and (3) are combined into a single expression Eq. (9) using the product mass fraction (λ) and reactant depletion ($1-\lambda$). And standard mixture rule applies to the internal energy and volume ratio such as

$$P_{total} = (1 - \lambda)P_{unreacted} + \lambda P_{reacted} \quad (9)$$

$$e_{total} = (1 - \lambda)e_{unreacted} + \lambda e_{reacted} \quad (10)$$

$$v_{total} = (1 - \lambda)v_{unreacted} + \lambda v_{reacted} \quad (11)$$

The Lee-Tarver model is comprised of *i*) ignition term that represents formation of the hotspots by the rapid compression, and *ii*) first growth term that describes the effect of the propagation of the reacting waves in the substance and second growth term that represents completion due to a detonation transition. For determination of 12 unknowns here, a curve fitting method with optimization technique is usually needed.

If the ignition term involving the initial density ratio is omitted, a JWL++ model [2] is generally recovered, and its simple form is

$$\frac{d\lambda}{dt} = G(1 - \lambda)(P + Q)^b \quad (12)$$

Here G is growth constant, b is pressure sensitivity, and Q is artificial viscosity. The determination of the unknowns is relatively easier and thus the usability of a simplified form of the rate law is greater if the process is mostly growth dependent.

An alternative to these two limiting forms of the reactive flow equation can be casted into a following form such that

$$\frac{d\lambda}{dt} = I(1-\lambda)\eta^a + G(1-\lambda)P^b, \quad \eta = \frac{\rho}{\rho_0} - 1 \quad (13)$$

Here, the model resembles a full Lee-Tarver, but it now includes an initiation step which is missing in JWL++. Four unknown parameters having the major significance in view of detonation are kept, namely I , a , G , b .

The initiation step requires defining the ignition constant, I , while the reactant depletion $(1-\lambda)$ is time-resolved in the governing equation with a compression $\eta = \rho/\rho_0 - 1$. The ignition of high explosive occurs by compression because of the shock wave propagation. Hotspots are formed in a shocked high explosive, leading to a void collapse. Any void or gas bubble that exists in high explosives may provide a potential site for local adiabatic compression that leads to the localized heating well beyond the activation energy for detonation.

Wackerle *et al.* [7, 8] reported that hotspot formation due to void collapse depends on the shock pressure, P_s , and the reaction rate is proportional to P^2 which is known experimentally. To investigate the shock-pressure-squared dependence of ignition, compression sensitivity, a , must be set to 4 because the relationship between pressure and density is parabolic based on the Rankine-Hugoniot argument. Once again, the pressure squared term is dominant in the shock induced ignition, and the pressure is proportional to compression squared. As such the compression sensitivity being 4 is the best choice for most of the SDT problems.

Souers *et al.* [3] provided a useful approach to determine the unknown parameters of JWLL++ model. They analytically linked the growth term with the unconfined rate stick data. The rate stick test provides detonation velocity versus the inverse radius of a cylindrical charge. With such size effect information, the unknowns of the growth term are determined. That is, the relationship between non-dimensional detonation velocity and a non-dimensional inverse radius is derived using a detonation velocity equation of unconfined rate stick following Eyring *et al.* [9] as

$$\frac{U_s}{D} = 1 - \left(0.4 / \left[1 - (U_s/D)^2 \right]^{0.8} \right)^{-1} \frac{t_e U_s}{R_0} \quad (14)$$

where U_s is the detonation velocity for radius R_0 , and D is the detonation velocity at infinite radius. t_e is the time to cross the reaction zone during which Eq. (14) is valid.

Now all λ 's are collected on the left of the growth term in Eq. (13) and the equation is integrated such that,

$$\int \frac{1}{(1-\lambda)} d\lambda = \int GP^b dt \quad \rightarrow \quad -\ln(1-\lambda) = GP^b t_e \quad (15)$$

Finally, Eq. (16) specifies the relationship between dimensionless detonation velocity and the charge inverse radius.

$$\frac{R_D}{R_0} = -\frac{0.4 \left[1 - (U_s/D)^2 \right]^{-0.8}}{\ln \left(1 - (U_s/D)^2 \right)} \left(\frac{U_s}{D} \right)^{2b-1} \left(1 - \frac{U_s}{D} \right) \quad (16)$$

The non-dimensional and generalized radius (R_D) and growth constant (G) are given by

$$R_D = D(GP^b)^{-1}, \quad G = D(R_D P^b)^{-1} \quad (17)$$

This means that the Eyring equation can be expressed in terms of the detonation velocity and the charge size, defined through a pressure term b such that the size effect can be derived by changing the value b in Eq. (16).

The curve fitting procedure for a heavily aluminized RDX is performed to determine the pressure sensitivity term, b . The optimal size effect curve of the analytical solution is drawn based on the pressure sensitivity set to $b=0.7$ with maximum detonation velocity at zero inverse radius being 7.387 mm/ μ s, and the generalized radius equals 0.75 mm. The analytical line which is an optimal fit is characteristically high for $R_D/R_0 < 0.05$ and low for $0.05 < R_D/R_0 < 0.12$.

Now the Ignition constant is defined by the ratio of ignition to growth, namely,

$$\left. \frac{d\lambda}{dt_I} \right|_{\text{Ignition}} = I(1-\lambda)\eta^a, \quad \left. \frac{d\lambda}{dt_G} \right|_{\text{Growth}} = G(1-\lambda)P^b \quad (18)$$

Here t_I , t_G are the total time for completion. The dimensionless IG takes the form,

$$IG = \frac{I\eta^a}{GP^b} \sim 0.1 \quad \text{or} \quad I \cong 0.1GP^b\eta^{-a} \quad (19)$$

where the four parameters (I , a , G , b) decide the intrinsic characteristics of initiation and detonation. By assigning 0.1 to this number, ignition constant I can be calculated from Eq. (19), suggesting that 10% of the full reaction time is spent for growth. Thus if IG is zero, the model reduces to a JWL++ rate law where the rapid growth step is of only relevance in the reactive flow process.

The constants of ignition I and growth G are set to $3.177 \times 10^8 \text{ s}^{-1}$ and $0.7045 \text{ s}^{-1} \text{ Pa}^{-b}$, respectively. The pressure sensitivity of the explosive is 0.7, and the compression sensitivity is 4. Table 2.1 shows comparison of the pressure sensitivity values and the literature values. The sensitivity of each energetic material was derived by the theoretical argument without any speculations based on numerical trials which is an improvement from the earlier reactive flow models.

Table 2.1 Comparison of the pressure sensitivity of selective energetic materials.

Energetic materials	Pressure sensitivity	
	<i>b</i> - Present	<i>b</i> - Others
LX-17	1.7	0.67[10]
ANFO-K1	1.38	1.3[11]
ANFO emulsion with 30% HMX	1.7	1.5[12]
Creamed TNT	1.0	1.75[12]
Urea nitrate (0.69 g/cm ³)	1.0	1.0[12]
HANFO	0.95	0.8[3]
TNT	1.0	...
HMX emulsion	1.7	...
Non-ideal AN emulsion k1a	1.45	1.5[3]
Extremely non-ideal AN	0.8	0.8[3]
ANFO prill	1.65	1.5[3]
Potassium chlorate/sugar	1.05	0.8[3]

Table 2.2 Equation of state coefficients and rate law parameters for the heavily aluminized RDX.

	Model parameter	Value
Reactant	C_0 (mm/ μ s)	2.60
	S	1.86
	Γ	0.99
Product	A (GPa)	2633
	B (GPa)	8.59
	C (GPa)	1.09
	R_1	6.68
	R_2	1.11
	ω (J/g-K)	0.09
Chemical kinetics	I (s ⁻¹)	3.18×10^8
	a	4.0
	G (s ⁻¹ Mbar ^{-b})	3.53×10^7
	b	0.7

2.4 Rate stick simulation

The multi-material numerical simulation of shock-to-detonation transition is conducted with a hydrocode [13]. A level-set based reactive Ghost Fluid Method (GFM) that imposes exact boundary conditions at material interfaces is developed to reproduce the experimental size effect data of the unconfined rate stick tests.

The conservative laws of mass, momentum, and energy equations in two-dimensional axisymmetric coordinate are defined by

$$\frac{\partial \vec{U}}{\partial t} + \frac{\partial \vec{E}}{\partial z} + \frac{\partial \vec{F}}{\partial r} = \vec{S}(\vec{U}) \quad (20)$$

where the vectors represent the conservative variables U , spatial fluxes in axial and radial directions E and F and the source term S that represents a variety of multi-material loading conditions. In the Eulerian form, each vector is given as follows

$$\vec{U} = \begin{bmatrix} \rho \\ \rho u_z \\ \rho u_r \\ \rho E \end{bmatrix} \quad \vec{E} = \begin{bmatrix} \rho u_z \\ \rho u_z^2 + p \\ \rho u_r u_z \\ u_z(\rho E + p) \end{bmatrix} \quad \vec{F} = \begin{bmatrix} \rho u_r \\ \rho u_z u_r \\ \rho u_r^2 + p \\ u_r(\rho E + p) \end{bmatrix} \quad \vec{S} = -\phi \frac{1}{r} \begin{bmatrix} \rho u_r \\ \rho u_r u_z \\ \rho u_r^2 \\ u_r(\rho E + p) \end{bmatrix} \quad (21)$$

where $\varphi = 0, 1$ for rectangular and cylindrical coordinates, respectively.

Here, ρ is density, u_z, u_r are velocity components in axial and radial coordinates. $E = e + (u_z^2 + u_r^2) / 2$ is the total energy per unit mass with the specific internal energy e , and p is the hydrostatic pressure, respectively. The governing equations are solved by a third-order Runge-Kutta in time, and convex ENO (essentially non-oscillatory) method discretizes the spatial fluxes [14].

The rate of burnt mass production is governed by

$$\frac{\partial(\rho\lambda_i)}{\partial t} + \frac{\partial(\rho\lambda_i u_j)}{\partial x_j} = w_i \quad (22)$$

where w_i is the reaction rate and λ_i is the reaction progress variable or burned mass fraction. The model is closed by specifying the equation of state, and the form for the rate law. Both Mie-Gruneisen EOS and JWL EOS are used to provide closure to the formulation. The parameters related to these constitutive relations are given in Table 2.2.

The control of the time step increment is determined automatically, where the step size is given by

$$\Delta t_{\text{CFL}} = \text{CFL} \frac{\min(\Delta z, \Delta r)}{\max[u + c, u, u - c]} \quad (23)$$

Here, the sound speeds for Mie-Gruneisen EOS (unreacted) and JWL EOS (reacted) are given by

$$c^2_{unreacted} = \frac{1}{\rho\rho_0} \left[\frac{1-\eta\Gamma}{\eta} P_H + \Gamma\rho(e - e_H) + \frac{2S}{1+\eta(1-S)} (P_H - \Gamma\rho e_H) \right] \quad (24)$$

$$c^2_{reacted} = \frac{\rho_0}{\rho^2} \left[AR_1 \exp(-R_1 \frac{\rho_0}{\rho}) + BR_2 \exp(-R_2 \frac{\rho_0}{\rho}) + C \frac{1+\omega}{(\rho_0/\rho)^{2+\omega}} \right] \quad (25)$$

The combined sound speed is then calculated by using

$$c^2_{total} = (1 - \lambda)c^2_{unreacted} + \lambda c^2_{reacted} \quad (26)$$

To evaluate the predictability of a modeled SDT, the unconfined rate stick experiment is conducted. A series of cylindrical charges with 0.1 m in length and inverse radii being 0 mm⁻¹ to 0.125 mm⁻¹ is used and shock-initiated by an impact on one side with 300 m/s. The prescribed impact was sufficient for pressure rise above the threshold value of the initiation.

Table 2.3 Chapman-Jouguet values of the heavily aluminized RDX.

	P_{cj} (GPa)	16.14
	ρ_{cj} (g/cc)	2.2
C-J condition	e_{cj} (kJ/cc)	1.54
	T_{cj} (K)	4410
	γ	4.24

The C-J conditions for heavily aluminized RDX are given in Table 2.3 obtained by using a thermo-chemical code [15]. Most of the aluminum particles do not participate in the reaction during the detonation phase [16] as these particles in micron size require a significantly long time to be oxidized. Since the reaction time is ultra-short, these metal particles do not have enough time to participate in the reaction. The RDX would still follow its sole reaction path without the particle effect. For a different particle size distribution, however, smaller particles are ignited in a relatively shorter time, thus providing extra heat release of the reaction.

Figure 2.3 shows computational domain. Two distinct materials which are void and explosive were initially brought to a contact by a zero level set represented by a black line in the figure. Six different radiuses are considered in the simulation that were carried out on a uniform mesh of size 1/120 mm.

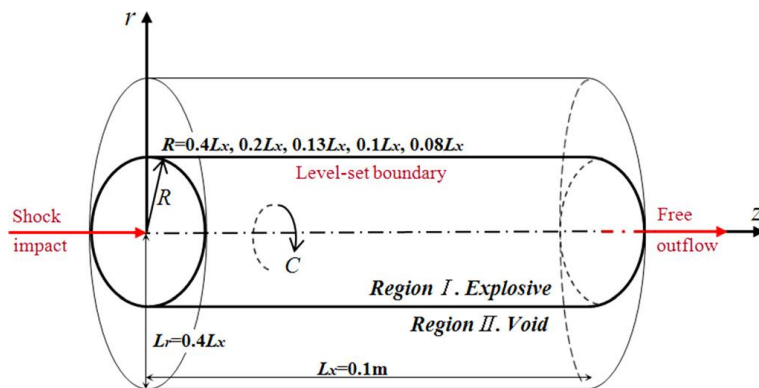


Fig. 2.3 Computational domain of a 2-D cylindrical duct for unconfined rate stick simulation.

Figure 2.4 is a plot of the detonation wave structures illustrated according to grid resolution. The lines are represented by dotted ($h = 0.05$ mm), dashed ($h = 0.0167$ mm), and solid ($h = 0.0083$ mm). As seen from the figure, optimal mesh size of $h = 0.0083$ mm seems to support convergence of a detonation wave.

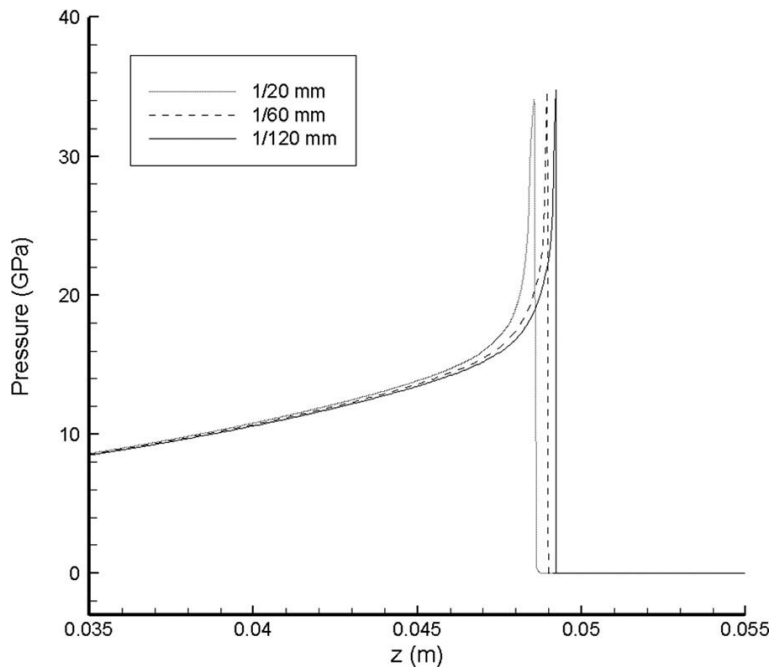


Fig. 2.4 Convergence of detonation wave front shown with grid resolution.

The length of the reaction zone of heavily aluminized RDX is obtained from the detonation pressure profile and the burned mass fraction in Fig. 2.5, and it is approximately 4.0 mm. At that time, $p_{ZND} = 35$ GPa, $p_{CJ} = 16$ GPa, $p_{ZND} / p_{CJ} = 2.1875$. For reference, the length of the reaction zone of a pure RDX is 0.4 mm ~ 0.5 mm [17, 18]. This suggests that the reaction zone length of a heavily aluminized RDX is 10 times that of a pure RDX.

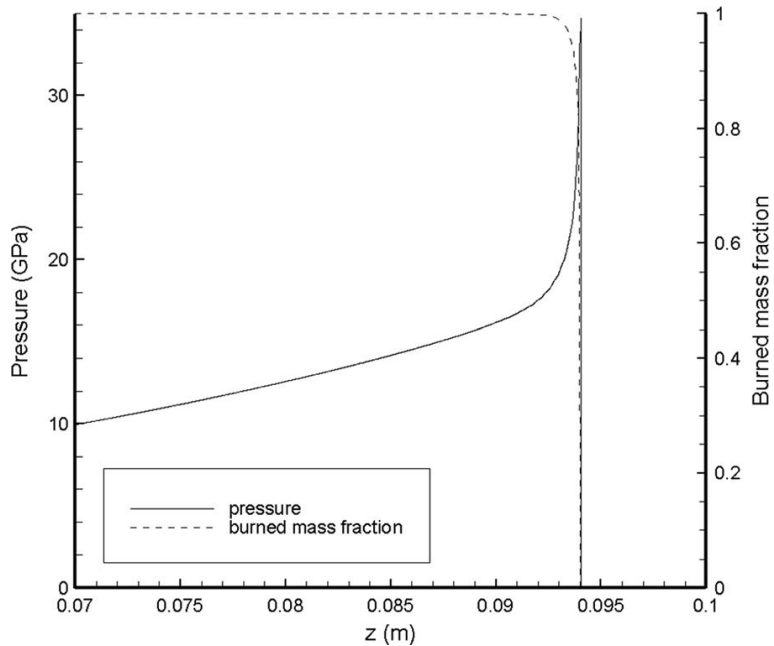


Fig. 2.5 Structure of detonation wave representing the reaction zone of heavily aluminized RDX.

Figure 2.6 depicts density contours that account for the detonation front propagation and expansion of exhaust gas outwards in the cases of infinite (0

mm⁻¹), 13.33 mm (0.075 mm⁻¹) and 8 mm (0.125 mm⁻¹) radius. Behind the detonation front, most of reactants are consumed and high pressure product gas gives rise to an extended reaction zone length. The reaction starts at the shock front and ends along the sonic point (C-J state). The compression region occurs just ahead of the reaction zone in both cases. Results show that the detonation velocity is strongly dependent on the size of the charge.

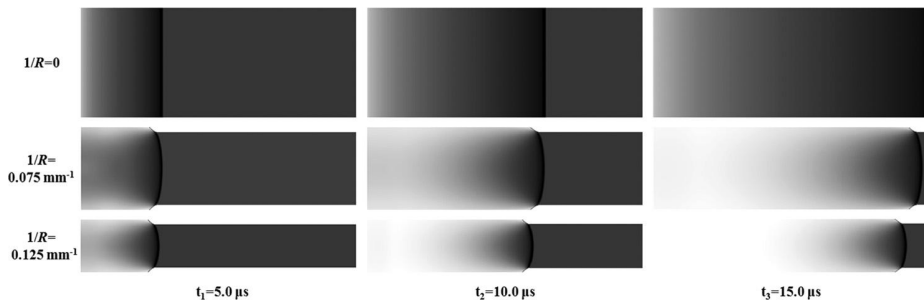


Fig. 2.6 Density contours for unconfined rate stick simulation of 0 (top), 0.075 mm⁻¹ (middle), and 0.125 mm⁻¹ (bottom) inverse radius cases with density range 0.1~2.4 g/cc.

Figure 2.7 describes propagation of detonation wave for 0 and 0.125 mm⁻¹ unconfined rate sticks. A series of pressure profiles shows the transition and stabilization of a von Neumann spike. The figure indicates that there are two distinct regions: *i*) run up region that represents fluctuation of detonation pressure, and *ii*) steady region that describes the convergence of detonation flow.

There is a difference in the detonation velocity of 0 and 0.125 mm⁻¹ rate sticks. The mean ZND pressures in the steady region for these rate sticks are calculated as being $p_{\text{ZND}}|_{r=0 \text{ mm}^{-1}} = 35 \text{ GPa}$, $p_{\text{ZND}}|_{r=0.125 \text{ mm}^{-1}} = 27 \text{ GPa}$, respectively. This suggests that pressure gradient determines the detonation velocity of a rate stick as such that the chemical energy pumping in the shocked region is decreased as the stick diameter is reduced.

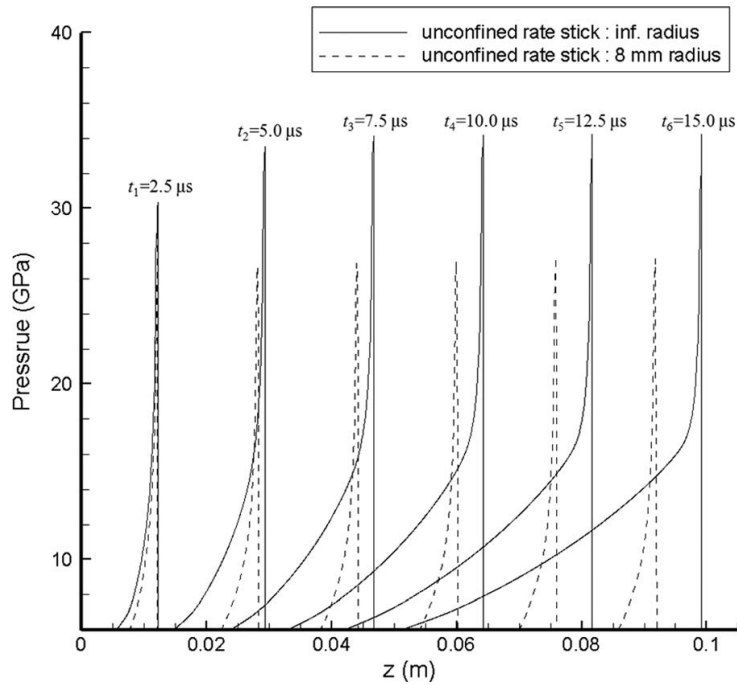


Fig. 2.7 Propagation of detonation front in 0 and 0.125 mm⁻¹ unconfined rate sticks.

The size effect curves showing detonation velocity versus inverse radius are shown in Fig. 2.8. The hydrocode simulation is shown to reproduce the

detonation velocities of 6 sample radii of unconfined rate sticks (0 mm^{-1} , 0.025 mm^{-1} , 0.050 mm^{-1} , 0.075 mm^{-1} , 0.100 mm^{-1} , 0.125 mm^{-1}). Table 2.4 shows comparison of the fully developed detonation velocity. The size effect data using the present rate law and parametric study is in good agreement with the experimental data, suggesting that the model effectively reduced steps in the parameter determination and solved the over-simplification issue related to JWL++ model.

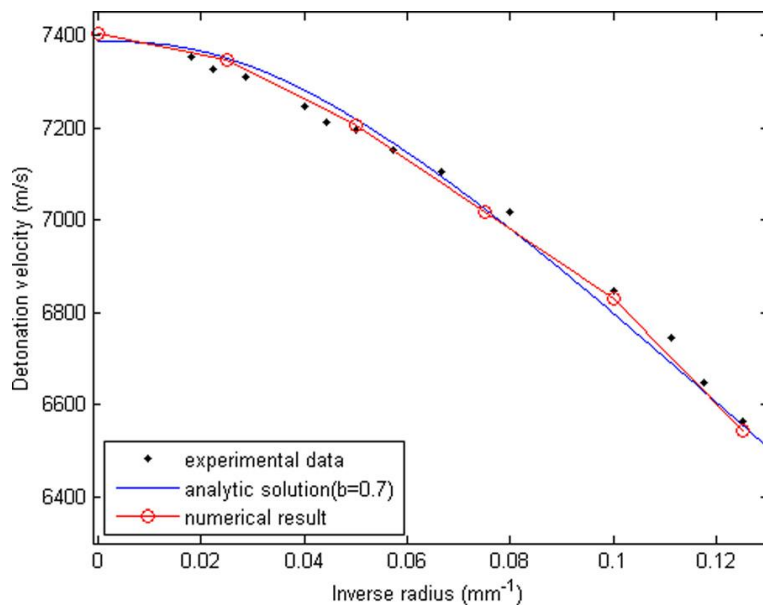


Fig. 2.8 Size effect curve for the unconfined rate stick tests for heavily aluminized RDX.

Table 2.4 Comparison of the fully developed detonation velocity for different charge radius.

Inverse radius (mm ⁻¹)	Detonation velocity (m/s)	
	Numerical	Experimental
0	7403.3	7387 (est.)
0.025	7348.9	7322 (est.)
0.050	7207.1	7197
0.075	7018.3	7044 (est.)
0.100	6829.9	6848
0.125	6544.2	6565

2.5 Conclusion

A reactive flow model aimed at quantifying the detonation response of energetic materials subjected to an external shock impact is presented. A detailed explanation for determining the free parameters of the model is provided. A validation experiment is performed using a heavily aluminized RDX. The unconfined rate stick experiment offered detonation velocity as a function of the charge radius. The hydrocode simulation that utilized the present chemical mechanism confirmed that the proposed reactive flow model reproduced the experimental measurements, and it can overcome the limitations set by the earlier reactive flow models.

CHAPTER 3

Simulating Sympathetic Detonation

3.1 Background and objective

Sympathetic detonation is dominantly driven by the propagation of detonation between individually cased high explosives; impact of a high-speed fragment produced by expansion of the casing is one of the primary causes of a chain detonation. We focus on an aluminized high explosive which is comprised of 64% RDX (cyclotrimethylene-trinitramine, $C_3H_6N_6O_6$) and 20% aluminum powder with 16% hydroxyl-terminated polybutadiene (HTPB) binder. The initial density after pressing is 1.6495 g/cc, and the steel casing is a silicon-manganese steel, AISI 9260.

A methodology to model and simulate sympathetic detonation with good accuracy and reproducibility relies on building the reactive flow model for high explosives and the complex multi-material scheme for handling the interaction between the reactive and inert materials. The SD experiment is also a large-scale test that requires great effort and costs, not to mention the safety of the researchers involved. Thus a single numerical model for all SD experiments is highly desired and valued in the munitions handling, storage, and safety assurance.

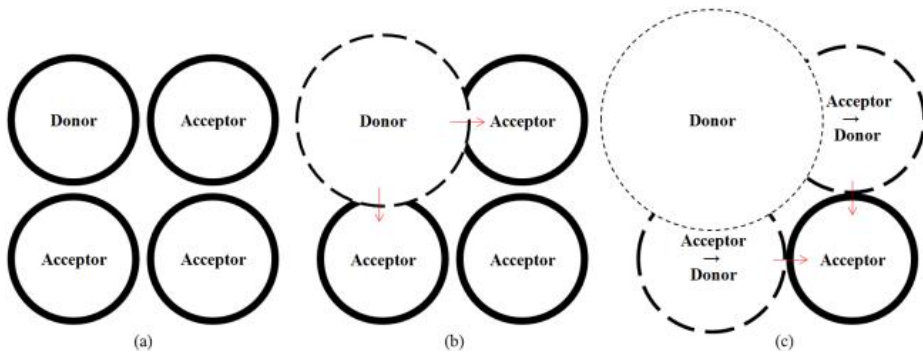


Fig. 3.1 Stacked high explosives for sympathetic detonation showing (a) initial configuration, (b) donor casing impacting neighbors after donor initiation, (c) fragmentation and subsequent chain initiation [1].

The unintended detonation of an explosive charge initiated by a shock wave or a blast fragment from the donor explosive presents a substantial safety risk during the storage of high explosives.

Figure 3.1 illustrates a scenario in which a sympathetic detonation is occurred in a closely packed four cylinder configuration. The casing expands during a center-loaded charge detonation. The fracture is quickly accompanied by fragmentation and venting of hot product gases, whereupon slender strips and breaking pieces are generated. The neighboring acceptors adjacent to a detonating charge (a donor) are impacted by the split fragments along with the blast wave of donor detonation. The subsequent propagation of waves and fragments ultimately results in devastation of the pallet-packaged or stacked shells.

Lochert et al. [2] attempted to investigate the damage reduction effect during SD using the reduced sensitivity RDX (RS-RDX), and showed reliability of their improved insensitivity. Son et al. [3] attempted to protect large-scale detonation of 100 detonators in a carton from external threat by changing the internal structure in the form of a metal tube surrounding the initiator. PETN was used to replace RDX in order to desensitize the shock sensitivity of the base charge. Nevertheless, full-scale tests of SD require enormous time and cost, as such precise capturing of the process is quite challenging. For this reason, quantitative discussion is often absent; instead qualitative results are reported with the number and size of the retrieved fragments for estimating the violence of a SD.

Fisher et al. [4] tested sympathetic detonation using five explosive charges that are packed with 92% HMX, 6% DOA, and 2% carboxylterminated polybutadiene powder. Their work was focused on the description of shell deformation and expansion that gave rise to fragmentation and subsequent initiation of the acceptor. Chen et al. [5] performed a sympathetic detonation simulation using one donor and four acceptors disposed in four directions surrounding the center, at the same interval distance from the donor, filled with RDX containing aluminum powder. Benjamin et al. [6] numerically analyzed one-on-one sympathetic detonation, of which the configuration is comprised of a mild steel cased composition B (60% RDX, 40% TNT) as a donor over the intermediate buffer made of plexiglass or rolled homogeneous

armor (RHA) materials and an acceptor charged with pentolite (50% PETN, 50% TNT). Because the simulation and experiment are complementary, numerical study can further cover areas unseen from SD experiment such as the process of fragmentation, detonation propagation, and chemical reaction runaway during SD process. For this reason, to build a numerical model that can strongly complement the experiment is especially desirable for understanding the SD process.

The aim of this study is to model SD involving chain reactions of eight pallet-packaged high explosives (64% RDX, 20% Al, 16% HTPB) cased in the AISI 9260 steel. The constitutive laws of reaction kinetics and the equations of state for both unreacted and reacted materials are established. Also, stochastic failure model based on the Mott probability function is used to describe the forming process of fragments. With the use of a multi-dimensional hydrodynamic simulation, SD model is constructed. As a validation of the results, the experimental SD provided the pressure measurements for comparison with the simulation.

3.2 Sympathetic detonation test

A sympathetic detonation test of eight pallet-packaged PBXN-109 is performed, where the blast effect is measured as a time trace of pressure. Two set of pressure gauges were laid out at distances of 15 m and 20 m from the source. The length of 945.7 mm and average diameter of 153.9 mm is

considered for PBXN-109. The average thickness of the casing is 13.8 mm. Figure 3.2 shows the test configuration with pressure sensors (PCB 137A23) shown. Data acquisition device (DAQ) of DEWE-SIRIUS had bandwidth of 0.2 MHz or frequency resolution of $5 \mu\text{s}$ (5×10^{-6} sec).



Fig. 3.2 Experimental setup of sympathetic detonation of pallet-packaged 155 mm shell.

3.3 Methods and mathematical formulation

The multi-material numerical simulation of sympathetic detonation is conducted with an ALE-based hydrodynamic code. The detonation of high explosives occurs on the microsecond time scale as such the relatively slower processes namely heat conduction, viscous dissipation, and radiation are neglected. The pressures generated by the detonation of a condensed explosive are of several GPa. Under this condition, the strength of the confining material is also neglected as the material is assumed to flow as if a fluid. The hydrodynamic behavior of the full process is described by the compressible Navier-Stokes equations that describe the conservation of mass, momentum, and energy and species reaction [7]:

$$\frac{\partial \rho}{\partial t} + \rho \frac{\partial u_i}{\partial x_i} = 0 \quad (1)$$

$$\frac{\partial(\rho u_j)}{\partial t} + \frac{\partial(\rho u_i u_j)}{\partial x_i} = -\frac{\partial P}{\partial x_j} + \frac{\partial S_{ji}}{\partial x_i} \quad (2)$$

$$\frac{\partial E}{\partial t} + \frac{\partial(E u_j)}{\partial x_j} = \rho \dot{q} - \frac{\partial P u_j}{\partial x_j} + S_{ji} \frac{\partial u_i}{\partial x_i} \quad (3)$$

$$\sigma_{ij} = S_{ij} - \delta_{ij} P \quad (4)$$

$$P = P(\rho, e, \lambda) \quad (5)$$

$$\frac{\partial(\rho\lambda_i)}{\partial t} + \frac{\partial(\rho\lambda_i u_j)}{\partial x_j} = w_i \quad (6)$$

In equations (1) – (6), ρ is density, u is the fluid velocity, and P is the hydrostatic pressure. Also, E is the total energy per unit volume, where $E = \rho e + \rho u_i^2/2$ with the specific internal energy e . In order to address the solid deformation, the Cauchy stress tensor, σ_{ij} is separated into two terms, namely deviatoric stress tensor, S_{ij} and hydrostatic pressure as shown in Eq. (4). w_i is the reaction rate and λ_i is the reaction progress variable, which is the burned mass fraction.

In describing both reactive and unreactive state of matter, the equations of state relating pressure, density, and energy are utilized. The Jones-Wilkins-Lee (JWL) parameter form of equations [8] in Eq. (7) and (8) for unreacted reactant and gaseous product gas of high explosive are used.

$$P_{unreacted} = A \left(1 - \frac{\omega}{R_1(\rho_0/\rho)} \right) e^{-R_1(\rho_0/\rho)} + B \left(1 - \frac{\omega}{R_2(\rho_0/\rho)} \right) e^{-R_2(\rho_0/\rho)} + \frac{\omega e_0}{(\rho_0/\rho)} \quad (7)$$

$$P_{reacted} = A e^{-R_1(\rho_0/\rho)} + B e^{-R_2(\rho_0/\rho)} + \frac{C}{(\rho_0/\rho)^{\omega+1}} \quad (8)$$

A , B , C , R_1 , and R_2 are the material dependent JWL parameters with ω being the Gruneisen coefficient of the explosive. These parameters are obtained by fitting the JWL-EOS to the cylinder expansion test results or

thermodynamic equilibrium calculation using CHEETAH [9], where $e_0 = \rho_0 C_v T$ refers to the thermodynamic energy in GPa. Particularly, Eq. (8) is an isentropic JWL C-term form of EOS used for products, and is derived according to the thermodynamics 1st law argument for isentropic process:

$$de = \delta q - \delta w = Tds - Pdv = -Pdv \quad (9)$$

Integrating Eq. (9) returns the following expression

$$\begin{aligned} e_0 &= -\int Pd(\rho_0/\rho) \\ &= \int \left(Ae^{-R_1(\rho_0/\rho)} + Be^{-R_2(\rho_0/\rho)} + \frac{C}{(\rho_0/\rho)^{\omega+1}} \right) d(\rho_0/\rho) \\ &= \frac{A}{R_1} e^{-R_1(\rho_0/\rho)} + \frac{B}{R_2} e^{-R_2(\rho_0/\rho)} + \frac{C}{\omega(\rho_0/\rho)^\omega} \end{aligned} \quad (10)$$

When Eq. (10) is substituted to the JWL EOS in Eq. (7),

$$\begin{aligned} P_{unreacted|isentropic} &= \\ &A \left(1 - \frac{\omega}{R_1(\rho_0/\rho)} \right) e^{-R_1(\rho_0/\rho)} + B \left(1 - \frac{\omega}{R_2(\rho_0/\rho)} \right) e^{R_2(\rho_0/\rho)} + \\ &A \frac{\omega}{R_1(\rho_0/\rho)} e^{R_1(\rho_0/\rho)} + B \frac{\omega}{R_2(\rho_0/\rho)} e^{R_2(\rho_0/\rho)} + \frac{C}{(\rho_0/\rho)^{\omega+1}} \end{aligned} \quad (11)$$

Thus, the C-term JWL EOS for reaction is the isentropic form of the original JWL equation.

Here, the sound speeds for Mie-Gruneisen EOS (unreacted) and JWL EOS (reacted) are given by

$$c^2_{unreacted} = -\frac{\rho_0}{\rho^2} \left[A \frac{\omega}{R_1 v^2} e^{-R_1(\rho_0/\rho)} + B \frac{\omega}{R_2 v^2} e^{-R_2(\rho_0/\rho)} - \frac{\omega e_0}{(\rho_0/\rho)} - AR_1 \left(1 - \frac{\omega}{R_1(\rho_0/\rho)} \right) e^{-R_1(\rho_0/\rho)} - BR_2 \left(1 - \frac{\omega}{R_2(\rho_0/\rho)} \right) e^{-R_2(\rho_0/\rho)} \right] \quad (12)$$

$$c^2_{reacted} = \frac{\rho_0}{\rho^2} \left[AR_1 e^{-R_1(\rho_0/\rho)} + BR_2 e^{-R_2(\rho_0/\rho)} - C \frac{1+\omega}{(\rho_0/\rho)^{2+\omega}} \right] \quad (13)$$

The unreacted and reacted EOS are combined into a single expression, Eq. (14), using the product mass fraction (λ) and reactant depletion ($1-\lambda$).

$$P = (1-\lambda)P_{unreacted} + \lambda P_{reacted} \quad (14)$$

The combined sound speed is then calculated by using

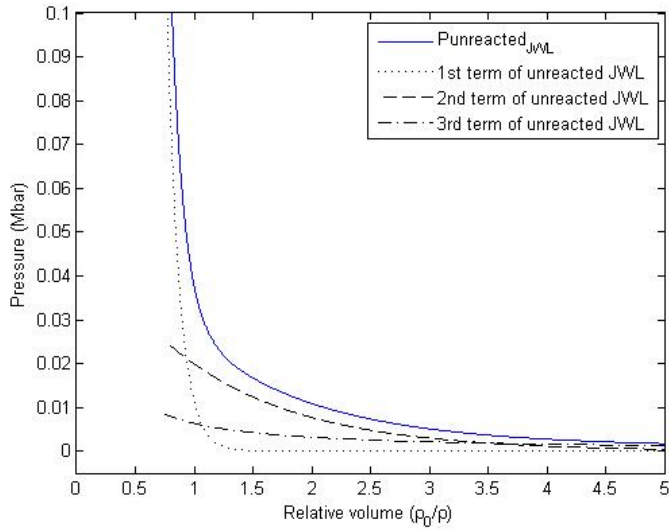
$$c^2 = (1-\lambda)c^2_{unreacted} + \lambda c^2_{reacted} \quad (15)$$

Meanwhile, thermo-chemical code namely CHEETAH incorporates a fitting program to an optimal parameters of JWL EOS. It works based on the cylinder test data that provide a detailed information on the thermodynamic C-J states including pressure, volume, energy, temperature, and detonation velocity. Parameterization of JWL EOS is done by a number of CHEETAH runs to use in the empirical fitting procedure. Table 3.1 shows the C-J conditions for the PBXN-109.

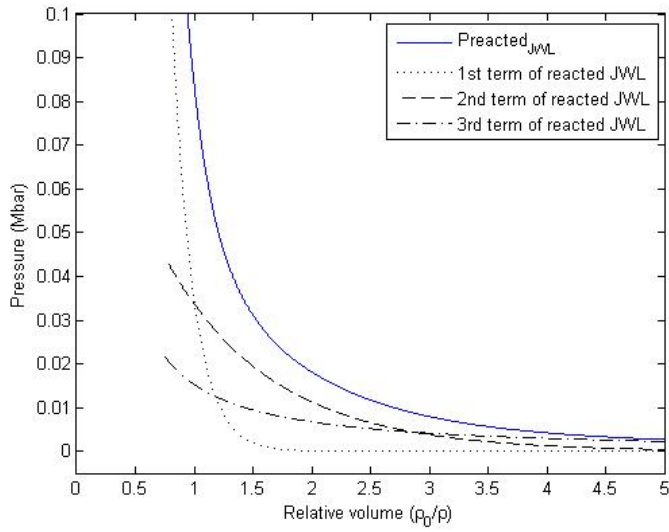
Table 3.1 Chapman-Jouguet conditions for PBXN-109.

	ρ_0 (g/cc)	1.6495
	P_{cj} (GPa)	18.64
C-J condition	ρ_{cj} (g/cc)	2.146
	e_{cj} (kJ/cc)	2.16
	T_{cj} (K)	4702
	γ	3.320

Figure 3.3 indicates the JWL pressure profiles of unreacted and reacted EOS with respect to the relative volume using the JWL EOS parameters for the PBXN-109 explosive which are given in Table 3.2. The first term of JWL EOS acts as a high pressure function that dominates any relative volume close to 1. The second term is significant at intermediate pressures; finally, the third term prevails in the expanded state where relative volume reaches infinity or large volumes.



(a) Unreacted JWL EOS



(b) Reacted JWL EOS

Fig. 3.3 JWL pressure profiles of unreacted and reacted EOS with respect to the relative volume.

The reactive flow model uses the rate of product mass fraction that consists of ignition and growth as suggested by Kim et al. [10].

$$\frac{d\lambda}{dt} = I(1 - \lambda)\mu^a + G(1 - \lambda)P^b, \mu = \frac{\rho}{\rho_0} - 1 \quad (16)$$

Here, P is the pressure, t is time, and ρ_0 and ρ are the initial and current densities, respectively. λ is the burned mass fraction, and constants I , a , G , and b are the unknown parameters. λ is the reaction progress variable ($\lambda = 0$ unreacted state and $\lambda = 1$ reacted state) and the compression term, μ , is defined as ($\mu = \rho/\rho_0 - 1$). The suggested rate law is comprised of *i*) the ignition term that represents the formation of hotspots by rapid compression and *ii*) the growth term that describes the effect of the propagation of the reacting waves on the substance. Four unknown parameters are determined from the unconfined rate stick test.

To evaluate the predictability of a detonation model, the size effect analysis is conducted. A series of numerical simulations using cylindrical charges with 0.1 m in length and inverse radii being 0 mm⁻¹ to 0.125 mm⁻¹ are used. The computational domain and numerical details are sourced from the preceding work [10]. The hydrocode simulation is conducted to reproduce the detonation velocities of 6 sample radii of unconfined rate sticks (0 mm⁻¹, 0.025 mm⁻¹, 0.050 mm⁻¹, 0.075 mm⁻¹, 0.100 mm⁻¹, and 0.125 mm⁻¹).

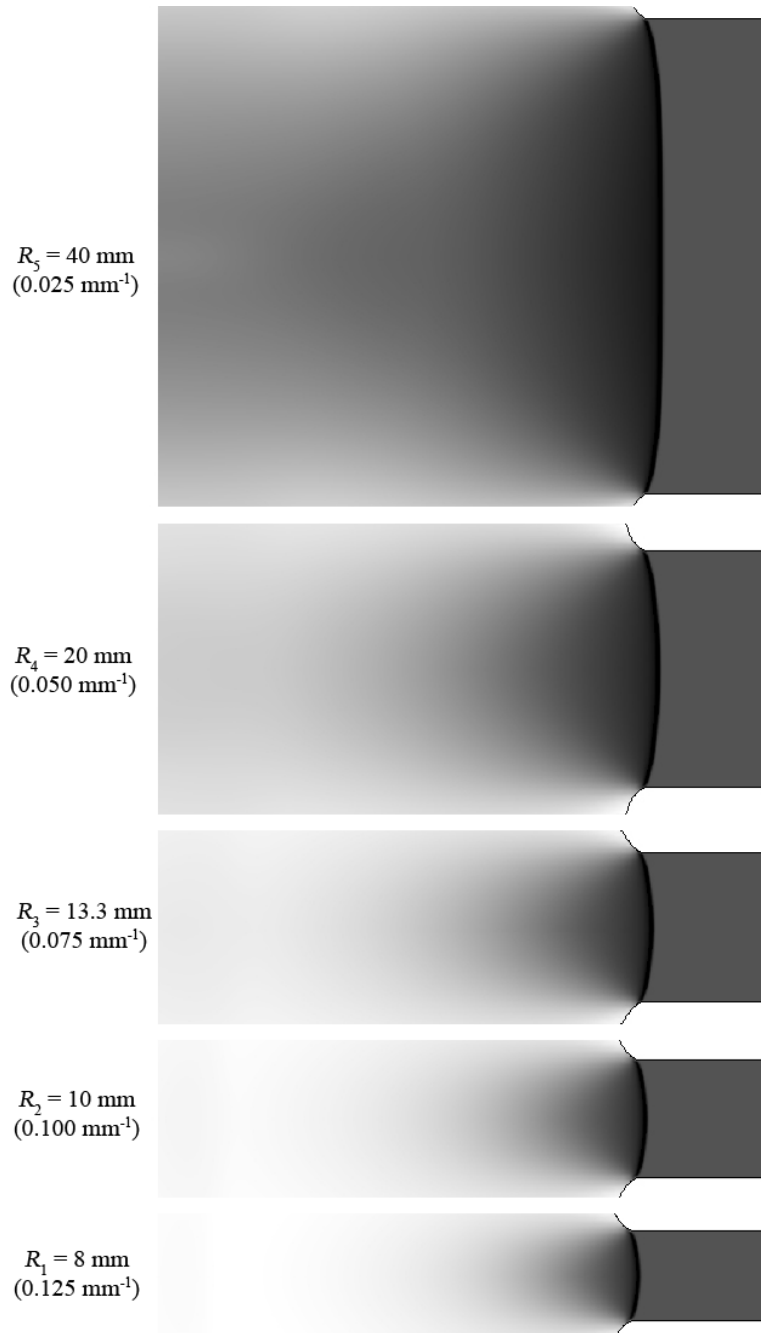


Fig. 3.4 Density contours for the unconfined rate stick of PBXN-109 at $t=12.5 \mu\text{s}$ with density range 0.1-2.5 g/cc.

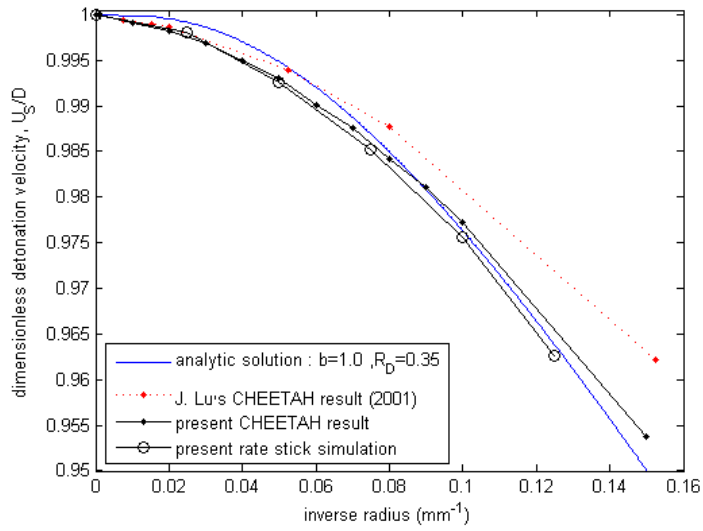


Fig. 3.5 Size effect curves for the unconfined rate stick of PBXN-109.

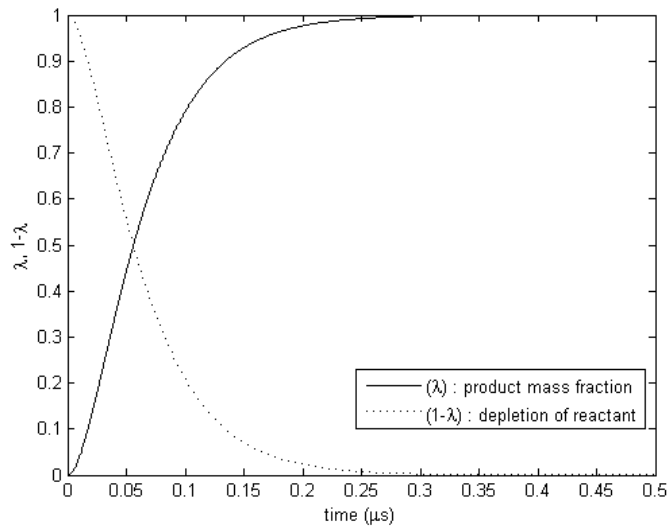


Fig. 3.6 Time trace of product and reactant mass fraction of PBXN-109.

Figure 3.4 depicts density contours that account for the propagation of detonation wave front in the rate stick simulations at $t = 12.5 \mu\text{s}$. It is noted that there is a difference in the distance of detonation wave front of several sample radii sticks at the same time. Results show that the detonation velocity is strongly dependent on the size of the charge. This phenomenon is based on the level of peak pressure of the wave front. The reaction starts at the shock front and ends along the sonic point (C-J state). Behind the detonation front, most of reactants are consumed and product gas gives rise to high pressure. Pressure gradient determines the detonation velocity of a rate stick as such that the chemical energy pumping in the shocked region is decreased as the stick diameter is reduced.

The size effect curves showing detonation velocity versus inverse radius are shown in Fig. 3.5. The CHEETAH is also used to predict the detonation velocities dependent on charge radius. It is calculated by the balance between the energy produced by chemical reaction and the energy loss due to radial expansion of the product gases. Thus the relationship on the energy balance between driving and expansion in unconfined rate stick test allows prediction of the dependence of detonation velocities on charge diameters. Though it seems that the measurement is still necessary to get factual data, using CHEETAH is indeed quite convenient to obtain the detonation behavior of high explosives in place of the actual experiments. Especially the pressure sensitivity, b , can be analytically determined by using the size effect data from

CHEETAH calculation. The size effect data using the rate law and JWL EOS is in good agreement with the CHEETAH data and analytical solution. Here, the analytic line [10] is calculated using Eq. (17).

$$\frac{R_D}{R_0} = -\frac{0.4[1-(U_s/D)^2]^{-0.8}}{\ln(1-(U_s/D)^2)} \left(\frac{U_s}{D}\right)^{2b-1} \left(1-\frac{U_s}{D}\right) \quad (17)$$

Figure 3.6 shows time trajectory of the product and reactant mass fraction of PBXN-109. The constants of ignition I and growth G are set to $2.5 \times 10^8 \text{ s}^{-1}$ and $1.1 \times 10^8 \text{ s}^{-1} \text{ Mbar}^{-b}$, respectively. The pressure sensitivity b of the explosive is 1.0, and the compression sensitivity, a , is 4.0. The constants evaluated from the ignition and growth relations as shown below.

$$G = D(R_D P^b)^{-1} \quad (18)$$

$$I \cong 0.1 G P^b \eta^{-a} \quad (19)$$

As for non-reactive solids, Mie-Gruneisen form EOS [11] is adapted to calculate the pressure of the casing materials.

$$P = P_H + \Gamma \rho (e - e_H) \quad (20)$$

where P_H and e_H refer to the pressure and internal energy, respectively, of a reference state that follows the Hugoniot curve, and Γ is the Gruneisen gamma. P_H , e_H , and Γ can be expressed as follows:

$$P_H = \frac{\rho_0 c_0 \mu (1 + \mu)}{[1 - (s - 1)\mu]^2} \quad (21)$$

$$e_H = \frac{P_H}{2\rho_0} \left(\frac{\mu}{1 + \mu} \right) \quad (22)$$

$$\rho\Gamma = \rho_0\Gamma_0 \quad (23)$$

where c_0 is the bulk sound velocity at a reference condition in the given material and s is a linear Hugoniot slope coefficient. Also, the shock speed relations are

$$s = dU_{shock} / dU_{particle} \quad (24)$$

$$c_0 = (\partial P / \partial \rho)^{1/2} \quad (25)$$

$$U_{shock} = c_0 + sU_{particle} \quad (26)$$

where U_{shock} is the shock wave velocity and $U_{particle}$ is the material particle velocity. In the above expressions, the shock velocity and the particle velocity are assumed to obey a linear relationship. The $\rho\Gamma$ is assumed to be a constant.

The casing material is modeled as AISI 9260 alloy steel. With the expanding force resulting from explosive detonation, the Johnson-Cook strength model [12] is employed to calculate the flow stress. The model is purely empirical and is expressed as

$$Y(\varepsilon_p, \dot{\varepsilon}_p, T) = \left[A_0 + B_0 \varepsilon_p^n \right] \left[1 + C_0 \ln \left(\frac{\dot{\varepsilon}_p}{\dot{\varepsilon}_{p0}} \right) \right] \left[1 - \left(\frac{T - T_0}{T_m - T_0} \right)^m \right] \quad (27)$$

where Y is the yield stress and ε_p , $\dot{\varepsilon}_p$, and $\dot{\varepsilon}_{p0}$ are the effective plastic strain, the effective plastic strain rate, and the effective plastic strain rate of the quasi-static state, respectively. The normalized temperature is defined according to reference room temperature, T_0 , and reference melt temperature, T_m . For conditions where $(T - T_0) < 0$, we assume that $m = 1$. The strength model that accounts for the effects of strain hardening, strain-rate hardening, and thermal softening are adopted to describe the dynamic response of the steel. In addition, the strength model constants, namely, A_0 , B_0 , C_0 , m , and n are used for AISI 9260 steel. As strain rate approaches zero, the natural log

approaches negative infinity, and therefore the Johnson-Cook model sets C to a zero if strain rate reaches a certain minimum value, usually 1 s^{-1} .

In addition, a Mott probability distribution [13] can be implemented in conjunction with the model for the non-reactive material.

$$P_m(\varepsilon_p) = 1 - \exp\left(-\frac{C_m}{\gamma} \left[\exp(\gamma\varepsilon_p) - 1\right]\right) \quad (28)$$

The exponential in Eq. (28) determines the tensile crack softening as a stochastic failure. It is given for the break-up of the metal case of a cylindrical explosive and for the length of the average fragment. Here, $P_m(\varepsilon_p)$ is the probability of fracture, and C_m and γ are the constants of hardness and softness, respectively. Figure 3.7 shows profiles of Mott probability distribution for varying the values of $\gamma = 3, 5, 10, 50$. The exponentially increased lines along the failure strain are plotted with different slope. It is close to step function when γ is increasing, the material can be broken or not at the point of $\varepsilon_p=1$. Generally, rigid material has higher γ , lower γ is for ductile metal because material-dependent constant, γ , represents the soft to rigid characteristic of a solid material.

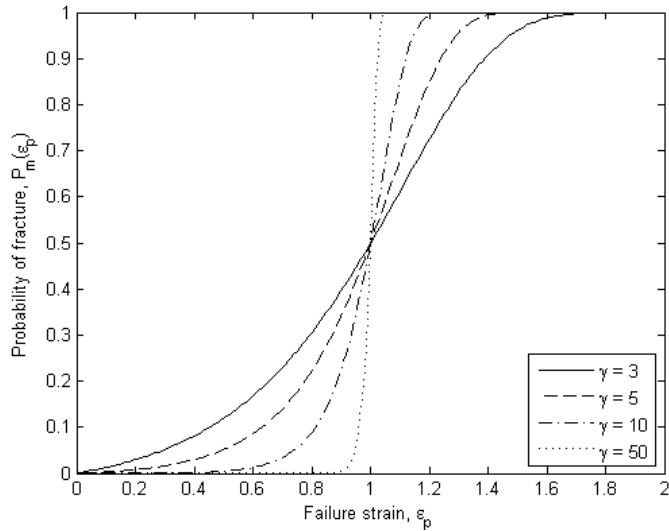


Fig. 3.7 Mott distribution for varying the values of $\gamma = 3, 5, 10, 50$.

3.4 Results and discussions

The model parameters of the constitutive relation for the PBXN-109 explosive are given in Table 3.2. The values used in the present analysis for the non-reactive material, AISI 9260, are given in Table 3.3.

Two sympathetic detonation configurations (with/without inert mockups) were considered to assess the violence. Eight rounds were stacked with a donor placed in the middle, as shown in Fig. 3.8. In the first simulation, all explosives are considered to be live and are filled with PBXN-109. In the second simulation, 5 live acceptors were replaced by the inert mockups that are filled with the sand.

Table 3.2 Modeling parameters of constitutive relations for PBXN-109.

Reactant	A (Mbar)	152.7
	B (Mbar)	0.052
	e_0 (Mbar)	6.54e-3
	R_1	9.500
	R_2	0.950
	ω (J/g-K)	0.976
Product	A (Mbar)	9.883
	B (Mbar)	0.101
	C (Mbar)	1.54e-2
	R_1	5.65
	R_2	1.09
	ω (J/g-K)	0.19
Chemical kinetics	I (s ⁻¹)	2.5x10 ⁸
	a	4.0
	G (s ⁻¹ Mbar ^{-b})	1.1x10 ⁸
	b	1.0

Table 3.3 Modeling constants for AISI 9260.

Mechanical constant	Initial density (g/cc)	7.85
	Young's modulus (Mbar)	2.00
	Shear modulus (Mbar)	0.80
	Poisson's ratio	0.29
Thermal constant	Specific heat capacity (J/kg·K)	472
	Room temperature (K)	300
	Melt temperature (K)	1370~1410
Mie-Gruneisen EOS	C_0 (m/s)	3935
	S_0	1.58
	Gruneisen coefficient	1.69
Strength model	A_0 (Mbar)	0.00792
	B_0 (Mbar)	0.00510
	C_0 (Mbar)	0.26
	n	0.14
	m	1.03

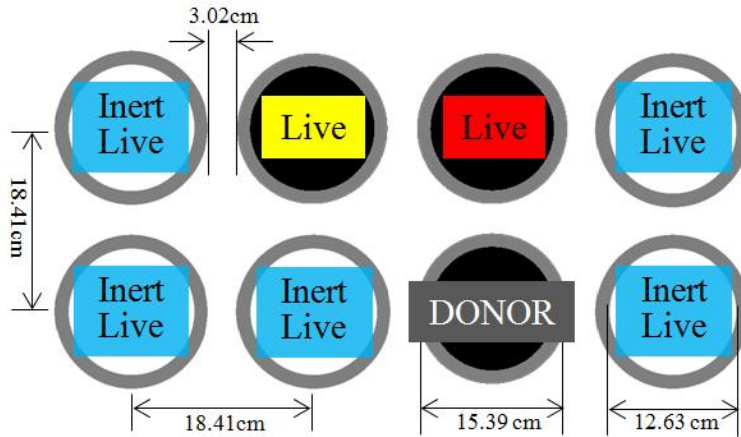
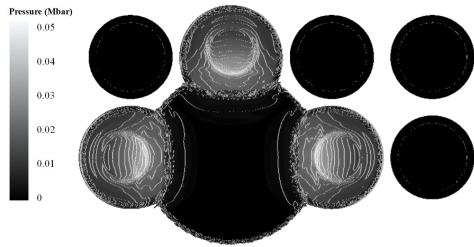


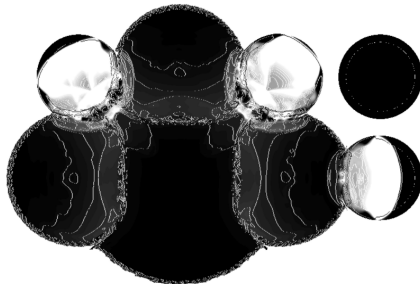
Fig. 3.8 Computational setup for eight pallet sympathetic detonation:

8 lives / 3 lives + 5 mockups.

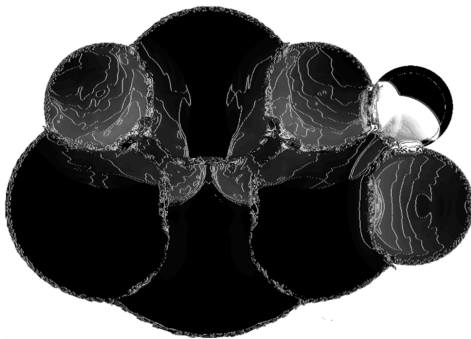
Understanding the SD phenomenon through experimental and numerical study has been a key area in high explosives research. Sympathetic detonation is a challenging subject in terms of both experimental investigations and numerical modeling owing to the complex shock interactions between energetic materials and non-reactive metal components.



(a) $t_1 = 90 \mu\text{s}$

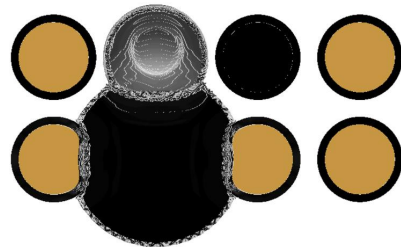


(b) $t_2 = 120 \mu\text{s}$

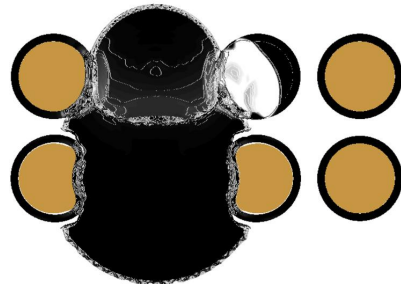


(c) $t_3 = 160 \mu\text{s}$

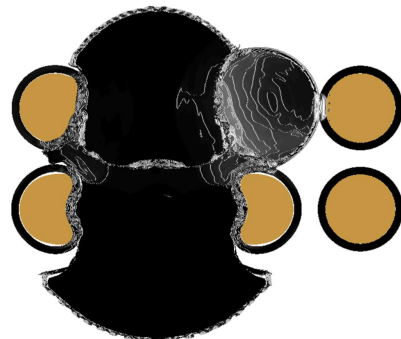
Fig. 3.9 Pressure contours of sympathetic detonation with 8 live rounds. Detonation wave propagation of PBXN-109 and effective plastic strain in the AISI 9260 are shown at (a) $t_1 = 90 \mu\text{s}$, (b) $t_2 = 120 \mu\text{s}$, and (c) $t_3 = 160 \mu\text{s}$ with pressure range 0-0.05 Mbar for PBXN-109 and strain range 0-1 for AISI 9260.



(a) $t_1 = 90 \mu\text{s}$



(b) $t_2 = 120 \mu\text{s}$



(c) $t_3 = 160 \mu\text{s}$

Fig. 3.10 Pressure contours of sympathetic detonation with 3 lives + 5 mockups. Detonation wave propagation of PBXN-109 are shown at (a) $t_1 = 90 \mu\text{s}$, (b) $t_2 = 120 \mu\text{s}$, and (c) $t_3 = 160 \mu\text{s}$ after initiation with pressure range 0-0.05 Mbar for PBXN-109 and strain range 0-1 for AISI 9260.

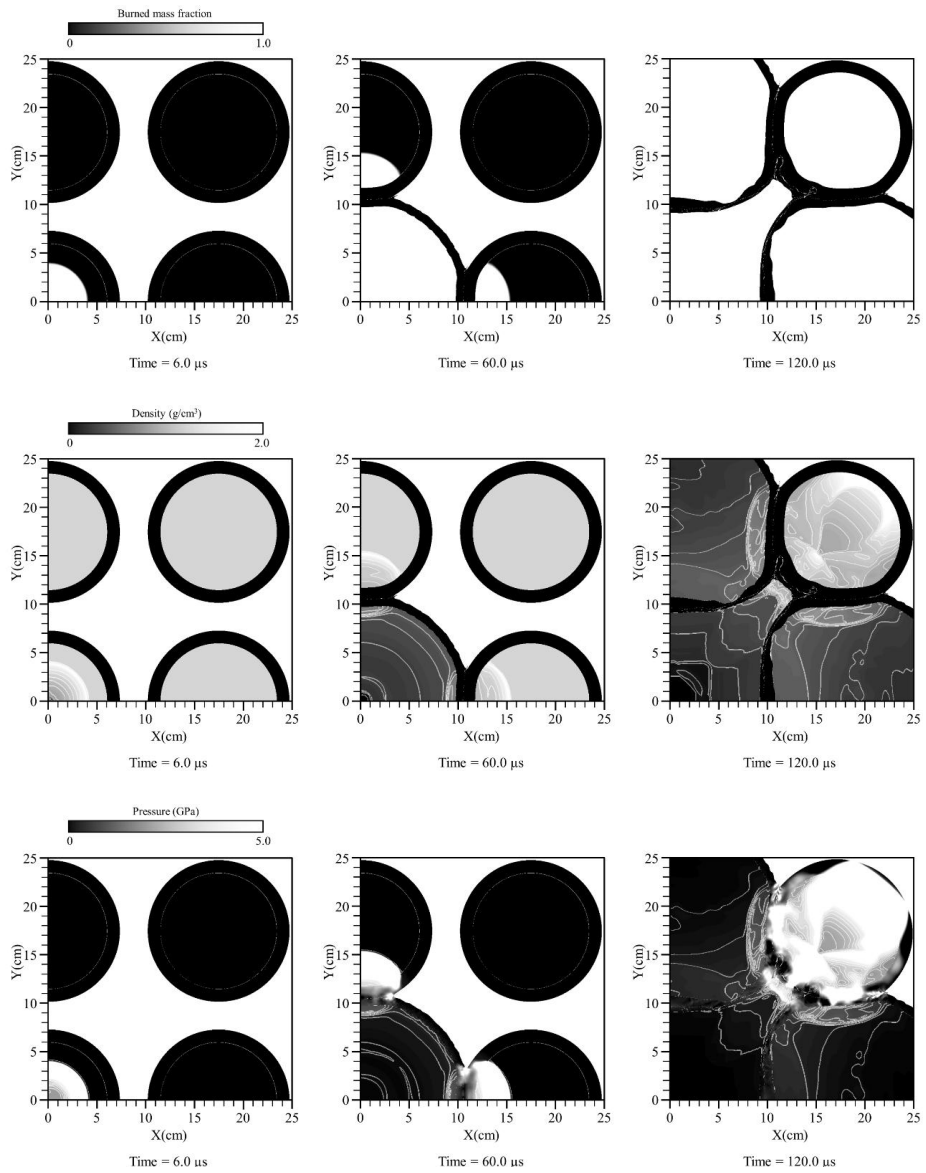


Fig. 3.11 Initiation process induced by shock-metal impact with three different contours and times for PBXN-109. (a) Burned mass fraction range 0-1.0, (b) Density range 0-2.0 g/cm³, and (c) Pressure range 0-5.0 GPa at 6.0 μs, 60.0 μs, and 120.0 μs.

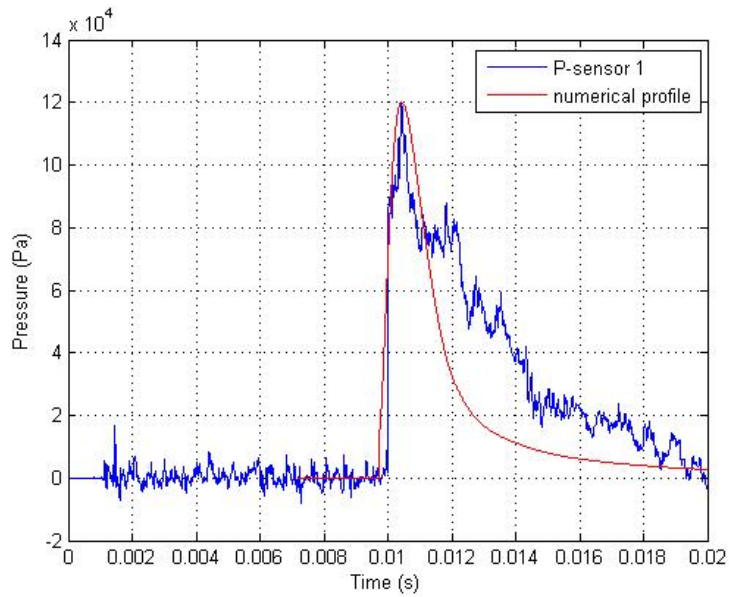
Figure 3.9 depicts the pressure contours that account for the sympathetic detonation at different times. As a donor exploded, the case fragmentation is seen with the fragments bursting out in all directions. The generated fragments collided with the adjacent and diagonal acceptors. Fragment impact then caused initiation of the acceptors. All live acceptors are detonated within 200 μ s.

Figure 3.10 describes the propagation of detonation pressure for the case of 5 inerts, 2 lives, and a donor. Three distinct features are observed: *i*) acceptor initiation is due to the donor fragment impact, *ii*) velocity of fragments increases with high pressure detonation wave, and *iii*) inert mockup damage is solely due to neighboring explosions and fragmentation.

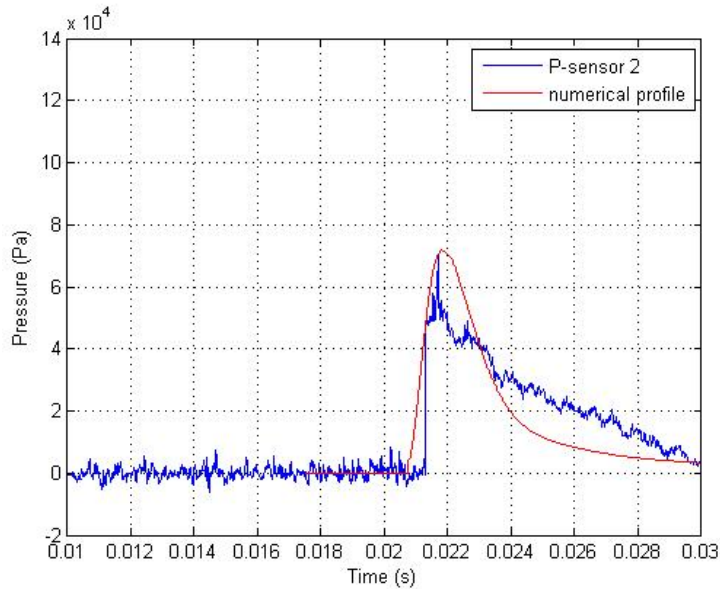
Figure 3.11 explains the phenomenon of the initiation process induced by the shock-metal impact. The SD sequence demonstrates the following steps. 1st step - donor initiation stage. At the center of the donor, the ignition point is generated by the slow cook-off (SCO) scenario. 2nd step - one point initiation stage. The expansion of the donor affects the initiation of the acceptors located at the orthogonal directions. 3rd step - multi point initiation stage. Simultaneously propagating waves from the second step ignite the acceptors located at the diagonal directions and igniting acceptors have multi-ignition points.

The numerous processes leading to sympathetic detonation include initiation of chemical reaction in the donor charge, a rise in pressure, the scattering of fragments of an exploding charge, and penetration of the high-velocity projectiles in the target.

The measured time trace of pressure from two sensors (SN : 10554, SN : 10555) located at 15 and 20 meters from the source is shown in Fig. 3.12. The blast waves of 120 kPa is reached at 15 m and 70 kPa is measured at a distance 20 m. The comparison between the calculation and measurement shows that the peak pressures are very close as well as the waveform and arrival time of the signal are almost identical. Recognizing these results, incident pressure and its propagation can be important factors to proceed with the next initiation of an acceptor which is located where it can be affected by a donor explosion. Thus, SD should be implemented by presenting a reliable modeling the constitutive equations that are comprised of EOS and rate law.



(a) 15 mm probe (SN : 10554)



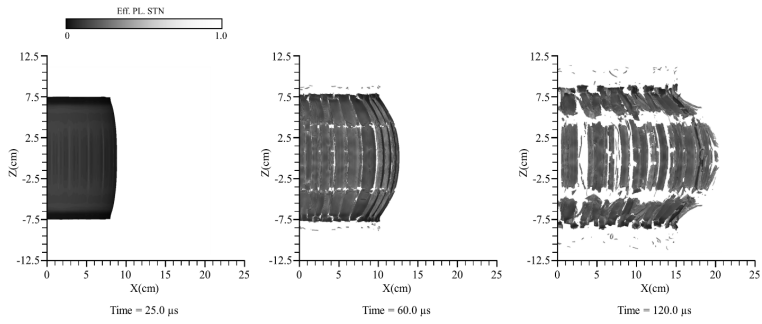
(b) 20 mm probe (SN : 10555)

Fig. 3.12 Time trace of measured pressure profiles at (a) 15 m and (b) 20 m distance probes.

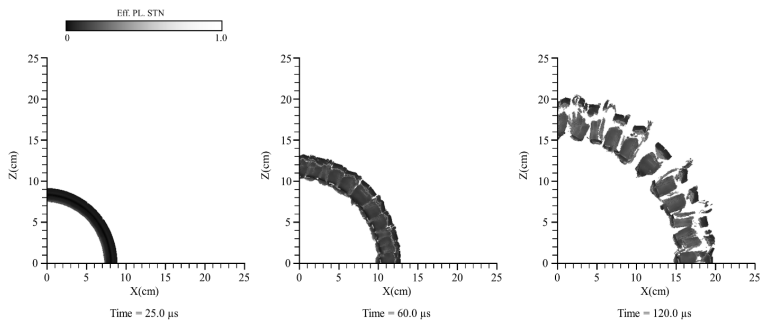
Figure 3.13 shows the broken pieces of the AISI 9260 case after the sympathetic detonation test (a). The pattern is comparable to the fragments obtained from the 3D calculation (b-d). As shown, there are various sizes of the fragments that are generated from the full fracture simulation.



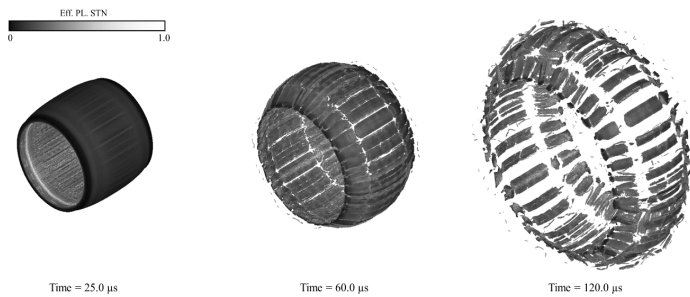
(a) Collected fragments



(b) Fragmentation process with strain range 0-1(Front)



(c) Fragmentation process with strain range 0-1(Top)



(d) Fragmentation process with strain range 0-1(Isometric)

Fig. 3.13 Comparison of calculated broken pieces of AISI 9260 casing with collected fragments.

Figure 3.14 depicts the simulation domain for the 155 mm artillery shell. The full scale simulation includes the explosive encased in a AISI 9260 casing. The casing has its density of 7.85 g/cm^3 and the melting temperature of 1390 K. The thickness of the casing is given by the difference between the outer and inner diameter, approximately 13.8 mm. The grid spacing 7 mm for high explosive resulted in 16732 computational cells while 5 mm grid spacing for casing resulted in 273867 computational cells. Five gauges are distributed on the surface of the AISI 9260 casing with the specified coordinates for data measurement.

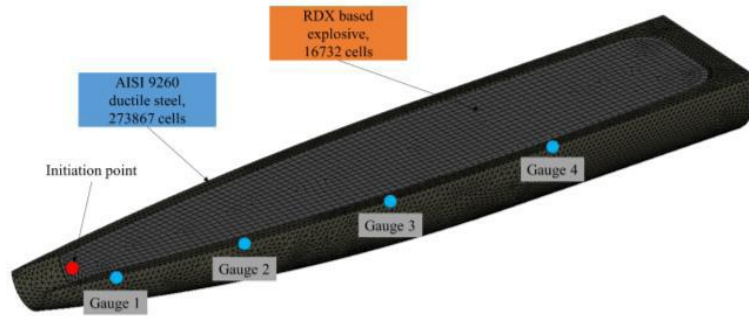


Fig. 3.14 3D computational geometry of 155 mm cased high-explosive.

The fracture and fragmentation in ductile material occur, whereby the void nucleates due to large strain with high pressure, and crack is generated due to the numerous voids created. Figure 3.15 shows the fragmentation process of the casing material due to a detonation of the explosive. The breakup pieces of the casing are first seen at $75 \mu\text{s}$, and nearly all of the casing is fractured at

130 μs . By 200 μs , the rear end plate of AISI 9260 is detached when the fracture is completed. A range of different size and shapes of fragments are generated.

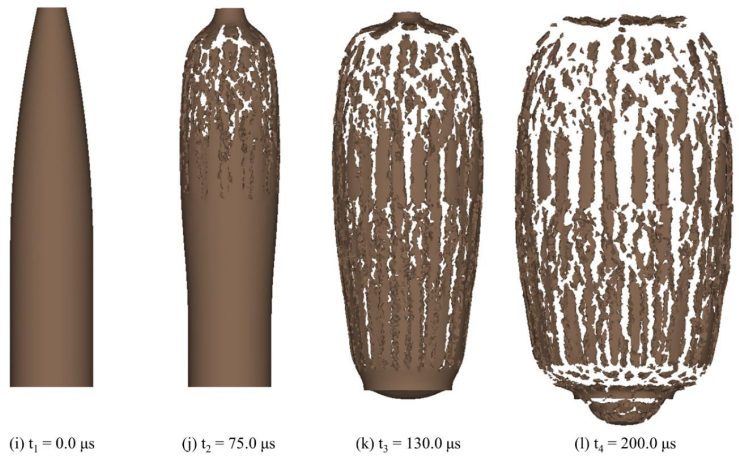
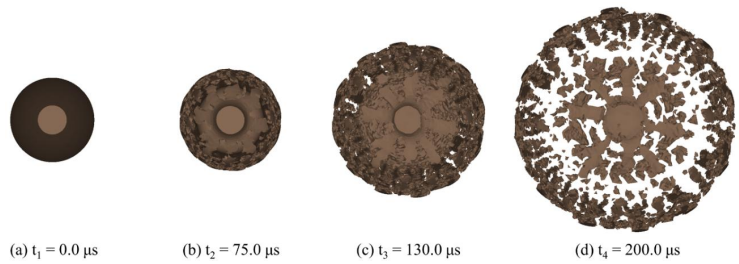


Fig. 3.15 Time sequence of fragmentation process and created broken pieces of AISI 9260 case of 155 mm artillery shell.

Figure 3.16 shows the expansion velocities of the AISI 9260 fragments where the fastest expansion velocity V_{\max} is obtained from gauge 4, at about 970 m/s while the initiation of detonation occurs near the gauge 1.

Figure 3.17 shows number of fragments generated with respect to time. The first occurrence of fragment is at 47.5 μ s, and the number increases to 459 at 230.0 μ s, suggesting the dominance of the later time dynamics that resulted in the fragment numbers.

The fragment mass distribution is shown in the histogram of Fig. 3.18. The largest mass $m_{frag_{\max}}$ is 716 g, and the smallest $m_{frag_{\min}}$ is 1.133 g, it shows that minimum mass of fragment is 0.158% of maximum mass of fragment roughly. The typical fragment had a dimension of 5.9 cm, based on the average final thickness of the fragments, which is 10 times bigger than bullet usual in army.

The time trace of kinetic energy of AISI 9260 is shown in Fig. 3.19. The total kinetic energy KE_{case} increases to 11500 kJ at 140 μ s, and beyond this time, the kinetic energy is shown to remain constant.

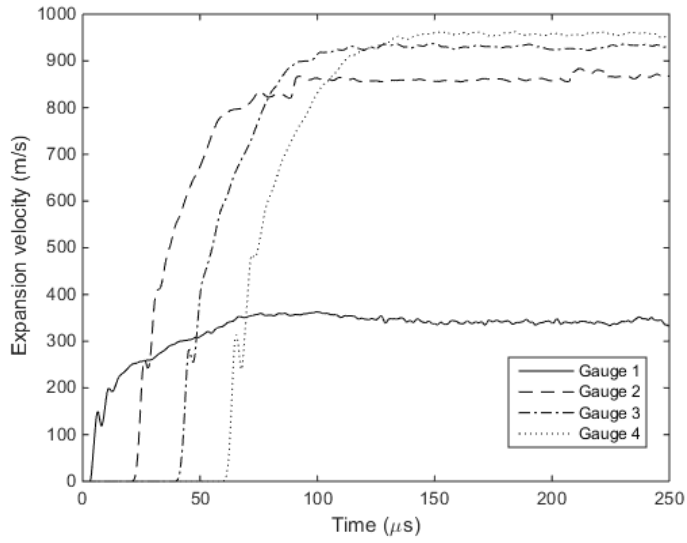


Fig. 3.16 Time history of expansion velocities of AISI 9260 in microsecond scale.

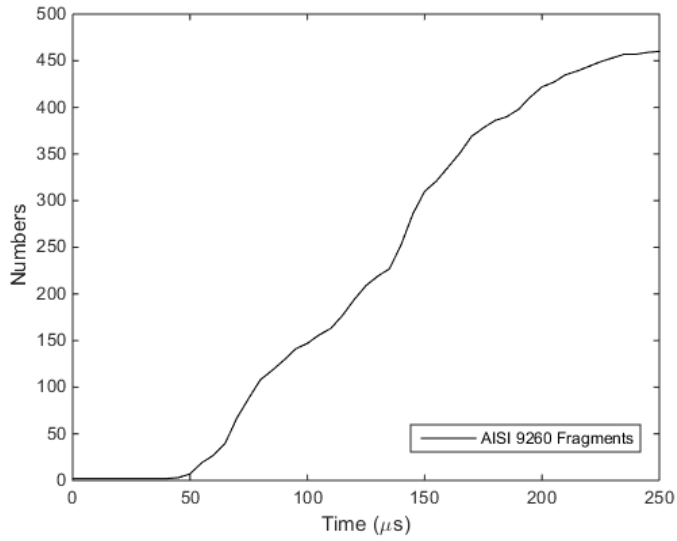


Fig. 3.17 Number of fragments recorded with respect to time.

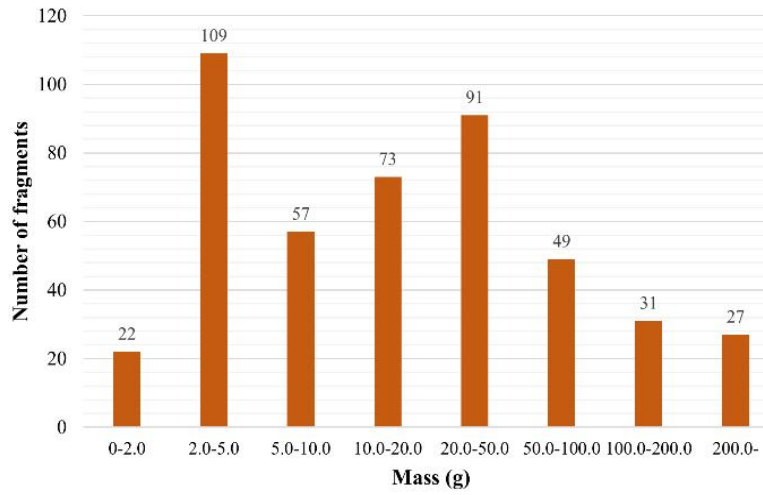


Fig. 3.18 Histogram of AISI 9260 fragment masses in fragmentation simulation.

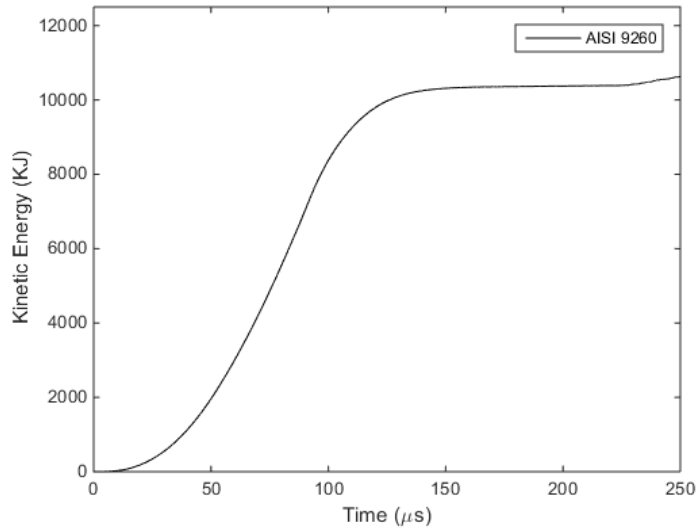


Fig. 3.19 Time history of kinetic energy of AISI 9260 casing in KJ.

3.5 Conclusion

A sympathetic detonation modeling that involves an explosive donor (PBXN-109), explosive or inert acceptors (sand), and AISI 9260 casing is investigated. The detonation of donor charge and the ensuing responses of nearby acceptors subjected to fragment impact and blast shock waves are simulated by a hydrodynamics with a set of constitutive equations for both reactive and inert components of the system. The modeling approach constructs a hydrodynamic model using the CHEETAH code while the constitutive relations were provided by JWL equation of state, and the chemical kinetics was elucidated through rate stick simulation. The stochastic failure model based on the Mott probability function is used to describe the fragmentation of steel casing as the impact of blast fragments and strong shock waves give rise to the initiation of acceptor charges. The pressure data and retrieved fragment size distribution from a full size sympathetic detonation test confirm the reliability of the present models.

CHAPTER 4

Analysis on Shock Attenuation in Gap Test

4.1 Background and objective

Pyrotechnic mechanical devices often utilize gap test configuration between a donor and an acceptor for reliable gas generation aiming at various “push-pull” actuations found in many industrial and military applications. Operability of such pyrotechnic systems depends on mechanical properties of the gap and shock sensitivity of donor-acceptor charges. A gap test is a standardized test to quantify the shock sensitivity of an acceptor that needs to be characterized. Critical gap thickness of a gap whose shock characteristics are known a priori is measured when the acceptor charge is detonated at its initiating pressure.

Gap test has advantage over other commonly used method for measuring shock sensitivity such as drop-weight impact test [1]. Critical gap thickness, under highly controlled circumstances, is quite reproducible with the error less than a fraction of a millimeter [2]. The test consists of four components: donor charge, gap, acceptor charge and a witness block. The four components train is first detonated at its donor usually by an electrical means. The shock wave generated by detonation is attenuated through the gap. The transmitted shock wave then may or may not trigger an acceptor depending on the level of

attenuation. If the acceptor is detonated, a hole is created at the witness block. Here, the gap thickness is adjusted and the test is repeated until a critical thickness (Go / No-go) is obtained for the test sample being the acceptor charge. A critical gap thickness for which the acceptor has 50% probability of being detonated, marks the shock sensitivity of the acceptor [3-5].

In this research, we attempt to define a multi-material hydrodynamic simulation for a Large Scale Gap Test (LSGT) comprising of a donor (Pentolite), a gap (PMMA), and an acceptor (heavily aluminized RDX). The aluminum-rich RDX is comprised of 50% RDX (cyclotrimethylene-trinitramine, $C_3H_6N_6O_6$), 35% aluminum powder and 15% HTPB (hydroxyl-terminated polybutadiene) binder. Its initial density after pressing is 1.78 g/cm^3 . The numerical simulation provides the complex shock interaction structure, the critical gap thickness, the acoustic impedance and the corresponding detonation characteristics of high explosives in contact with a PMMA gap. A full scale LSGT experiment is also conducted for validation of the numerical predictions provided in this study.

4.2 Numerical approach

In order to simulate the energetic material response at high temperature and pressure conditions, one requires reactive flow models, rupture model, multi-material interface tracking model and hydrodynamic model for accurate capturing of various waves inherent to a globally hyperbolic system. For both

energetic material and inert gap material, compressible form of the governing equations is used, and the stress tensor for inert solids is composed of deviatoric stress and hydrostatic pressure [6]. The Mie-Gruneisen equation of state (EOS) defines pressure of gap material, while the JWL (Jones-Wilkins-Lee) EOS is used for high explosives. The rate of chemical reaction is based on the ignition and growth steps previously built for the aluminized RDX [7]. The interface between two different materials is tracked through a hybrid particle level set method, and the material properties near the interface are determined through the ghost fluid method. Here, only a brief explanation of the method is outlined. For more detailed discussions, one may refer to Ref. 8.

4.2.1 Governing equations

The compressible Navier-Stokes equations in a cylindrical coordinate system reflect the conservations of mass, momentum and energy:

$$\frac{\partial \vec{U}}{\partial t} + \frac{\partial \vec{E}}{\partial r} + \frac{\partial \vec{F}}{\partial z} = \vec{S}(\vec{U}) \quad (1)$$

$$\vec{U} = \begin{bmatrix} \rho \\ \rho u_r \\ \rho u_z \\ \rho E \end{bmatrix}, \quad \vec{E} = \begin{bmatrix} \rho u_r \\ \rho u_r^2 + p \\ \rho u_r u_z \\ u_r(\rho E + p) \end{bmatrix}, \quad \vec{F} = \begin{bmatrix} \rho u_z \\ \rho u_z u_r \\ \rho u_z^2 + p \\ u_z(\rho E + p) \end{bmatrix} \quad (2)$$

$$\bar{S} = \begin{bmatrix} -\frac{\rho u_r}{r} \varphi \\ \frac{s_{rr} - s_{\theta\theta} - \rho u_r^2}{r} \varphi + \eta \left(\frac{\partial s_{rr}}{\partial r} + \frac{\partial s_{zr}}{\partial z} \right) \\ \frac{s_{zr} - \rho u_r u_z}{r} \varphi + \eta \left(\frac{\partial s_{rz}}{\partial r} + \frac{\partial s_{zz}}{\partial z} \right) \\ \frac{u_r s_{rr} + u_z s_{rz} - u_r (\rho E + p)}{r} \varphi + \eta \left(\frac{\partial (u_r s_{rr} + u_z s_{rz})}{\partial r} + \frac{\partial (u_r s_{zr} + u_z s_{zz})}{\partial z} \right) \end{bmatrix} \quad (3)$$

where $\varphi = 0, 1$ for rectangular and cylindrical coordinates respectively and $\eta = 0, 1$ for fluids (liquids and gases) and solids respectively. The governing equation is solved by a third-order Runge-Kutta and ENO (essentially non-oscillatory) method [8] with respect to the temporal and spatial discretizations, respectively. Here, the stress effect in the unreacted solid state can be ignored in comparison with the dominant hydrostatic pressure of the reacted gas state of high explosive. However, to capture the drastic change in deformation of the inerts, the Cauchy stress tensor is formulated into deviatoric stress tensor and hydrostatic pressure as follows:

$$\sigma_{ij} = s_{ij} - p\delta_{ij} \quad (4)$$

The rate of deviatoric stress change follows the first order differential equation:

$$\dot{s}_{ij} = \dot{s}_{ij,tr} + \dot{s}_{ij,cor} = \Omega_{ik} s_{kj} - s_{ik} \Omega_{kj} + 2G(\overline{D}_{ij} - D_{ij}^p) \quad (5)$$

$$\dot{s}_{ij,tr} = \Omega_{ik} s_{kj} - s_{ik} \Omega_{kj} + 2G\overline{D}_{ij} \quad (6)$$

$$\dot{s}_{ij,cor} = -H : D_{ij}^p = -2G\Lambda N_{ij,tr} \quad (7)$$

where each operator is defined as

$$\overline{D}_{ij} = D_{ij} - \frac{1}{3} D_{kk} \delta_{ij}, \quad D_{ij} = \frac{1}{2} \left(\frac{\partial u_i}{\partial x_j} + \frac{\partial u_j}{\partial x_i} \right), \quad \Omega_{ij} = \frac{1}{2} \left(\frac{\partial u_i}{\partial x_j} - \frac{\partial u_j}{\partial x_i} \right) \quad (8)$$

4.2.2 Constitutive relation

The shock Hugoniot for donor and Mie-Gruneisen for acceptor are used for EOS of the unreacted high explosive [9].

$$p_{unreacted(donor)} = A(\rho/\rho_0 - 1)^1 + B(\rho/\rho_0 - 1)^2 + C(\rho/\rho_0 - 1)^3 \quad (9)$$

$$p_{unreacted(acceptor)} = P_H + \Gamma\rho(e - e_H) \quad (10)$$

In particular, isentropic JWL C-term form is used for products, and is derived by assuming the process being isentropic [10].

$$P_{reacted}(\text{donor, acceptor}) = Ae^{-R_1(\rho_0/\rho)} + Be^{-R_2(\rho_0/\rho)} + C(\rho_0/\rho)^{-(1+\omega)} \quad (11)$$

As for the gap material, Mie-Gruneisen EOS is adopted to calculate the pressure of PMMA [11] as such,

$$P_{non-reactive(\text{PMMA})} = \Gamma_0 E + \begin{cases} \rho_0 C_0^2 \mu \left[1 + \left(1 - \frac{\Gamma_0}{2} \right) \mu \right] / \left[1 - (S_1 - 1)\mu - S_2 \frac{\mu^2}{\mu + 1} \right]^2 & \text{if } \mu > 0 \\ C_0^2 \rho_0 \mu & \text{if } \mu < 0 \end{cases} \quad (12)$$

where $\mu = \rho/\rho_0 - 1$.

The Johnson–Cook model is applied for flow stress or the minimum outer force needed to deform plastically. This model makes use of the equivalent plastic strain, strain rate, and melting temperature [12], such that

$$\sigma_Y = \left(A + B(\overline{\varepsilon}^p)^n \right) \left(1 + C \ln \left(\frac{\dot{\varepsilon}^p}{\dot{\varepsilon}_n} \right) \right) \left(1 - \frac{T - T_0}{T_m - T_0} \right) \quad (13)$$

Since PMMA is a brittle material under the present test, no strength model is used as such a constant yield stress is utilized [11]. In this research, we set the yield stress of PMMA to be constant unless its temperature is less than a melting temperature. If its temperature is higher than the melting temperature, then the yield stress is reduced to zero.

4.2.3 Chemical reaction of the high explosive materials

The reactive flow model is described by the rate law that consists of both ignition and growth terms suggested by Kim et al. [13]

$$\frac{d\lambda}{dt} = I(1-\lambda)\mu^a + G(1-\lambda)p^b, \quad \mu = \frac{\rho}{\rho_0} - 1 \quad (14)$$

Here p is pressure, t is time, ρ_0 and ρ are the initial and current densities, respectively. λ is the burned mass fraction, and constants I , a , G , b are the unknown parameters. λ is a reaction progress variable ($\lambda = 0$ unreacted state and $\lambda = 1$ reacted state) and the compression term, μ , is defined as ($\mu = \rho/\rho_0 - 1$). Four unknown parameters of major significance in view of detonation are determined by a series of standardized unconfined rate stick experiment performed previously [13].

4.2.4 Hybrid particle level set method

To obtain sharp interface between two different materials, hybrid particle level set method [14] is applied. The motion of the level set follows the equation [15, 16],

$$\frac{\partial \phi}{\partial t} + u_r \frac{\partial \phi}{\partial r} + u_z \frac{\partial \phi}{\partial z} = 0 \quad (15)$$

Here, the interface of each substance is a zero level set $\phi=0$. $\phi<0$ indicates inner and $\phi>0$ indicates outside of the material. This equation is integrated with a 4th order scheme in space and 3rd order Runge-Kutta method in time [17].

While calculating the interface level set function, a drastic change in the material property may give rise to distortion of the interface. To remedy this weakness, a periodic re-initialization is adapted by solving the following equation until steady state is reached.

$$\phi_t + S(\phi)(|\nabla\phi| - 1) = 0 \quad (16)$$

Here S is

$$S = \frac{\phi}{\sqrt{\phi^2 + (1 - |\nabla\phi|)^2} d^2} \quad (17)$$

with d being the grid size.

Basic information like unit normal vector or curvature can be obtained easily using the following relations.

$$\text{Unit normal vector: } \vec{n} = \frac{\nabla\phi}{|\nabla\phi|} \quad (18)$$

$$\text{Curvature: } \kappa = \nabla \cdot \vec{n} = \nabla \cdot \left(\frac{\nabla\phi}{|\nabla\phi|} \right) \quad (19)$$

The dissipation characteristics of ENO scheme and re-initializations of level set lead to interface round off errors and violation of mass conservation. In order to correct these issues for precise interface tracking, a hybrid particle level set method is applied [15, 16]. Here, two types of massless particles, positive and negative particles, are placed in the region of $\phi > 0$ and $\phi < 0$ respectively. These particles are allowed to advect following the equation.

$$\frac{d\vec{x}_p}{dt} = \vec{u}(\vec{x}_p) \quad (20)$$

where \vec{x}_p is the position of the particles and $\vec{u}(\vec{x}_p)$ is their velocity vector. The characteristic information of the flow is preserved due to deletion of the dissipation from the evolution equation.

Each particle has zero mass but has a volume. The radii of those particles are determined from the size of the grid as such, the maximum and minimum values are

$$r_{\min} = 0.1 \min(\Delta r, \Delta z) \quad (21)$$

$$r_{\max} = 0.5 \min(\Delta r, \Delta z) \quad (22)$$

Initially, the particles are randomly placed and then directed to the correct direction. Then the final radii for particles follow,

$$r_p = \begin{cases} r_{\max} & \text{if } s_p \phi(\vec{x}_p) > r_{\max} \\ s_p \phi(\vec{x}_p) & \text{if } r_{\min} \leq s_p \phi(\vec{x}_p) \leq r_{\max} \\ r_{\min} & \text{if } s_p \phi(\vec{x}_p) < r_{\min} \end{cases} \quad (23)$$

where s_p is the sign of the particle and sets to +1 if $\phi(\vec{x}_p) > 0$ and -1 if $s_p \phi(\vec{x}_p) < 0$, respectively. Here, if an error by the particles to move in the wrong direction with respect to the interface is detected, error correction through the local level set reconstruction is performed.

4.2.5 Ghost fluid method

The material properties change drastically across the interface between any two different materials. This is mainly due to the discontinuous entropy distribution at the interface that results in numerical truncation errors, which can be quite significant if not properly treated. In the present method, the

ghost cells are populated in the opposite of the real material of interest using the extrapolation while having the continuous entropy distribution. Here, the real discontinuous entropy distribution is merged with the entropy distribution of ghost cells and generates proper boundary conditions. The physical conditions are used in the ghost band where pressure and velocity are the same as the interface conditions. Then the entropy in the ghost band is assigned the value of the real material. All other remaining variables are determined through the entropy relation and the proper EOS [18, 19].

4.2.6 Interface conditions

At the interface, velocity components in the normal direction and stress fields must remain continuous following the conservation law as such that

$$\sigma_{nn}^{solid} = -P^{fluid}, \quad \sigma_{nt}^{solid} = 0, \quad v_n^{solid} = v_n^{fluid} \quad (24)$$

4.3 Modeling constants

The material properties and Mie-Gruneisen EOS constants are summarized in Table 4.1 [11]. The chemical reaction and pressure growth of the energetic materials are calculated from the reactive flow model with JWL EOS as listed in Table 4.2 [7, 9]. The JWL EOS parameters of product gas of pentolite are calculated with a thermo-chemical equilibrium code [19].

Table 4.1 Material properties for PMMA.

<i>Mechanical constant</i>		<i>Mie-Gruneisen EOS</i>	
Initial density (kg/m ³)	1182	C_0 (m/s)	2180
Young's modulus (GPa)	0.42	S_0	1.410
Shear modulus (GPa)	2.32	Gruneisen coefficient	0.85
<i>Thermal constant</i>		<i>Strength model</i>	
Specific heat capacity(J/kg·K)	1466	Constant yield stress (GPa)	0.42
Room temperature (K)	300		
Melt temperature (K)	330.3		

Table 4.2 Modeling constants for Pentolite and heavily aluminized RDX.

	Model parameter	Pentolite	Al-RDX
Reactant	ρ_0 (kg/m ³)	1560	1780
	A (GPa)	12.82	-
	B (GPa)	0	-
	C (GPa)	119.30	-
	C_0 (mm/ μ s)	-	2.60
	S	-	1.86
	Γ	-	0.99
Product	A (GPa)	507.91	2633.31
	B (GPa)	6.62	8.59
	C (GPa)	1.27	1.09
	R_1	4.62	6.68
	R_2	1.02	1.11
	w (J/g-K)	0.33	0.09
Chemical kinetics	I (s ⁻¹)	1.4×10^8	3.2×10^8
	a	4.0	4.0
	G (s ⁻¹ Mbar ^{-b})	3.3×10^8	3.5×10^7
	b	1.3	0.7
	p_i (GPa)	1.2	5.9

4.4 Results and validations

4.4.1 Shock attenuation in Donor-Gap configuration

We tested a combination of pentolite donor and PMMA gap to verify the shock generation and attenuation characteristics. The time evolution plot of the pressure profile along the centerline is shown in Fig. 4.1.

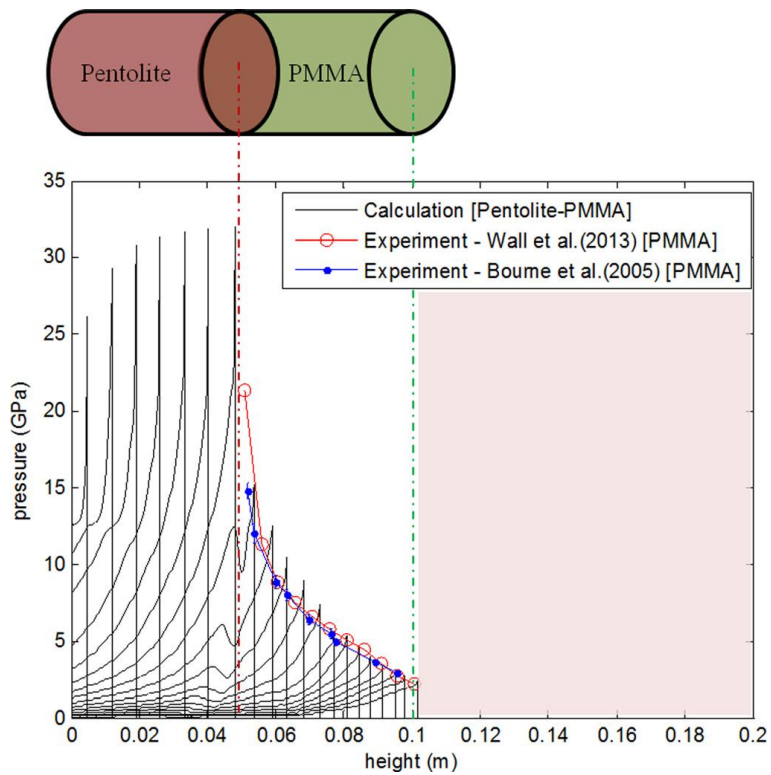


Fig. 4.1 Calculated shock pressure attenuation in Pentolite(donor)-
PMMA(gap).

Here, during the development of detonation wave, the von Neumann spike reaches approximately 31 GPa. The tendency of attenuation in the pressure is in good agreement with the LSGT data [21, 22]. The comparison of attenuating pressure is shown in table 4.3 which demonstrates that the prediction of shock sensitivity is quite precise.

Table 4.3 Comparison of shock attenuation.

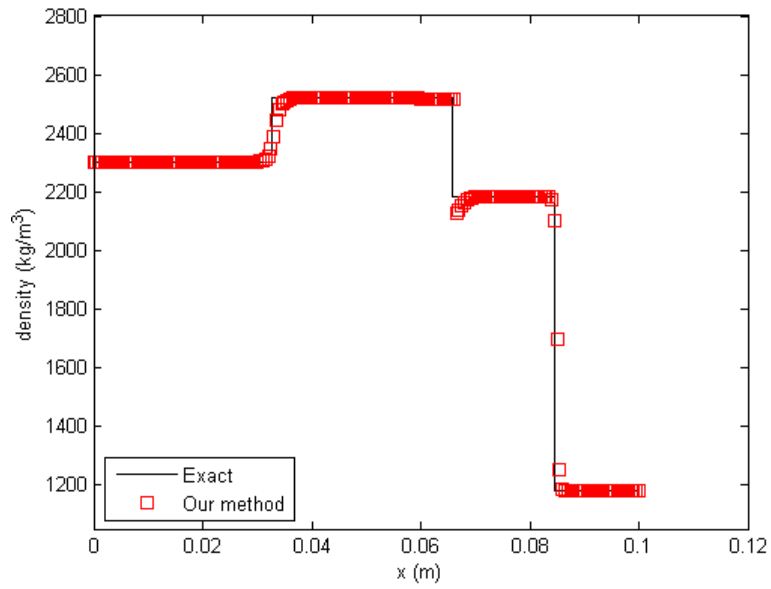
Height (m)	p_{cal} (GPa)	$p_{exp,Wall}$ (GPa)	$p_{exp,Boume}$ (GPa)
0.0535	13.71	12.79	12.23
0.0590	11.33	10.69	10.25
0.0635	9.483	8.939	8.977
0.0685	8.028	7.474	7.626
0.0730	6.641	6.477	5.971
0.0810	4.824	4.864	4.410
0.0845	4.121	4.215	4.091
0.0880	3.552	3.786	3.806
0.0915	3.113	3.281	3.415
0.0950	2.762	2.947	2.987
0.0980	2.463	2.647	2.609
0.1015	2.144	2.293	2.167
Error %		5.3	6.8

4.4.2 Interaction in Gap-Acceptor configuration

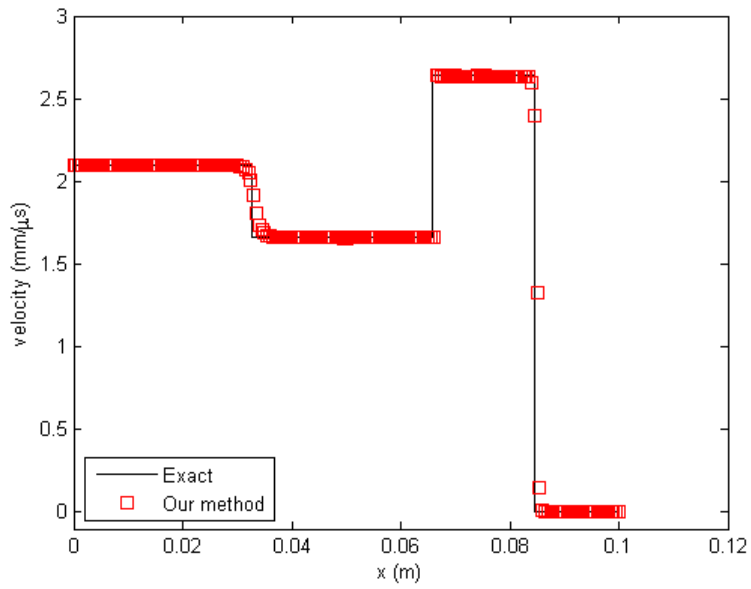
Handling of subtle motion between gap (PMMA) and acceptor (heavily aluminized RDX) is tested. One-dimensional Riemann problem, in which initial condition is given in Table 4.4, is solved and compared with the exact solution. The result with mesh size of 0.5 mm at 6 μs is shown in Fig. 4.2. The interface between PMMA and RDX at $x = 0.05$ m moves to $x = 0.065$ m while retaining a sharp discontinuity, thanks to the hybrid particle level set method used. Although minor undershoots are observed around the contact line (especially in the case of density), two shocks propagating through Acceptor and Gap are captured quite precisely.

Table 4.4 Initial parameters for a gap-acceptor problem.

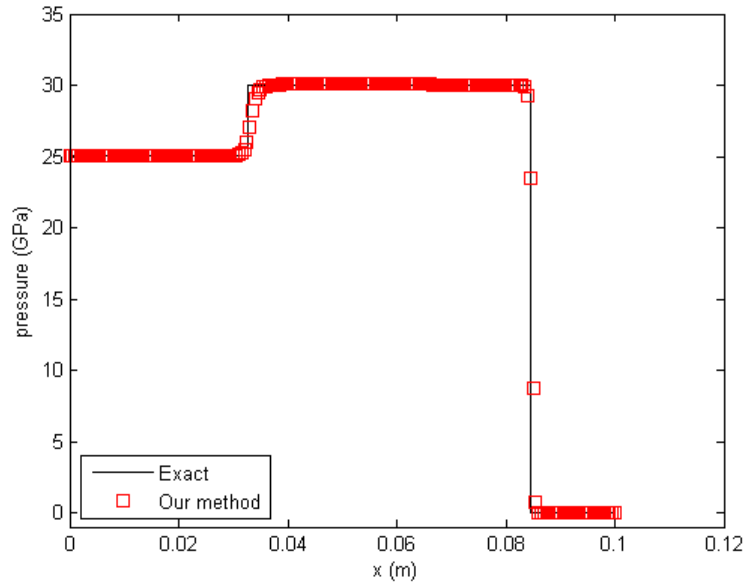
Working mediums	PMMA	Al-RDX
Density (kg/m^3)	1182	2300
Pressure (GPa)	0	25
Velocity ($\text{mm}/\mu\text{s}$)	0	2.1
Initial yield stress (GPa)	0.42	none
Shear modulus (GPa)	2.32	none
Strength model	Constant yield stress	none



(a) density



(b) velocity



(c) pressure

Fig. 4.2 Calculated results for Gap-Acceptor configuration at 6 μ s:

(a) density, (b) velocity, and (c) pressure.

4.4.3 Shock attenuation inside PMMA Gap

Shock attenuation through a PMMA gap is reproduced following the experimental LSGT data [23, 24]. The gap diameter of 5.08 cm is considered. The particle velocity following a shock wave is tracked along the central axis and plotted for each mesh size used in the simulation in Fig. 4.3. The present method is shown to capture the shock attenuation pattern in the PMMA quite well for all grid resolutions considered. The mesh size of 0.1 mm \times 0.1 mm is suggested for all future gap test simulation.

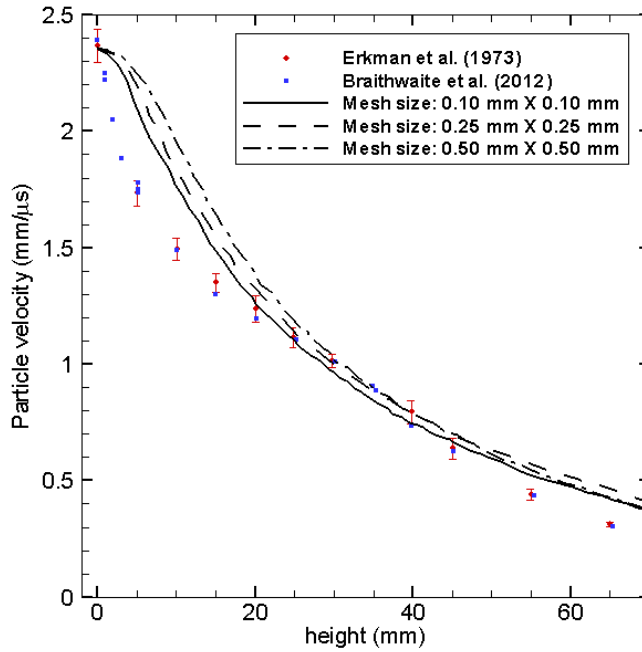


Fig 4.3. Mesh refinement test via particle velocity.

4.4.4 LSGT of Pentolite-PMMA-Aluminized RDX

The large-scale gap tests were conducted. The length of gap substance was varied to observe the critical gap thickness until acceptor is detonated in 50% of the trials. The donor charge is Pentolite whose initial density is 1.56 g/cm^3 , and the acceptor is heavily aluminized RDX of its initial density 1.78 g/cm^3 . The gap is provided by stacking PMMA discs to adjust its thickness height. All materials were shaped into a 50.8 mm diameter circle. The height of donor is 50.8 mm and that of acceptor is 139.7 mm. The gap length was varied. The gap test specimen and configuration are shown in Fig. 4.4.

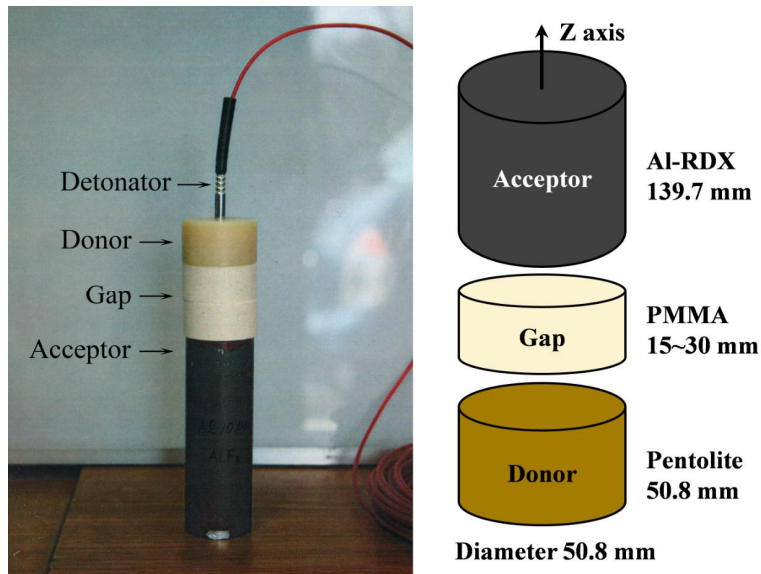


Fig 4.4 Gap test configuration.

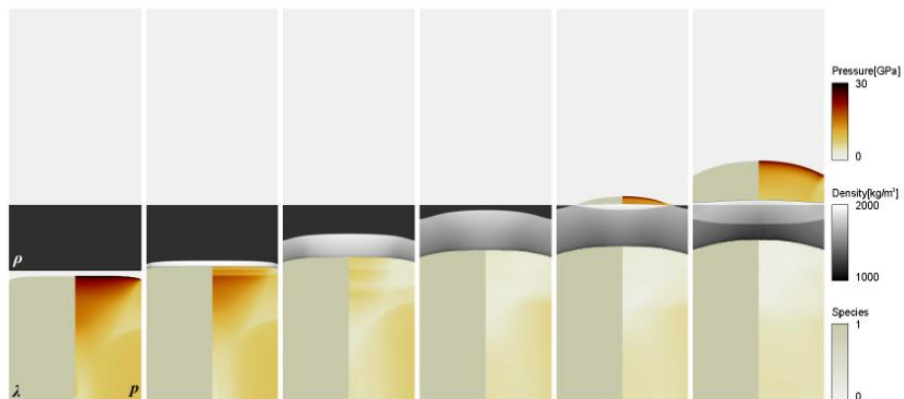
Three trials are conducted at gap thicknesses varied by 0.254 mm interval. Go / No-go criterion is obtained until the witness plate breakage. From the experiment, the critical thickness was found to be 25.75 mm as any thicker value resulted in undamaged witness plate. Table 4.5 lists the LSGT experimental result.

Table 4.5 LSGT experimental result.

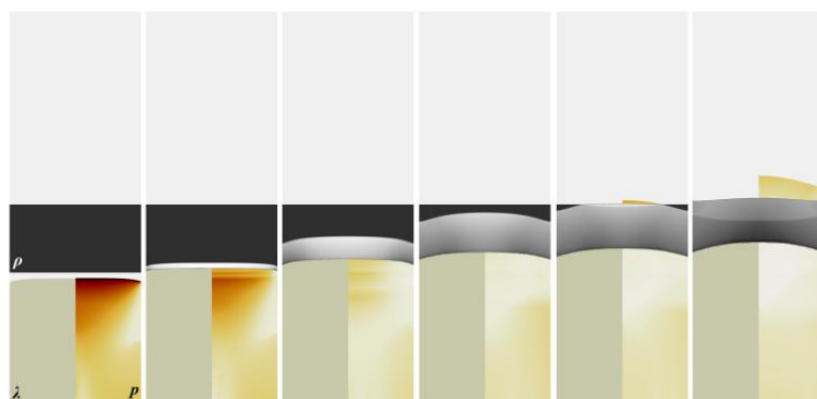
PMMA gap thickness	Go/No go
24.480 mm	Go
24.734 mm	Go
24.988 mm	Go
25.242 mm	Go
25.496 mm	Go
25.750 mm	Go/No go
26.004 mm	No go
26.258 mm	No go
26.512 mm	No go
26.766 mm	No go
27.020 mm	No go

The schematic of the gap test simulation is shown at the right hand side in Fig. 4.4. The gap sizes are varied from 15 mm to 30 mm with 1 mm interval. Pentolite cylinder block with height of 50.8 mm and Al-RDX cylinder block of height 139.7 mm are modeled in a computational domain of 190.5 (+ gap height) mm. As for the initial condition for detonating a donor charge, 1 km/s impact is applied at the bottom. All other outer boundaries are unconfined.

The gap size is varied from 15 mm to 30 mm. The full simulation of the gap test for 25 and 26 mm is shown in Fig. 4.5. For clear illustrations, reaction progress variable (λ) and pressure are used for explosive charges (donor and acceptor) while density is used for PMMA. Pentolite is shown below the PMMA gap, and aluminized RDX is above. The subsequent initiation of acceptor then determines the sensitivity of the acceptor in the LSGT.



(a) Go Case at 25 mm PMMA thickness



(b) Nogo Case at 26 mm PMMA thickness

Fig. 4.5 Shown reaction progress and pressure for donor (bottom)/acceptor (top), density for PMMA (middle). (a) 25 mm Gap and (b) 26 mm Gap at times $t = 7, 8, 10, 12, 13,$ and $15 \mu\text{s}$.

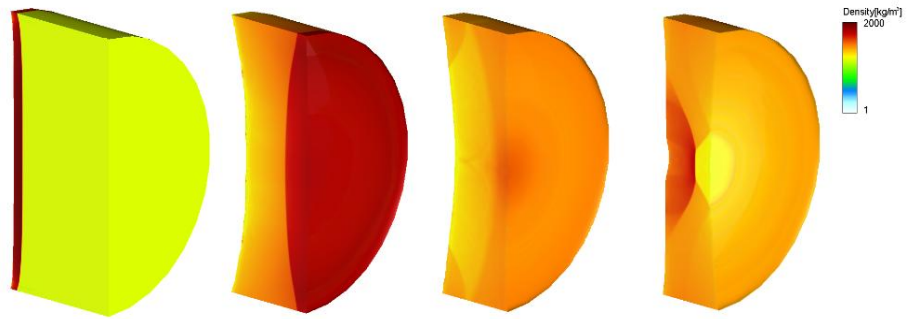
There are LSGT experimental data presented by Wall et al. [21] and Bourne et al. [22] where they measured the shock attenuation through PMMA. In Erkman et al. [23] and Braithwaite et al. [24], the peak particle velocities against gap thickness have been appraised. Our LSGT experiment has provided the critical gap thickness of an aluminized RDX acceptor, in a form that is rather brief but simplified for use in the computational research. The hydrodynamic simulation on the peak pressure histories and particle velocity curves shown in Figs. 4.1 and 4.3 are in good agreement with the experimental data, including both the detonation pressure of energetic materials and its attenuation within the non-reactive materials.

Figure 4.5 shows how the donor detonation wave is attenuated through the gap depending on PMMA thickness. The Go / No-go of acceptor is determined. A full set of reactive compressible equations of two energetic materials are solved while comprehensive stress field calculation is used to accurately track the evolution of PMMA undergoing its shape change. The go case in (a) shows the initiation of acceptor with initiating pressure shown in several GPa ranges, where as in (b) the no-go case is shown with diminishing pressure following pressure attenuation leaving the gap. The importance of the equation of state for materials involved in LSGT is of particular interest. The precise capturing of the gap thickness for Go / No-go is also due to resolving the impedance mismatch between reactive medium and inert, namely PMMA. At 26 mm, the detonation failure might have occurred

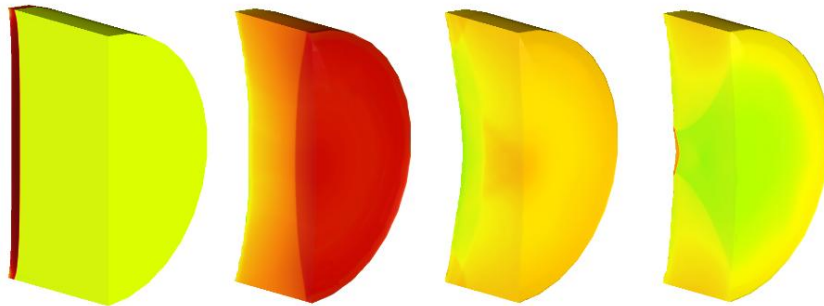
because such critical gap thickness (t_c) must lie somewhere below this thickness, namely 25 mm.

The shape change of PMMA during the test is quite interesting. As the pressure is less attenuated in 25 mm case as such most of the donor pressure is transmitted to the acceptor, causing a higher compression of the gap during successive acceptor initiation. The density of the deformed gap in Fig. 4.6(a) remains higher than nogo case shown in 4.6(b). Under the condition that the gap length is relatively short, transmitted shock pressure becomes increasingly high near the central axis of the acceptor due to highly reactive detonation front in the center. The resulting curvature of PMMA is therefore concave up or down as shown in Fig. 4.6(a) and 4.6(b).

The time trace of consecutive pressure profiles along the centerline of LSGT simulation with 25 mm PMMA gap which is a Go and 26 mm No-go are shown in Fig. 4.7. The initial shock pressure at the Pentolite donor is about 31 GPa. The shock is attenuated through the gap. When donor shock triggers the acceptor charge, the initiating pressure (p_i) of the acceptor was approximately at 5.9 GPa.

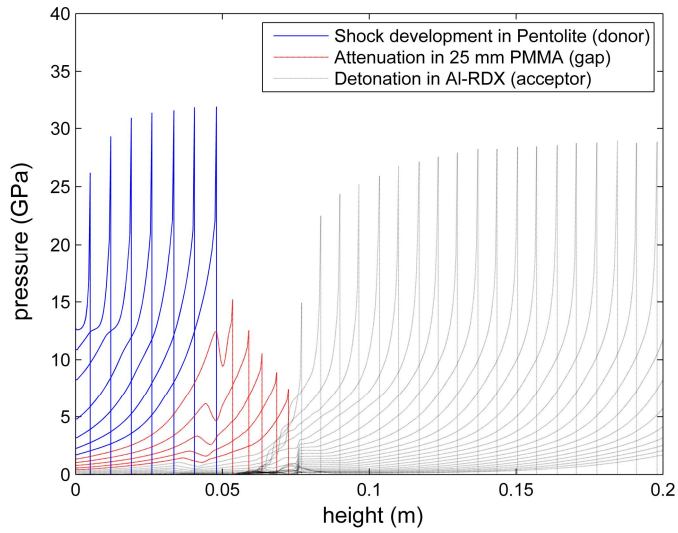


(a) Go Case – Initial PMMA thickness of 25 mm

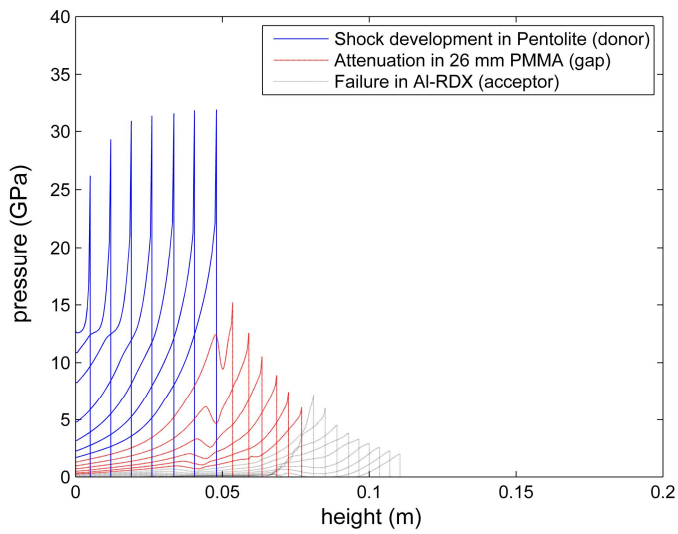


(b) Nogo Case – Initial PMMA thickness of 26 mm

Fig. 4.6 Shape evolution of PMMA during shock attenuation: (a) Initial PMMA thickness of 25 mm and (b) Initial PMMA thickness of 26 mm at times 8, 14, 20, and 26 μ s.



(a) 25 mm thickness gap



(b) 26 mm thickness gap

Fig. 4.7 Time trace of consecutive pressure profiles of LSGT simulation with 25 mm and 26 mm gap thickness.

4.4.5 Impedance calculation for validation

For the impedance analysis, the considered LSGT test near the contact between gap and high explosive is assumed one-dimensional. The acoustic impedance calculation becomes quite effective in providing a secondary view on the Go / No-go prediction from LSGT test in addition to a standardized pressure calculation.

Figure 4.8 shows reflection and transmission of a plane wave incident on contact surface between the two different matters with distinct impedance.

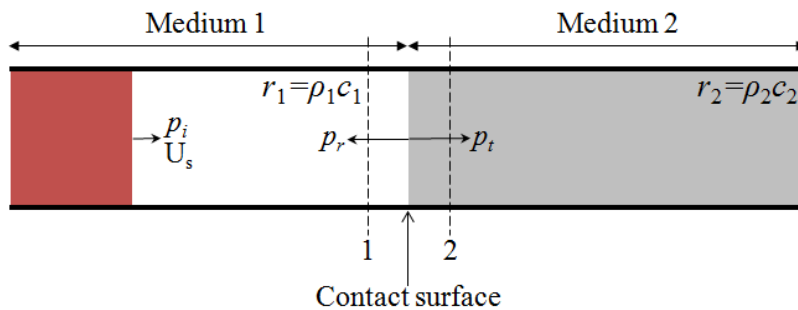


Fig. 4.8 Jump in the acoustic impedances.

The ratios of the pressure amplitudes and intensities of the reflected and transmitted waves depend on the characteristic acoustic impedance and the speed of sound in the two media. The incident and reflected waves travel in the first medium of characteristic acoustic impedance $r_1 = \rho_1 c_1$, where ρ_1 and c_1 are the equilibrium density and the speed of sound in the first medium, respectively. The transmitted wave travels in the second medium whose

characteristic acoustic impedance is $r_2 = \rho_2 c_2$. If pressure amplitude of the incident wave is p_i , those of the reflected and transmitted are p_r and p_t , respectively. Therefore, one can define pressure transmission and reflection coefficients using the following equations [25] :

$$T = p_t / p_i \quad (25)$$

$$R = p_r / p_i \quad (26)$$

The boundary conditions need to be satisfied at all times on the contact surface as such the pressure and particle velocity on both sides of the surface must equal to each other:

$$p_i + p_r = p_t \quad (27)$$

$$u_i + u_r = u_t \quad (28)$$

Division of (27) by (28) yields

$$\frac{p_i + p_r}{u_i + u_r} = \frac{p_t}{u_t} \quad (29)$$

Since the continuity of acoustic pressure across the surface demands $p/u = r$, (29) becomes

$$r_1 \frac{p_i + p_r}{p_i - p_r} = r_2 \quad (30)$$

which leads directly to the transmission and reflection coefficients [26]

$$T = \frac{\rho_2 c_2 + \rho_2 c_2}{\rho_2 c_2 + \rho_1 c_1} = \frac{r_2 + r_2}{r_2 + r_1} \quad (31)$$

$$R = \frac{\rho_2 c_2 - \rho_1 c_1}{\rho_2 c_2 + \rho_1 c_1} = \frac{r_2 - r_1}{r_2 + r_1} \quad (32)$$

Here, T-R equals 1. Thus if $\rho_1 c_1 = \rho_2 c_2$, acoustic wave will not be reflected at the contact surface.

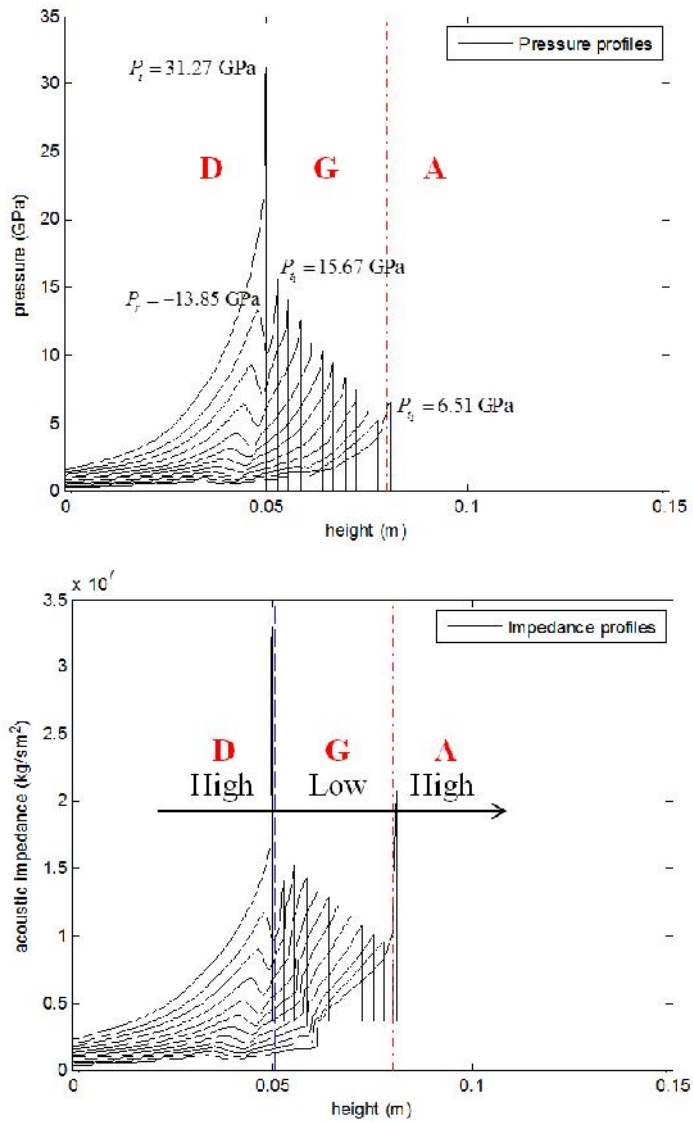


Fig. 4.9 Pressure and acoustic impedance of LSGT configuration (Donor, Gap, Acceptor).

Pressure and acoustic impedance profiles at the contact interfaces of LSGT are plotted in Fig. 4.9. The incident pressure is approximately 31.27 GPa right before the impact on the first contact. Subsequently the incident wave is split into two, namely 15.67 GPa transmitted and 13.85 GPa reflected waves. Here, the negative sign represents the direction of the wave propagation.

As the wave is propagated, the intensity of impedance varies from high to low and back to high again, going through two contact interfaces. Based on eq. (32), reflection coefficient is positive when $r_2 < r_3$, but, negative when $r_1 > r_2$. Consequently, at the interface the acoustic pressure of the reflected wave is either in phase or 180° out of phase with the incident wave. When the acoustic impedance of the third medium is greater than that of PMMA, a positive pressure in the incident wave is reflected as a positive pressure. On the other hand, if $r_1 > r_2$, a pressure is reflected backwards. When $r_1 = r_2$, reflection coefficient equals 0, and such all is transmitted. Transmission coefficient being the ratio between incident pressure and transmitted pressure is calculated to be 0.52 while reflection coefficient is a bit less, -0.48. The summation of these coefficients equals one as discussed.

The acoustic impedance ($Z = \rho c$) calculation becomes quite effective in providing a view of the development of rarefaction waves from LSGT test in addition to a standardized pressure calculation. Figure 4.5 shows the interactions between reflected and transmitted waves incident on the contact surface between the two different materials with distinct impedances. It is

noted that the shape deformation of the gap geometry occurs. The geometry of the attenuating gap is changed from a square-type cylinder to (compressed) concaved cylinder structure bent upwardly. This deformation as well as the shock bouncing inside the gap can be easily distinguished in Fig. 4.5. In Fig. 4.5, the shock wave is oscillating between the upper interface and the lower interface. Meanwhile, various shock waves interact together to form a complex shock structure inside the gap as shown after 20 μs . These various rarefaction waves are generated by reflection from the deformed upper/lower surfaces. The transmission and reflection from the surfaces are due to the impedance mismatch between inert material (PMMA) and energetic materials.

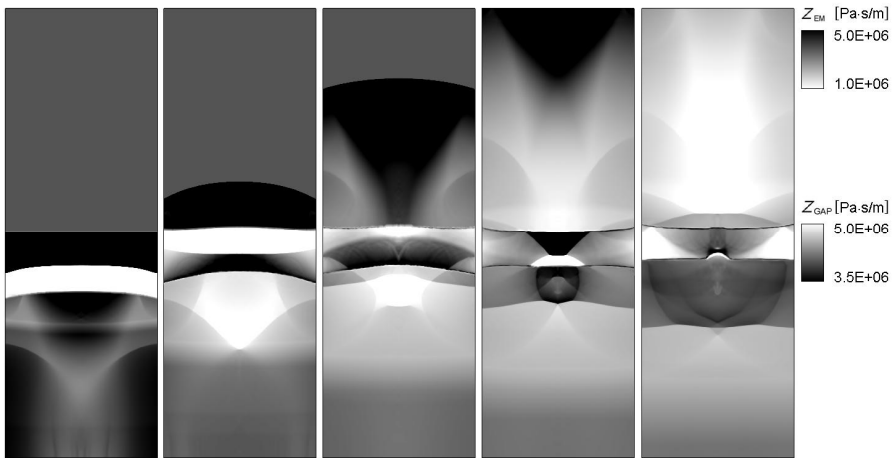


Fig. 4.5 Timed images of acoustic impedance ($Z = \rho c$) at Go case of LSGT simulation at times $t = 10, 15, 20, 25,$ and $30 \mu\text{s}$.

4.5 Conclusion

We have presented a modeling strategy necessary for accurately reproducing the large scale gap test result for characterizing the heavily aluminized RDX. The methodology for such numerical calibration of shock pressure attenuation within the gap is quite straight forward assuming the models are properly implemented and solved in the well-formulated hydrodynamic shock physics code. The present strategy can also accommodate any other type of non-ideal energetic materials (acceptor) subject to a precise characterization.

CHAPTER 5

Pyrotechnic Combustion in Closed Bomb Chamber

5.1 Background and objective

The analysis of pyrotechnic mechanical actuation requires a full-scale, fully-integrated dynamic simulation of fluid-solid, combustion of explosives and propellants in a train configuration. The reaction of a solid-phase energetic material must be precisely calculated before transferring subsequent dynamic loading onto a contacting inert structure such as a metal or plastic that is commonly in contact with another energetic material in a so called train configuration. A pyrotechnic mechanical device (PMD) is typically devised with several energetic components together with inert gap materials that often play the role of shock pressure attenuator for various applications. Airbag inflator is a common example that relies on this multi-material energetic-inert composite design that ultimately works as a single system to achieve rapid release of high pressure gas intended for inflating the airbag for automobile safety, for instance.

The work of multi-material modeling and simulation is a daunting task for any single-phase hydrodynamic code or Lagrangian structural code.

Conventional multi-phase solvers also fall short of handling such task that require precise capturing of dynamic interface between the reacting energetic material and inert, and resolving explosively fast time scale of chemical reaction associated with energetic substances that need to be experimentally calibrated and modeled to reproduce a series of standardized calibration tests of military standards. To do so, a solver must be written in fully integrated framework that strongly interacts between fluid and solid, and in addition, the reaction models must be built for each energetic material of unique composition and calorimetric properties. The utilized numerical methods must be of high order to track the rapid temporal transition during the chemical reaction and stable for smoothly linking the strain dynamics requirement from inert, elastic and plastic neighboring domain.

One needs to adapt a stable, multi-material interface handling algorithm based on a strongly-coupled fluid-structure interaction framework while accurately solving the chemical response of the involved high explosives, propellants, and reactive (powder) components. In addition, the equations of state for each energetic material as well as the inert materials need to be modeled to reproduce the full scale test of the energetic system in a train configuration.

Rider and Kothe [1] published a paper on volume of fluid methods which is one of the multi-material handling in a special issue of the Journal of Computational Physics on interfaces. The algorithm for the volume tracking

of interfaces is based upon a volume evolution equation that utilizes local discrete material volume and velocity data to track interfaces of arbitrarily complex topology. In 2002, D. J. Benson [2] addressed an issue on interface reconstruction methods using Level set methods and volume of fluid methods. Level set methods are comparatively new, and conceptually similar to a contouring algorithm function, with the zero contour level defining the material interface, is updated every time step from the particle velocities. Volume of fluid methods reconstructs the material interfaces based on the volumes fractions of the materials in an element and its neighboring elements. The volume of fluid methods, however, approximate the material interface as a line or plane within an element based on piecewise linear interface calculation methods. So, the author mentioned that an ability to model equilibrium point, which can currently be modeled with level set methods, is highly desirable. Harman et al. [3] solved a tightly coupled fluid-structure interaction problem on explosion of confined energetic materials using a multi-material formulation integrated with a Lagrangian, particle based, solid mechanics technique, known as the material point methods, as described by Kashiwa et al. [4] and Guilkey et al. [5]. This work successfully illustrates the algorithm's capabilities with regards to mass exchange among materials, large deformations, and the handling of multiple materials for a cylindrical copper container filled with a PBX explosive. Also, Guilkey et al. [6] shows an approach known as the material point method which is applicable to a wide

range fluid-structure interaction scenario via the simulation of explosions of energetic devices. The highly pressurized gaseous products of the energetic material lead to large deformations at strain rates in the cases of cylindrical rate stick test, metal contained cook-off test, shock tube test, and shaped charge test [7]. Recently, the multi-material numerical simulation for energetic system that consists of a high explosive charge and an inert confinement was carried out with an accurate and state-of-the-art Eulerian method by Kim and Yoh [8]. An explosively driven copper tube results in a state of high speed structural response of metal due to a detonating high explosive and a new particle level set based reactive ghost fluid method that imposes exact boundary conditions at the material's interface according to physical restraints is used to simulate the multi-material detonation problem. Level set method based sharp interface is developed for solution of moving boundary problems on fixed Cartesian grids. Kapahi et al. [9] describes the sharp interface Eulerian approach to high-speed multi-material dynamics using level sets that are used to define the objects immersed in the flow field and a modified ghost fluid method that is used for interface treatment of embedded objects. Comprehensively, level set algorithm (moving and deforming) with handling of the ghost fluid method have proven to be robust and reasonably accurate for multi-material interface handling, also represents a significant advance in the capability of compressible multi-material flows to resolve the material interfaces.

A small-scale gap test (SSGT) can be tested with a small amount of sample at a scale of about 1/10 times smaller than large-scale gap test (LSGT) by reducing the diameter to 5 mm. SSGT is tested by filling the thick (~ 10 mm) restrained shell of brass metal so that the detonating pressure does not disperse in the space but reaches the maximum capacity of the acceptor explosive through the gap material. LSGT is unconstrained or SSGT uses confined rate sticks. Therefore, it is possible to more precisely judge the shock sensitivity of the acceptor when considering the compositive interactions between reactants and non-reactants, such as shock pressure attenuation in the gap and deformation of the non-reactive materials.

Studies on the sensitivity of explosive using SSGT have been conducted mainly at NOL (Naval Ordnance Laboratory) and LLNL (Lawrence Livermore National Laboratory). Price et al. [10] of NOL compared the measured results of SSGT and LSGT to allow mutual calibration of the initiating threshold pressure. Souers et al. [11] of LLNL analyzed trends of initiating threshold pressure derived from flyer impact and gap tests for various energetic materials. However, the demand for numerical methodology has been steadily increasing because of the high cost and high risk of explosion experiments. In the experiment, it is thought that the numerical analysis can contribute to the internal flow phenomenon for shock wave generation and transfer process which is difficult to measure.

A closed bomb test is used to further validate the response of a pyrotechnic

device, consisting of donor, bulkhead, acceptor, and pyrotechnic propellant, connected with a 10 cc pressure sealed vessel. The explosive train configuration is filled with pyrotechnic charges of HNS+HMX, STS, RDX, and BKNO₃. HNS takes a role of a primer and HMX generates the incident pressure as a booster. The shock wave generated from the donor is undergoes attenuation through the STS bulkhead. It causes ignition when the transmitted wave reaches RDX acceptor. Thus, this is a sympathetic chain reaction of sequential explosives up to BKNO₃. It is important to verify that the explosive train properly demonstrates working performances as a through bulkhead initiator (TBI). Because the sympathetic pressure to be transferred to acceptor charge depends on the thickness of the bulkhead, a proper analysis is needed for accurate prediction of shock-to-detonation transition of a series of high energetic materials arranged in the explosive train. In order to quantify the detonation response of a high explosive in a pyrotechnic device by shock impact, it is necessary to clarify the relationship between ignition sensitivity and threshold pressure.

In this research, we attempt to conduct a multi-material hydrodynamic simulation for a Small Scale Gap Test (SSGT) using RDX acceptor that is comprised of 97.5% RDX (cyclotrimethylene-trinitramine, C₃H₆N₆O₆), 0.5% polyisobutylene, 0.5% graphite and 1.5% calciumstearite. Its initial density after pressing is 1.65 g/cm³. A series of Small Scale Gap Test (SSGT) and detailed hydrodynamic simulation are conducted to quantify the shock

sensitivity of an acceptor that contains 97.5% RDX. The methodology for such numerical prediction of shock propagation is quite straight forward if the models are properly implemented and solved in a well-formulated shock physics code. Also, a full-scale numerical simulation which necessary to accurately reproduce shock-induced detonation is conducted to analyze the pyrotechnic combustion of a pyrotechnic initiator in Closed Bomb Test (CBT) chamber that involves detonation of a composite donor (HNS+HMX), high pressure attenuation in a gap (STS), detonation of an acceptor (RDX), and finally a deflagration of a gas-generating propellant (BKNO₃). The present train configuration of two-dimensional layers of energetic-inert materials is designed for purging high pressure gas into a 10 cc dump chamber for subsequent monitoring of the flow oscillation due to inherent shock and rarefactions. A closed bomb test is also used to validate the full-scale simulation results provided in the study.

5.2 Numerical approach

In order to simulate the energetic response of high explosive and propellant contained in a donor-acceptor arrangement in stainless steel casing, the mathematical formulation is required to include reactive flow models for both detonation and deflagration, rupture model for metal, multi-material interface tracking model, and hydrodynamic model for accurate capturing of various acoustic waves inherent to a globally hyperbolic system. When the external

shock impact to a heterogeneous explosive is sufficiently large, the shock is able to grow to detonation. This process is known as shock-to-detonation transition. A shock impact which is superior to the threshold initiating pressure should be applied to an energetic material for successful SDT. The SDT phenomenon of energetic materials appears within the microsecond time scale ($\sim\mu\text{s}$) as such the comparatively tardier process namely thermal conduction, viscous dissipation are neglected. In effect, the time scale on the detonating chemical reaction is very fast compared to the time scale of the phenomena occurring in the fluid dynamics. Since detonation waves generally propagate at thousands of m/s, the assumption that molecular diffusion, heat conduction and viscous dissipation can be ignored in the problem dealing with shock and detonation physics is reasonably acceptable. For subsonic flows, pressure disturbances travel faster than the flow speed. If supersonic flows like detonation or shock, pressure disturbances can not travel upstream. Limited zone of influence is a characteristic of hyperbolic problems.

The dynamic response of both energetic and inert components of the given system is described by the compressible form of the governing equations, and the stress tensor that describes the structural response of steel is comprised of a deviatoric stress and a hydrostatic pressure [8]. The Mie-Gruneisen equation of state (EOS) defines the pressure attained by the gap between donor-acceptor high explosive pair, while the Jones-Wilkins-Lee (JWL) EOS determines explosive pressure resulting from the hydro-thermodynamic state.

The rate of chemical reaction is based on the ignition and growth kinetics [12]. The material interface between any two materials is tracked through a hybrid particle level set method, while material properties in the vicinity of an interface are determined through the ghost fluid method. For more detailed discussions, one may refer to Ref. 13.

5.2.1. Governing equations

The compressible Navier-Stokes equations in two-dimensional system reflect the conservations of mass, momentum and energy:

$$\frac{\partial \vec{U}}{\partial t} + \frac{\partial \vec{E}}{\partial r} + \frac{\partial \vec{F}}{\partial z} = \vec{S}(\vec{U}) \quad (1)$$

$$\vec{U} = \begin{bmatrix} \rho \\ \rho u_r \\ \rho u_z \\ \rho E \end{bmatrix}, \quad \vec{E} = \begin{bmatrix} \rho u_r \\ \rho u_r^2 + p \\ \rho u_r u_z \\ u_r(\rho E + p) \end{bmatrix}, \quad \vec{F} = \begin{bmatrix} \rho u_z \\ \rho u_z u_r \\ \rho u_z^2 + p \\ u_z(\rho E + p) \end{bmatrix} \quad (2)$$

$$\vec{S} = \begin{bmatrix} -\frac{\rho u_r}{r} \varphi \\ \frac{s_{rr} - s_{\theta\theta} - \rho u_r^2}{r} \varphi + \eta \left(\frac{\partial s_{rr}}{\partial r} + \frac{\partial s_{zr}}{\partial z} \right) \\ \frac{s_{zr} - \rho u_r u_z}{r} \varphi + \eta \left(\frac{\partial s_{rz}}{\partial r} + \frac{\partial s_{zz}}{\partial z} \right) \\ \frac{u_r s_{rr} + u_z s_{rz} - u_r(\rho E + p)}{r} \varphi + \eta \left(\frac{\partial(u_r s_{rr} + u_z s_{rz})}{\partial r} + \frac{\partial(u_r s_{zr} + u_z s_{zz})}{\partial z} \right) \end{bmatrix} \quad (3)$$

where $\varphi = 0$ for rectangular and $\varphi = 1$ for cylindrical coordinates. Also, $\eta = 0$ for energetic materials while $\eta = 1$ for inert (metal) materials. The resulting hyperbolic system of equations is solved by a third-order Runge-Kutta and ENO (essentially non-oscillatory) methods [14] for temporal and spatial discretizations, respectively. Here, stress effect in the unreacted high explosives or propellant is ignored in comparison to a dominantly high hydrostatic pressure resulted from the reacted product gases. However, to capture the drastic change in deformation of the inerts, the Cauchy stress tensor is formulated into deviatoric stress tensor and hydrostatic pressure as follows:

$$\sigma_{ij} = s_{ij} - p\delta_{ij} \quad (4)$$

where σ_{ij} is Cauchy stress tensor. Deviatoric stress tensor, s_{ij} , and the hydrostatic pressure, p , taken to be positive in compression.

$$\varepsilon = \varepsilon^e + \varepsilon^p, \quad \varepsilon'{}^p = \varepsilon_{ij}^p - \frac{1}{3}\varepsilon_{kk}^p\delta_{ij} = \varepsilon_{ij}^p, \quad \bar{D}_{ij} = D_{ij} - \frac{1}{3}D_{kk}\delta_{ij} \quad (5)$$

where ε is the strain tensor, ε^e and ε^p are the elastic strain tensor and the plastic strain tensor, respectively. $\varepsilon'{}^p$ is the plastic deviatoric strain tensor, D_{ij} and \bar{D}_{ij} are the strain rate tensor and the deviatoric strain rate tensor, respectively.

We assume that $\varepsilon_{kk}^p = 0$, plastic incompressibility.

$$I_1 = \sigma_{11} + \sigma_{22} + \sigma_{33}, \quad J_1 = s_{kk} = s_{11} + s_{22} + s_{33} = \sigma_{kk} + p\delta_{kk} = 0 \quad (6)$$

A Huber-von Mises yield function for von Mises material with isotropic hardening is given by

$$f = f(\sigma, \sigma_v) = f(s_{ij}, \bar{\sigma}) = \sqrt{\frac{3}{2} s_{ij} s_{ij}} - \sigma_v \approx \sqrt{s_{ij} s_{ij}} - \sqrt{\frac{2}{3}} \sigma_v \leq 0 \quad (7)$$

where $\bar{\sigma}$ is the effective stress and σ_v is the current yield stress.

Let define the effective stress $\bar{\sigma}$ and the effective plastic strain $\bar{\varepsilon}^p$ as follows:

$$\bar{\sigma} = \sqrt{\frac{3}{2} s_{ij} s_{ij}} = \sqrt{\frac{3}{2} (s_{11}^2 + s_{22}^2 + s_{33}^2 + 2(s_{12}^2 + s_{23}^2 + s_{31}^2))} \quad (8)$$

$$\dot{\bar{\varepsilon}}^p = \sqrt{\frac{2}{3} D_{ij}^p D_{ij}^p} = \sqrt{\frac{2}{3}} \Lambda \quad (9)$$

with Λ is a positive parameter called the consistency parameter and D_{ij}^p the plastic strain rate tensor.

In the cases of cylindrical coordinate or axisymmetric problem, the effective plastic strain is express as;

$$\bar{\sigma} = \sqrt{\frac{3}{2}(s_{rr}^2 + s_{\theta\theta}^2 + s_{zz}^2 + 2s_{rz}^2)} = \sqrt{3(s_{rr}^2 + s_{zz}^2 + s_{rr}s_{zz} + s_{rz}^2)} \quad (10)$$

Deviatoric stresses of evolution equation are as follows.

$$\dot{s}_{rr} = \Omega_{rz}s_{zr} - s_{rz}\Omega_{zr} + 2G\left(\frac{\partial u}{\partial r} - \Sigma - D_{rr}^p\right) = 2s_{rz}\Omega_{rz} + 2G\left(\frac{\partial u}{\partial r} - \Sigma - D_{rr}^p\right) \quad (11)$$

$$\dot{s}_{zz} = \Omega_{zr}s_{rz} - s_{zr}\Omega_{rz} + 2G\left(\frac{\partial v}{\partial z} - \Sigma - D_{zz}^p\right) = -2s_{rz}\Omega_{rz} + 2G\left(\frac{\partial v}{\partial z} - \Sigma - D_{zz}^p\right) \quad (12)$$

$$\dot{s}_{rz} = \Omega_{rz}s_{zz} - s_{rr}\Omega_{rz} + 2G\left(\frac{1}{2}\left(\frac{\partial u}{\partial z} + \frac{\partial v}{\partial r}\right) - D_{rz}^p\right) = \Omega_{rz}(s_{zz} - s_{rr}) + 2G\left(\frac{1}{2}\left(\frac{\partial u}{\partial z} + \frac{\partial v}{\partial r}\right) - D_{rz}^p\right) \quad (13)$$

where the spin tensor Ω_{ij} and the volume strain Σ are calculated by following equations.

$$\Omega_{ij} = \frac{1}{2}\left(\frac{\partial u_i}{\partial x_j} - \frac{\partial u_j}{\partial x_i}\right) \quad (14)$$

$$\Sigma = \frac{1}{3}\left(\frac{\partial u}{\partial r} + \frac{u}{r} + \frac{\partial v}{\partial z}\right) \quad (15)$$

The rate of deviatoric stress change follows the first order ordinary differential equation:

$$\dot{s}_{ij} = \dot{s}_{ij,tr} + \dot{s}_{ij,cor} = \Omega_{ik}s_{kj} - s_{ik}\Omega_{kj} + 2G(\bar{D}_{ij} - D_{ij}^p) \quad (16)$$

where each operator is defined as

$$\dot{s}_{ij,tr} = \Omega_{ik} s_{kj} - s_{ik} \Omega_{kj} + 2G\bar{D}_{ij} \quad (17)$$

$$\dot{s}_{ij,cor} = -H : D_{ij}^p = -2G\Lambda N_{ij,tr} \quad (18)$$

When plastic deformation occurs, the plastic strain rate tensor is given by

$$D_{ij}^p = \Lambda \frac{\partial f}{\partial \sigma} = \Lambda N_{ij} \quad (19)$$

$$N_{ij} = \frac{s_{ij}}{\sqrt{s_{kl}s_{kl}}} \quad (20)$$

It is classically determined by expressing so-called consistency condition

$$\dot{f}(\sigma, \sigma_v) = \frac{\partial f}{\partial \sigma} \dot{\sigma} + \frac{\partial f}{\partial \sigma_v} \dot{\sigma}_v = 0 \quad (21)$$

Hardening law is given by

$$\dot{\sigma}_v = \sqrt{\frac{2}{3}} h \Lambda = h \dot{\varepsilon}^p \quad (22)$$

with h which is called the hardening coefficient and corresponds to the slope of the effective stress versus effective plastic strain curve under uniaxial loading conditions.

5.2.2. Level set method

To obtain sharp interface between two different materials, hybrid particle level set method [15] is applied. The motion of the level set follows the equation [16, 17],

$$\frac{\partial \phi}{\partial t} + \vec{V} \cdot \nabla \phi = 0 \quad (23)$$

Here, the interface of each substance is a zero level set $\phi = 0$. $\phi < 0$ indicates inner and $\phi > 0$ indicates outside of the material. This equation is integrated with a 4th order scheme in space and 3rd order Runge-Kutta method in time [18].

While calculating the interface level set function, a drastic change in the material property may give rise to distortion of the interface. To remedy this weakness, a periodic re-initialization is adapted by solving the following equation until steady state is reached.

$$\phi_t + S(\phi)(|\nabla\phi| - 1) = 0 \quad (24)$$

Here S is

$$S = \frac{\phi}{\sqrt{\phi^2 + (1 - |\nabla\phi|)^2} d^2} \quad (25)$$

with d being the grid size.

Basic information like unit normal vector or curvature can be obtained easily using the following relations.

$$\text{Unit normal vector: } \vec{n} = \frac{\nabla\phi}{|\nabla\phi|} \quad (26)$$

$$\text{Curvature: } \kappa = \nabla \cdot \vec{n} = \nabla \cdot \left(\frac{\nabla\phi}{|\nabla\phi|} \right) \quad (27)$$

The dissipation characteristics of ENO scheme and re-initializations of level set lead to interface round off errors and violation of mass conservation. In order to correct these issues for precise interface tracking, a hybrid particle level set method is applied [16, 17]. Here, two types of massless particles, positive and negative particles, are placed in the region of $\phi > 0$ and $\phi < 0$ respectively. These particles are allowed to advect following the equation.

$$\frac{d\vec{x}_p}{dt} = \vec{u}(\vec{x}_p) \quad (28)$$

where \vec{x}_p is the position of the particles and $\vec{u}(\vec{x}_p)$ is their velocity vector. The characteristic information of the flow is preserved due to deletion of the dissipation from the evolution equation. The third order TVD Runge-Kutta method is used to solve the temporal derivative for the evolution equation. Each particle has zero mass but has a volume. The radii of those particles are determined from the size of the grid as such, the maximum and minimum values are

$$r_{\min} = 0.1 \min(\Delta r, \Delta z) \quad (29)$$

$$r_{\max} = 0.5 \min(\Delta r, \Delta z) \quad (30)$$

Initially, the particles are randomly placed and then directed to the correct direction. Then the final radii for particles follow,

$$r_p = \begin{cases} r_{\max} & \text{if } s_p \phi(\vec{x}_p) > r_{\max} \\ s_p \phi(\vec{x}_p) & \text{if } r_{\min} \leq s_p \phi(\vec{x}_p) \leq r_{\max} \\ r_{\min} & \text{if } s_p \phi(\vec{x}_p) < r_{\min} \end{cases} \quad (31)$$

where s_p is the sign of the particle and sets to +1 if $\phi(\bar{x}_p) > 0$ and -1 if $s_p \phi(\bar{x}_p) < 0$, respectively. Here, if an error by the particles to move in the wrong direction with respect to the interface is detected, error correction through the local level set reconstruction is performed.

In well-resolved regions, the interface tracked by level set method is adequately accurate and the particles do not drift farther from the interface. However, in under-resolved regions the calculation of level set generates mass loss and particles escape quietly across the interface. In pure Eulerian based approach, drastic physical phenomena, sometimes, results in level set warping which incurs many numerical problems. One of the major problems is related with level set normal vector determination. In this case, many physical variables calculated based on the information of the orthogonal vector might not converge or even converge into nonphysical values. The correction of the level set value is achieved by comparison of the values from grid based-level set and escaped particles' localized level set. The main idea of level set correction is to eliminate the center grid point around where level set warping occurred. In other words, level set values are artificially designated so that the configuration of the level set has not the form of singularity. This kind of artificial touch is expected to have ignorable effect on the whole physical phenomena if the grid size is sufficiently small. Here, the conservative variables at the center grid point are re-calculated through distance based

interpolation using the same material grid points around the center grid point.

5.2.3. Ghost fluid method

The material properties change drastically across the interface between any two different materials. This is mainly due to the discontinuous entropy distribution at the interface that results in numerical truncation errors, which can be quite significant if not properly treated. In the present method, the ghost cells are populated in the opposite of the real material of interest using the extrapolation while having the continuous entropy distribution. Here, the real discontinuous entropy distribution is merged with the entropy distribution of ghost cells and generates proper boundary conditions. The physical conditions are used in the ghost band where pressure and velocity are the same as the interface conditions. Then the entropy in the ghost band is assigned the value of the real material. All other remaining variables are determined through the entropy relation and the proper EOS [19, 20].

Two nonlinear characteristics intersecting at the interface for system are given as

$$\frac{dp_I}{dt} + \rho_{IL} c_{IL} \frac{du_I}{dt} = 0 \quad \text{along} \quad \frac{dx}{dt} = u_I + c_{IL} \quad (32)$$

$$\frac{dp_I}{dt} - \rho_{IR} c_{IR} \frac{du_I}{dt} = 0 \quad \text{along} \quad \frac{dx}{dt} = u_I - c_{IR} \quad (33)$$

Modified Ghost fluid method follow,

$$u_l = \frac{\rho_l C_l u_l + \rho_r C_r u_r + (p_l - p_r)}{\rho_l C_l + \rho_r C_r} = \frac{w_l u_l + w_r u_r + (p_l - p_r)}{w_l + w_r} \quad (34)$$

$$p_l = \frac{\rho_l C_l p_r + \rho_r C_r p_l + \rho_l C_l \rho_r C_r (u_l - u_r)}{\rho_l C_l + \rho_r C_r} = \frac{w_l p_r + w_r p_l + w_l w_r (u_l - u_r)}{w_l + w_r} \quad (35)$$

5.2.4. Interface conditions

At the interface, velocity components in the normal direction and stress fields must remain continuous following the conservation law as such that

$$\rho_r = \rho_l, \quad u_r = -u_l, \quad p_r = p_l \quad (36)$$

$$u_l = 0, \quad p_l = 2p_l \quad (37)$$

Particle velocity at the surface is zero.

$$\sigma_{nn}^{solid} = -P^{fluid}, \quad \sigma_{nt}^{solid} = 0, \quad v_n^{solid} = v_n^{fluid} \quad (38)$$

5.2.5. Discretization

The third order Runge-Kutta method for time marching is given by

$$u^{n+1} = u^n + \sum_{j=1}^r w_j k_j \quad (39)$$

$$\begin{aligned} & \left[I - \Delta t d_i S \left(u^n + \sum_{j=1}^i c_{ij} k_j \right) \right] k_i \\ & = \Delta t \left[E \left(u^n + \sum_{j=1}^{i-1} b_{ij} k_j \right) + F \left(u^n + \sum_{j=1}^{i-1} b_{ij} k_j \right) \right] \quad (i = 1, \dots, r) \end{aligned} \quad (40)$$

Where the implicit Runge-Kutta coefficients, c_{ij} , are used for integrating the source term and the explicit Runge-Kutta coefficients, b_{ij} , are used for the convective process of the Euler equation where the spatial derivative is replaced by a set of discretized fluxes. The fluxes of a hyperbolic equation will determine the order of spatial accuracy. For a high-order ENO flux construction, a combination of upwind and downwind fluxes are given as

$$f_{j+1/2}^+(u) = \frac{1}{2} (f(u) + \alpha_{j+1/2} u) \quad (41)$$

$$f_{j+1/2}^-(u) = \frac{1}{2} (f(u) - \alpha_{j+1/2} u) \quad (42)$$

where $\alpha_{j+1/2}$ is the largest eigenvalue of the flux Jacobian, and the local Lax-Friedrichs flux is defined as

$$\hat{f}_{j+1/2} = f_{j+1/2}^+(u_j) + f_{j+1/2}^-(u_{j+1}) \quad (43)$$

The control of the time step increment is determined automatically, where the step size is given by

$$\Delta t_{\text{CFL}} = \text{CFL} \frac{\min(\Delta z, \Delta r)}{\max[u + c, u, u - c]} \quad (44)$$

5.2.6. Equation of state

In describing both unreacted and product states of an energetic material, the equations of state defining the pressure are utilized. The Jones-Wilkins-Lee (JWL) form of equations [21] in Eq. (45) and (46) for unreacted reactant and gaseous product of high explosives are used.

$$p_{\text{unreacted}} = A \left(1 - \frac{\omega}{R_1(\rho_0/\rho)} \right) e^{-R_1(\rho_0/\rho)} + B \left(1 - \frac{\omega}{R_2(\rho_0/\rho)} \right) e^{-R_2(\rho_0/\rho)} + \frac{\omega e_0}{(\rho_0/\rho)} \quad (45)$$

$$p_{\text{reacted}} = A e^{-R_1(\rho_0/\rho)} + B e^{-R_2(\rho_0/\rho)} + \frac{C}{(\rho_0/\rho)^{\omega+1}} \quad (46)$$

ρ_0 and ρ are the initial and current densities, respectively. A , B , C , R_1 , and R_2 are the material dependent JWL parameters with ω being the Gruneisen coefficient of the explosive. These parameters are obtained by fitting the JWL EOS to the cylinder expansion test results or thermodynamic equilibrium calculation of CHEETAH [22], where $e_0 = \rho_0 C_v T$ refers to the thermodynamic energy in GPa. In particular, Eq. (46) is an isentropic JWL C-term form of EOS used for gaseous products, and is derived according to the thermodynamics 1st law argument for isentropic process:

$$de = \delta q - \delta w = Tds - pdv = -pdv \quad (47)$$

Integrating Eq. (47) returns the following expression

$$\begin{aligned} e_0 &= -\int pd(\rho_0/\rho) \\ &= \int \left(Ae^{-R_1(\rho_0/\rho)} + Be^{-R_2(\rho_0/\rho)} + \frac{C}{(\rho_0/\rho)^{\omega+1}} \right) d(\rho_0/\rho) \\ &= \frac{A}{R_1} e^{-R_1(\rho_0/\rho)} + \frac{B}{R_2} e^{-R_2(\rho_0/\rho)} + \frac{C}{\omega(\rho_0/\rho)^\omega} \end{aligned} \quad (48)$$

When Eq. (48) is substituted to the JWL EOS in Eq. (45),

$$\begin{aligned}
P_{unreacted|isentropic} = & \\
& A \left(1 - \frac{\omega}{R_1 (\rho_0/\rho)} \right) e^{-R_1 (\rho_0/\rho)} + B \left(1 - \frac{\omega}{R_2 (\rho_0/\rho)} \right) e^{R_2 (\rho_0/\rho)} \\
& + A \frac{\omega}{R_1 (\rho_0/\rho)} e^{R_1 (\rho_0/\rho)} + B \frac{\omega}{R_2 (\rho_0/\rho)} e^{R_2 (\rho_0/\rho)} + \frac{C}{(\rho_0/\rho)^{\omega+1}}
\end{aligned} \tag{49}$$

Thus, the C-term JWL EOS is the isentropic form of the original JWL equation.

The sound speed can be defined as

$$c^2 = \left(\frac{\partial p}{\partial \rho} \right)_s = \left(\frac{\partial p}{\partial \rho} \right)_e + \frac{p}{\rho^2} \left(\frac{\partial p}{\partial e} \right)_\rho \tag{50}$$

Here, the sound speeds for JWL EOSs (unreacted and reacted) are given by

$$\begin{aligned}
c^2_{unreacted} = & -\frac{\rho_0}{\rho^2} \left[A \frac{\omega}{R_1 v^2} e^{-R_1 (\rho_0/\rho)} + B \frac{\omega}{R_2 v^2} e^{-R_2 (\rho_0/\rho)} - \frac{\omega e_0}{(\rho_0/\rho)} \right. \\
& \left. - AR_1 \left(1 - \frac{\omega}{R_1 (\rho_0/\rho)} \right) e^{-R_1 (\rho_0/\rho)} - BR_2 \left(1 - \frac{\omega}{R_2 (\rho_0/\rho)} \right) e^{-R_2 (\rho_0/\rho)} \right] \tag{51}
\end{aligned}$$

$$\begin{aligned}
c^2_{reacted} & \\
= & \frac{\rho_0}{\rho^2} \left[AR_1 e^{-R_1 (\rho_0/\rho)} + BR_2 e^{-R_2 (\rho_0/\rho)} - C \frac{1 + \omega}{(\rho_0/\rho)^{2+\omega}} \right] \tag{52}
\end{aligned}$$

The unreacted and reacted EOS are combined into a single expression, Eq. (53), using the product mass fraction (λ) and reactant depletion ($1-\lambda$).

$$p = (1 - \lambda) p_{unreacted} + \lambda p_{reacted} \quad (53)$$

The combined sound speed is then calculated by using

$$c^2 = (1 - \lambda) c_{unreacted}^2 + \lambda c_{reacted}^2 \quad (54)$$

Meanwhile, thermo-chemical code namely CHEETAH incorporates a fitting program to an optimal parameters of JWL EOS. It works based on the cylinder test data that provide detailed information on the thermodynamic C-J states including pressure, volume, energy, temperature, and detonation velocity. Parameterization of JWL EOS is done by a number of CHEETAH runs to use in the empirical fitting procedure. Table 5.1 shows the C-J conditions for the energetic materials.

Table 5.1 C-J conditions for HNS, HMX, RDX, and BKNO3

	Parameter	HNS	HMX	RDX	BPN
C-J condition	ρ_0 (kg/m ³)	1430	1700	1640	1300
	pressure (GPa)	14.86	27.99	26.55	3.15
	density (GPa)	1.92	2.29	2.22	1.70
	Energy (KJ/cc)	1.90	3.59	3.45	0.37
	Temperature (K)	3638	3549	3574	3932
	Shock velocity (m/s)	6366	8009	7899	3216
	particle velocity (m/s)	1632	2056	2050	753
	sound speed (m/s)	4734	5953	5849	2463
	Gamma	2.90	2.90	2.85	3.27

As for the gap and bulkhead materials, Mie-Grüneisen EOS is adopted to calculate the pressure of non-reactive materials [23] as such,

$$P_{non-reactive} = \Gamma_0 E + \begin{cases} \rho_0 C_0^2 \mu \left[1 + \left(1 - \frac{\Gamma_0}{2} \right) \mu \right] / \left[1 - (S_1 - 1) \mu - S_2 \frac{\mu^2}{\mu + 1} \right]^2 & \text{if } \mu > 0 \\ c_0^2 \rho_0 \mu & \text{if } \mu < 0 \end{cases} \quad (55)$$

where $\mu = \rho/\rho_0 - 1$.

Assuming that $\rho\Gamma = \rho_0\Gamma_0$ so that the sound speed of Mie-Grüneisen EOS is

given by

$$c_{non-reactive}^2 = \rho_0 \Gamma_0 \frac{P - P_0}{\rho^2} + \begin{cases} \frac{\rho_0^2 c_0^2 [\rho + s(\rho - \rho_0)]}{[\rho - s(\rho - \rho_0)]^3} - \Gamma_0 \frac{\rho_0^2 c_0^2 (\rho - \rho_0)}{[\rho - s(\rho - \rho_0)]^3} & \text{if } \rho \geq \rho_0 \\ c_0^2 & \text{otherwise} \end{cases} \quad (56)$$

The Johnson–Cook model is applied for flow stress or the minimum outer force needed to deform plastically. This model makes use of the equivalent plastic strain, strain rate, and melting temperature [24], such that

$$\sigma_Y(\varepsilon_p, \dot{\varepsilon}_p, T) = [A_0 + B_0 \varepsilon_p^n] \left[1 + C_0 \ln \left(\frac{\dot{\varepsilon}_p}{\dot{\varepsilon}_{p0}} \right) \right] \left[1 - \left(\frac{T - T_0}{T_m - T_0} \right)^m \right] \quad (57)$$

where σ_Y is the yield stress and ε_p , $\dot{\varepsilon}_p$, and $\dot{\varepsilon}_{p0}$ are the effective plastic strain, the effective plastic strain rate, and the effective plastic strain rate of the quasi-static state, respectively. The normalized temperature is defined according to reference room temperature, T_0 , and reference melt temperature, T_m . For conditions where $(T - T_0) < 0$, we assume that $m = 1$. The strength model that accounts for the effects of strain hardening, strain-rate hardening, and thermal softening are adopted to describe the dynamic response of the

steel. In addition, the strength model constants, namely, A_0 , B_0 , C_0 , m , and n are used for PMMA, BRASS, and STS. As strain rate approaches zero, the natural log approaches negative infinity, and therefore the Johnson-Cook model sets C_0 to a zero if strain rate reaches a certain minimum value, usually 1 s^{-1} . $\dot{\epsilon}_{p0}$ is commonly set to unity.

The material properties and Mie-Gruneisen EOS constants are summarized in Table 5.2 [23].

Table 5.2 Material properties for PMMA, STS, and BRASS

	Parameter	PMMA	STS	BRASS
Mechanical constant	Initial density (kg/m^3)	1182	7900	8450
	Young's modulus (GPa)	0.42	200	100
	Shear modulus (GPa)	2.32	77	40
Thermal constant	Heat capacity($\text{J/kg}\cdot\text{K}$)	1466	423	380
	Room temperature (K)	300	300	300
	Melt temperature (K)	330.3	1683	1200
Mie-Gruneisen EOS	C_0 (m/s)	2180	4570	3726
	S_0	1.41	1.49	1.43
	Gruneisen coefficient	0.85	1.93	2.04
Johnson-Cook model	A_0 (GPa)	0.76	0.79	0.08
	B_0 (GPa)	0.07	0.51	0.50
	C_0	0.0	0.01	0.29
	m	1.0	1.0	1.0
	n	1.0	0.26	0.61
Strength model	Yield stress (GPa)	0.42	0.34	0.25

5.2.7. Chemical reaction

The reactive flow model is described by the rate law that consists of both ignition and growth terms suggested by Kim et al. [25]

$$\frac{d\lambda}{dt} = I(1 - \lambda)\mu^a + G(1 - \lambda)p^b \quad \mu = \frac{\rho}{\rho_0} - 1 \quad (58)$$

Here p is pressure, t is time, ρ_0 and ρ are the initial and current densities, respectively. Constants I , a , G , b are the unknown parameters and λ is the burned mass fraction. λ represents reaction progress where $\lambda = 0$ is unreacted and $\lambda = 1$ is reacted state. The compression, μ , is defined $\mu = \rho/\rho_0 - 1$. Four unknown parameters of major significance in view of detonation are determined by a series of standardized unconfined rate stick experiment performed [25].

For the RDX, the constants of ignition I and growth G were set at $5.8 \times 10^7 \text{ s}^{-1}$ and $3.8 \times 10^8 \text{ s}^{-1} \text{ Mbar}^{-b}$, respectively. The pressure sensitivity b was 1.1, and the compression sensitivity a was 4.0.

$$\frac{d\lambda}{dt} = I(1 - \lambda)^{0.222} \mu^a + G(1 - \lambda)\lambda^{0.666} p^b \quad (59)$$

The rate law of HMX was modeled by Eq. (59), with the rate parameters of $I = 4.4 \times 10^7 \text{ s}^{-1}$, $a = 4.0$, $G = 8.5 \times 10^8 \text{ s}^{-1} \text{ Mbar}^{-b}$, and $b = 2.0$.

BKNO₃ is a pyrotechnic propellant used for solid fuel igniters, thermites, gas generators, etc. The chemical reaction of BKNO₃ corresponds to deflagration and the reaction rate [26] is calculated as follows.

$$\dot{r} = \sqrt{\frac{Z \cdot e^{-E_a/(\bar{R}T)} \cdot k \cdot \bar{R}T_f^2}{c_p \cdot E_a \cdot (T_f - T_0)}} / \rho_0 \quad (60)$$

Here, the thermal response of BKNO₃ is simulated using the Arrhenius law, and related parameters are quantified by the DSC (Differential Scanning Calorimetry) analysis which measures the calorific heat of chemical reaction. The reaction parameters of BKNO₃ are $Z = 9.2 \times 10^9 \text{ s}^{-1}$, $E_a = 1.8 \times 10^5 \text{ kJ/kmol}$, and $k = 3.2 \times 10^{-3} \text{ kJ/m-sec-K}$. The reaction rate of BKNO₃ with temperature is shown in Fig. 5.1.

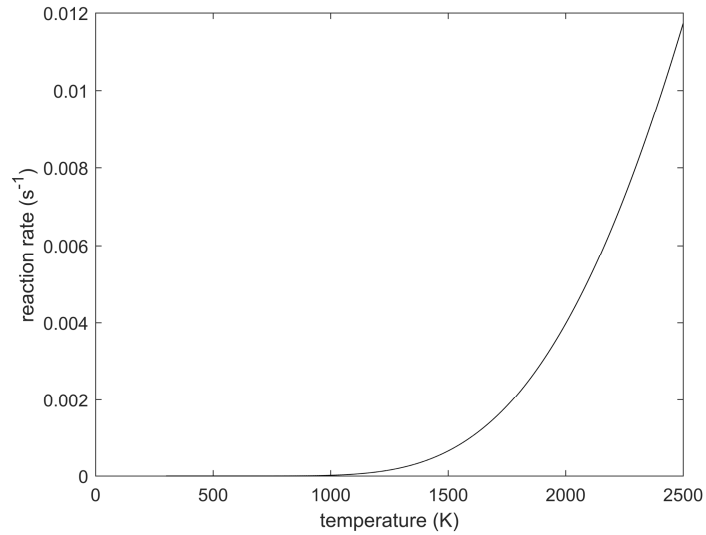


Fig. 5.1 Reaction rate profile for BKNO3's burning based on Arrhenius law with temperature rise.

The rate parameters used in the calculation summarized in Table 5.3. The JWL EOS parameters of product gas of energetic materials are calculated with a thermo-chemical equilibrium code [22].

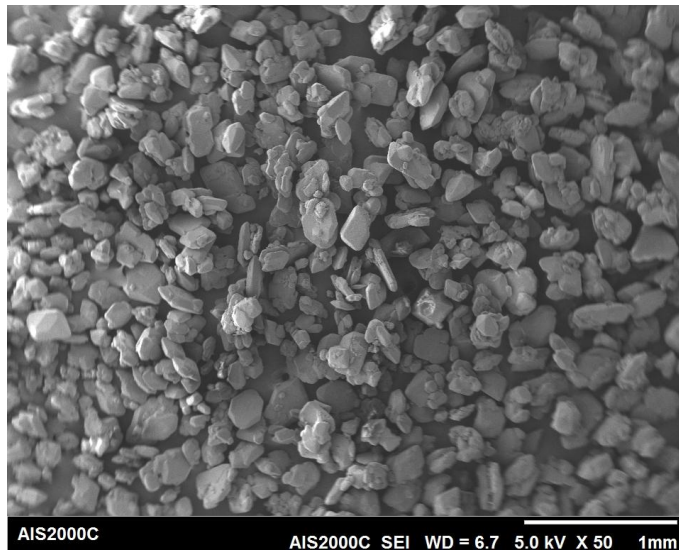
Table 5.3 Modeling constants for HNS, HMX, RDX, and BKNO3

	Parameter	HNS	HMX	RDX	BPN
Reactant	ρ_0 (kg/m ³)	1430	1700	1640	1300
	A (GPa)	-	952200	77810	-
	B (GPa)	-	-5.944	-5.031	-
	R_1	-	14.1	11.3	-
	R_2	-	1.41	1.13	-
	ω	-	0.89	0.89	-
Product	A (GPa)	250.05	333.88	311.19	116.58
	B (GPa)	4.00	5.92	5.69	-0.097
	C (GPa)	1.00	1.35	1.36	0.46
	R_1	4.14	3.63	3.61	4.96
	R_2	1.05	1.02	1.01	0.50
	ω	0.32	0.37	0.36	0.07
Chemical kinetics	I (s ⁻¹)	-	4.4x10 ⁷	5.8x10 ⁷	-
	a	-	4.0	4.0	-
	G (s ⁻¹ Mbar ^{-b})	-	8.5x10 ⁸	3.8x10 ⁸	-
	b	-	2.0	1.1	-
	Z (s ⁻¹)	-	-	-	9.2x10 ⁹
	E_a (kJ/kmol)	-	-	-	1.8x10 ⁵
	k (kJ/m-sec-K)	-	-	-	3.2x10 ⁻³
	p_i (GPa)	-	1.0	1.0	-

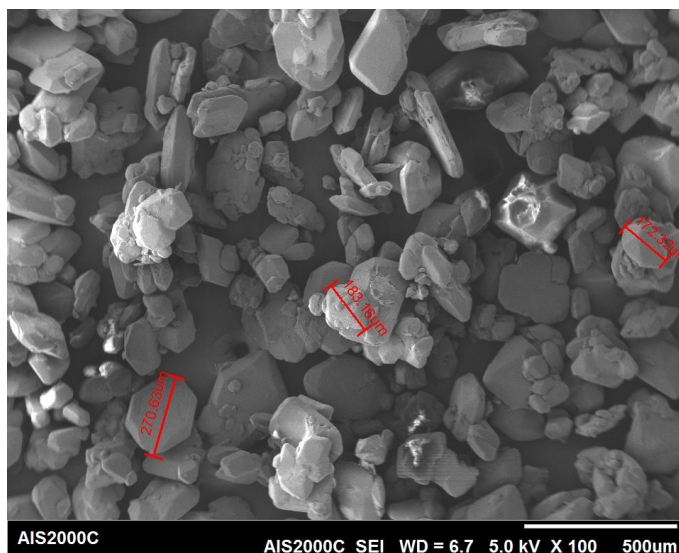
5.3 Results and validations

5.3.1. Small-scale gap test

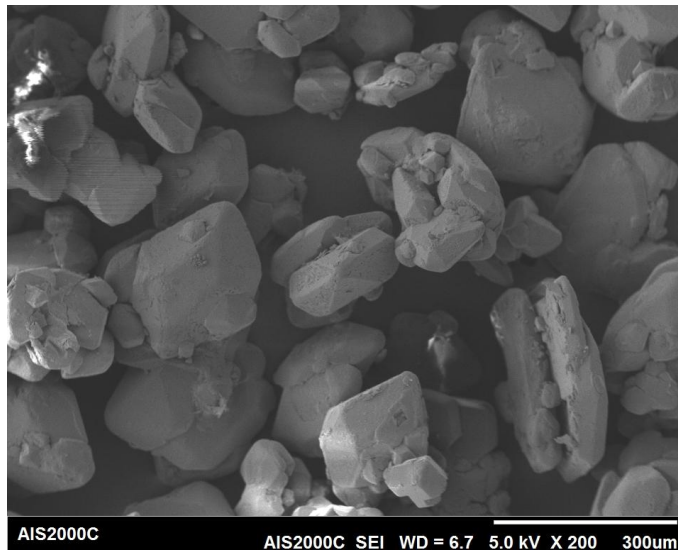
We tested a combination of PMMA gap and RDX explosives to verify the shock sensitivity and attenuation characteristics. The length of gap substance was varied to observe the critical gap thickness until acceptor is detonated in 50% of the trials. The donor charge is RDX whose initial density is 1.57 g/cm^3 , and the acceptor is 97.5% RDX of its initial density 1.64 g/cm^3 . Figure 5.2 shows a SEM image of RDX. The particle diameter ranged from $100 \text{ }\mu\text{m}$ to $500 \text{ }\mu\text{m}$ and the average particle size was about $300 \text{ }\mu\text{m}$ as a result of particle size analysis. It was generally composed of uniform particles. The gap is provided by stacking PMMA discs to adjust its thickness height. All materials were shaped into a 5.11 mm diameter circle confined with 10.145 mm thickness of BRASS metal. The heights of donor and acceptor are 38.1 mm . The gap length was varied. The gap test specimen and configuration are shown in Fig. 5.3. Fifteen trials are conducted at gap thicknesses varied from 9.84 mm to 11.85 mm . Go / No-go criterion is obtained until the witness plate breakage.



(a) 1 mm scale



(b) 500 μm scale



(c) 300 μm scale

Fig. 5.2 SEM images in several length scale for particle size analysis.

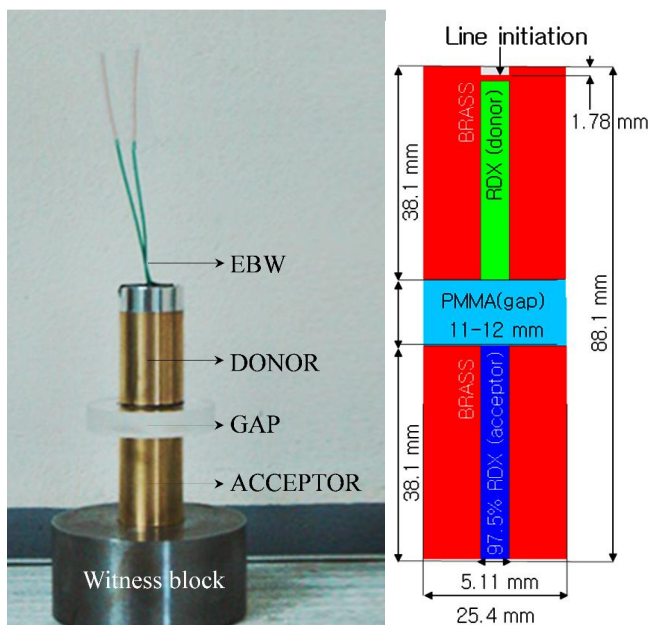


Fig. 5.3 Small scale gap test configuration.



Fig. 5.4 Go (broken) and No-go (preserved) results of small scale gap test.

The confined rod was filled with explosives using a dedicated pneumatic pressure press to homogenize the initial density. Initiation is done by an electronic bridge wire connecting to the center of the upper surface of the donor. The thickness of the attenuator can be reduced by observing alternating positive (Go) and negative (No-go) responses. As the number of trials is increased, the range of gap thickness showing a positive / negative response gradually narrows. A total of 15 tests were carried out to a precision of ± 0.05 mm thickness. A witness plate of mild steel material was installed at the bottom of the acceptor to facilitate the Go / No-go judgment by being broken according to whether or not it was detonated. Table 5.4 lists the SSGT experimental result. From the experiment, the critical thickness was found to be 11.51 mm or 11.56 mm as any thicker value resulted in undamaged witness plate. Therefore, the critical gap thickness of PMMA for the initiation of

97.5% RDX was defined as around 11.5 mm, and the incident pressure delivered to the acceptor can be considered as the minimum value for initiation. Go (broken) and No-go (preserved) results of small scale gap test are shown in Fig. 5.4. If the acceptor charge is initiated by shock to detonate, the BRASS confinement is broken like sample number 1 or 2 on the left side case. Otherwise it is preserved.

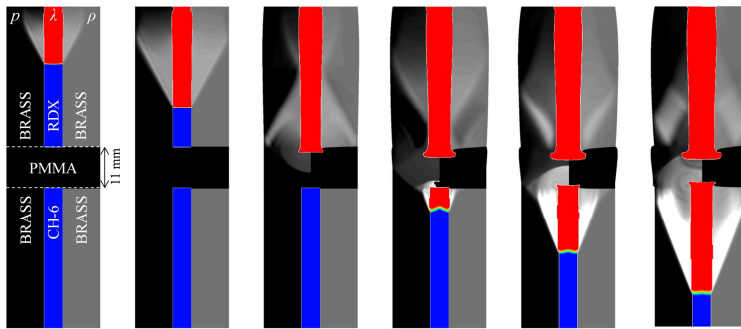
Table 5.4 SSGT experimental result

Exp. num.	PMMA gap thickness	Go / No go
1	9.87 mm	Go
2	11.85 mm	No-go
3	10.71 mm	Go
4	11.34 mm	Go
5	11.40 mm	Go
6	11.56 mm	No-Go
7	11.37 mm	Go
8	11.45 mm	No-go
9	11.41 mm	Go
10	11.44 mm	No-go
11	11.40 mm	Go
12	11.43 mm	Go
13	11.44 mm	Go
14	11.46 mm	Go
15	11.51 mm	Go

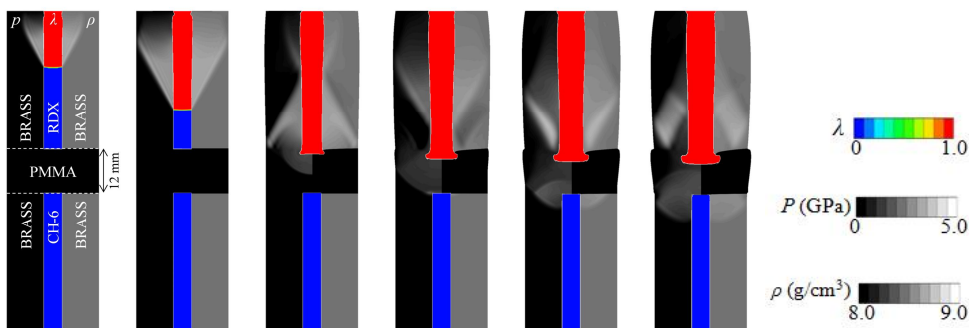
The schematic of the gap test simulation is shown at the right hand side in Fig. 5.3. In order to precisely simulate shock-to-detonation transition and pressure attenuation in the gap test, we constructed a very dense grid system ($h = 0.05$ mm) rather than the reaction zone (~ 0.5 mm) from shock wavefront and the C-J state.

The gap sizes are varied from 10 mm to 12 mm with 1 mm interval. The computational results of Go / No-go response when the shock wave passing through the PMMA of 11 mm and 12 mm thickness reaches the acceptor (97.5% RDX) is shown in Fig. 5.5. The contours are indicated by the reaction progress variable from 0 (reactant) to 1 (product) to distinguish Go / No-go response. The non-reactive materials, PMMA and BRASS, exhibited pressure (left) and density (right) on both sides, respectively, to observe the generation of transmitted and reflected waves. 6 cross sectional views were shown from 2.0 μ s at the initial stage of reaction to 11.0 μ s at which combustion of the acceptor was almost completed. As the explosion proceeds, the pressure of the product gas is applied and the shape of the BRASS changes convexly, but it does not affect the progress of the explosion. As a calculation result, the arrival time of the detonation wave front of the donor reaches to the PMMA after initiation is about 5.0 μ s, and the mean velocity is about 7600 m/s. Transmission and reflection due to the interaction between detonation wave and PMMA occur at 7.0 μ s and 9.0 μ s. The first reflection and transmission are observed when the detonation wave front of the donor reaches the upper

interface of the PMMA. The reflected wave propagates backward, and the transmitted wave enters the PMMA. At this time, the energy loss is converted into a pressure drop. Pressure attenuation occurs through the non-reactive material and the maximum pressure of the shock wave is continuously reduced. A second reflection and transmission occurs when the shock wave impacts the bottom side of the PMMA. Finally, the transmitted wave into the acceptor causes ignition. PMMA and BRASS are deformed as pressure is applied. Various superposition and refraction occur by waves passing through different media.



(a) Go Case at 11 mm PMMA thickness



(b) Nogo Case at 12 mm PMMA thickness

Fig. 5.5 Shown reaction progress for donor (top) and acceptor (bottom), pressure and density for PMMA (middle) and BRASS (both sides). (a) 11 mm Gap and (b) 12 mm Gap at times $t = 2.0, 3.5, 7.0, 9.0, 10.0,$ and $11.0 \mu\text{s}$.

At the PMMA gap thickness of 11 mm, 97.5% RDX is initiated due to the transferred pressure, but at 12 mm, negative reaction is observed because the shock impact lower than the critical initiating pressure reached the acceptor. It was confirmed that the difference in pressure delivered by the gap thickness makes the ignition response different. The attenuating profile of the shock

wave passing through PMMA is shown in Fig. 5.6. The final attenuating pressure at the points corresponding to the gap thickness of 11 mm and 12 mm were calculated to be 1.15 GPa and 0.918 GPa, respectively. Table 5.5 compares the critical initiating pressure and 50% gap thickness derived from the gap test of NOL [10] and LLNL [11]. The critical initiating pressure of 97.5% RDX was obtained at about 1 GPa between 11 mm and 12 mm gap thickness of SSGT in this study, which is consistent with the references. This is the threshold for the minimum pressure required to induce impact ignition on energetic materials. The critical initiating pressure of 97.5% RDX derived from the SSGT test and computational analysis can be quantified to 1 GPa.

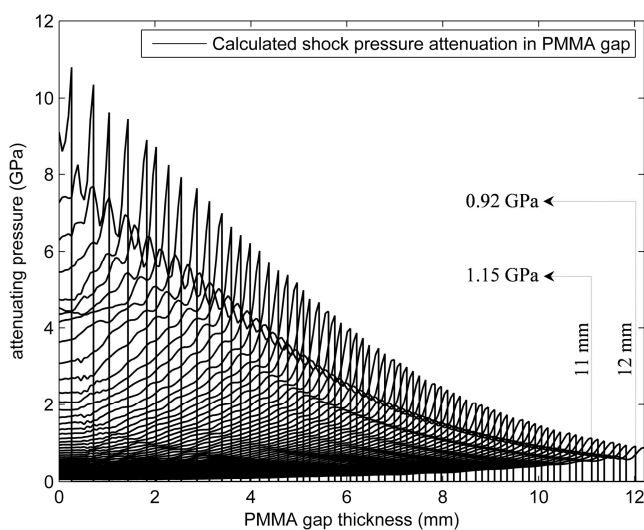


Fig. 5.6 Time trace of attenuating pressure profiles through PMMA gap of SSGT simulation.

Table 5.5 SSGT results for 97.5% RDX [10, 11]

	Threshold pressure (GPa)	50% gap thickness (mm)
NOL SSGT (1996)	-	11.96
NOL LSGT (1966)	0.92	-
LLNL SSGT (2007)	1.05	-
Present SSGT - exp.	-	11.51-11.56
Present SSGT - simul.	0.918-1.15 (1.026)	11.0-12.0 (11.5)

5.3.2. Shock-induced detonation in pyrotechnic device using Al-RDX

A pyrotechnic initiator is a device used to facilitate the ignition of relatively insensitive energetic materials. A detailed schematic of the numerical configuration is illustrated in Fig. 5.7. For bulkhead material, STS-304 with initial density of 7900 kg/m^3 and melting temperature of 1410 K in average was considered. The detonator was comprised of 1430 kg/m^3 HNS (hexanitrostilbene, $\text{C}_{14}\text{H}_6\text{N}_6\text{O}_{12}$), and 1700 kg/m^3 HMX (cyclotetramethylene-tetranitramine, $\text{C}_4\text{H}_8\text{N}_8\text{O}_8$). The initiation of detonator is the onset point of primary detonation. Assuming a high-speed flyer impact, the initiation point was located at the front center of the detonator.

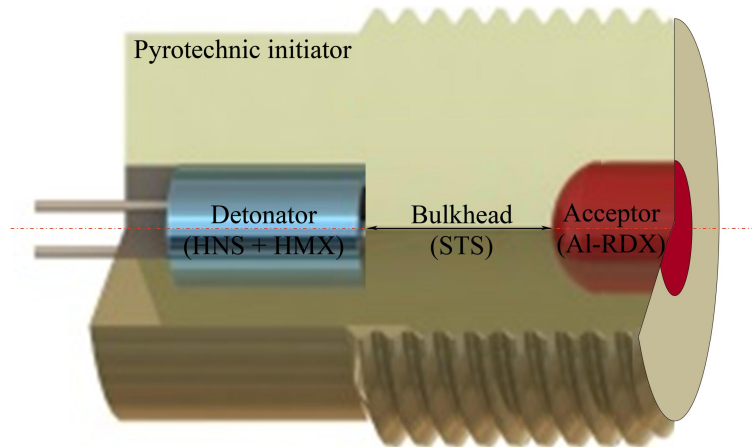


Fig. 5.7 Configuration of an explosive train used in the pyrotechnic initiator (HNS+HMX - STS - Al-RDX).

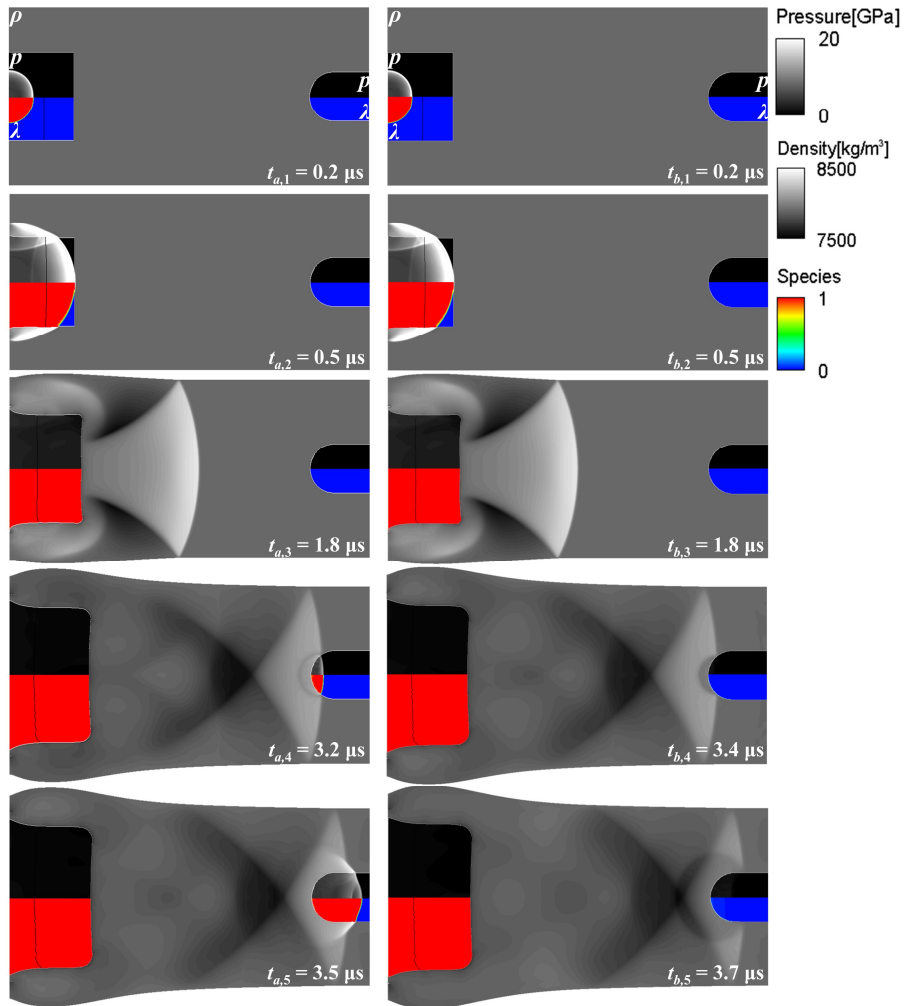
The bulkhead (the gap between the charges) dependence of shock initiation of detonation is shown in Fig. 5.8. A detonator (HNS+HMX) and bulkhead (STS) arrangement was used to transmit the triggering pressure (~ 5.9 GPa) into an acceptor (Al-RDX). The length of the bulkhead was varied, and between 13 mm to 14 mm confirmed the existence of a critical distance. The results determined that 13 mm represented Go while 14 mm was No-go. Also the expanding deformation of the outer contour of the bulkhead assembly is observed in Fig. 5.8 (and Fig. 5.3) in contrast to Fig. 4.5. The pyrotechnic device is a sort of screw-thread and thus the boundaries were confined by STS, while LSGT tests and simulations were entirely unconfined. The mushroom shape of the high pressure area can be observed at $t = 1.0 \sim 3.0 \mu\text{s}$. This interesting feature is generated by interaction between shock and expanding

bulkhead. The backward shock is reflected from the expanding wall and results in fan-shaped rarefactions.

The comparison of Hugoniot curves of STS between the present calculation and experimental data [16] is shown in Fig. 5.9. For pressures up to 45 GPa, our predictions were in good agreement with the experiment.

A closer look at the critical initiation process results in a pressure trajectory shown in Fig. 5.10. The STS bulkhead was operated as an attenuator gap, meaning that a shock stronger than the threshold pressure might result in initiation while a weaker shock will not. The effect of the bulkhead may also be due to shock interaction between non-reactive and reactive materials. It could be used to predict the influence of an acceptor on the initiation in the explosive train configuration. It is important to be able to distinguish cases where detonation is initiated (Go) and those where failure (No-go) occurs depending on bulkhead thickness.

Based on experimental data, the critical PMMA gap thickness was 25.75 mm. Any gap thicker than that resulted in no reactions. Based on LSGT calculations, there is a transition point from Go to No-go between 25 mm and 26 mm of PMMA corresponding to the critical gap thickness. This result was similarly seen in a pyrotechnic initiator case where the transmitted shock wave determines subsequent reaction of Al-RDX.



(a) Go Case at 13 mm gap (b) No-go Case at 14 mm gap

Fig. 5.8 Simulated results for Go and No-go events in a pyrotechnic device.

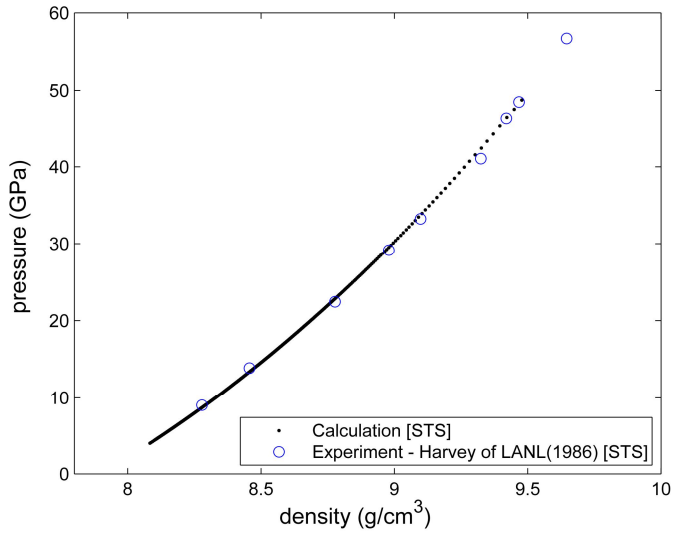


Fig. 5.9 Hugoniot curve for STS-304 in the p - ρ plane from calculation and experiment.

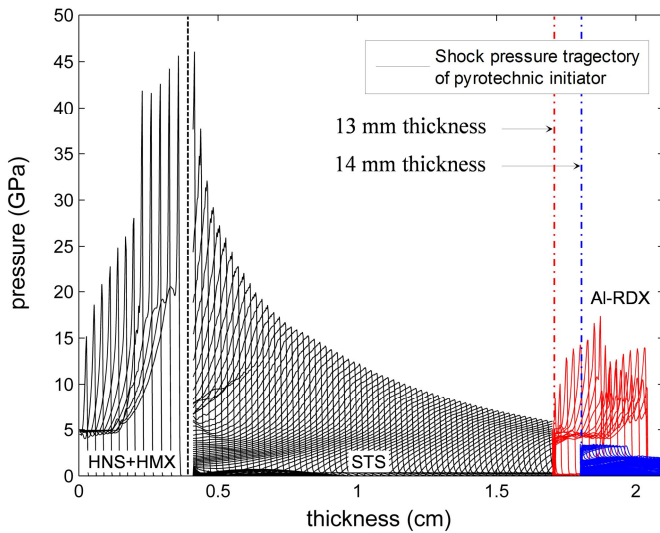


Fig. 5.10 Shock pressure trajectory in detonator-bulkhead-acceptor of pyrotechnic initiator.

5.3.3. Small-scale gap test

The closed bomb test (CBT) provides the measured chamber pressure when BKNO₃ is deflagrated to release hot product gas into a 10 cc purge chamber. Figure 5.11 shows the pyrotechnic initiator-chamber assembly on the left and the computational domain on the right. A threaded screw of the pyrotechnic initiator is fastened into the chamber. The primary layer of donor is HNS (hexanitrostilbene, C₁₄H₆N₆O₁₂, R.E. factor 1.05) with an initial density of 1.43 g/cc. The next layer is a HMX (cyclotetramethylene-tetranitramine, C₄H₈N₈O₈, R.E. factor 1.70) with an initial density of 1.70 g/cc. The electrical flyer initiator of 0.2 mm × 0.2 mm is used to ensure the ignition of the layered donor assembly. Separated by the bulkhead or gap of STS (stainless steel 304, content: C-0.08%, Cr-18%, Ni-8%), acceptor charge is of 97.5% RDX. STS has the advantages of nonmagnetic and processability. Its strength and rigidity are maintained at low temperature environment by heat treatment. The donor-gap-acceptor train configuration is then utilized to ignite BPN (boron potassium nitrate, BKNO₃) of 1.3 g/cc for uniform gas generation into the chamber.

A pressure sensor measures the central wall pressure fluctuation during the event, as the sensor is of the model #102B of PCB piezotronics which is connected to ICP model 484b signal conditioner and receives the voltage signal with a DAQ system. The test was repeated by increasing the bulkhead

thickness in 0.1 mm in order to find the critical condition of the acceptor. The test was carried out from 10 to 16 sets at the point where the Go / No-go reactions were observed alternately.

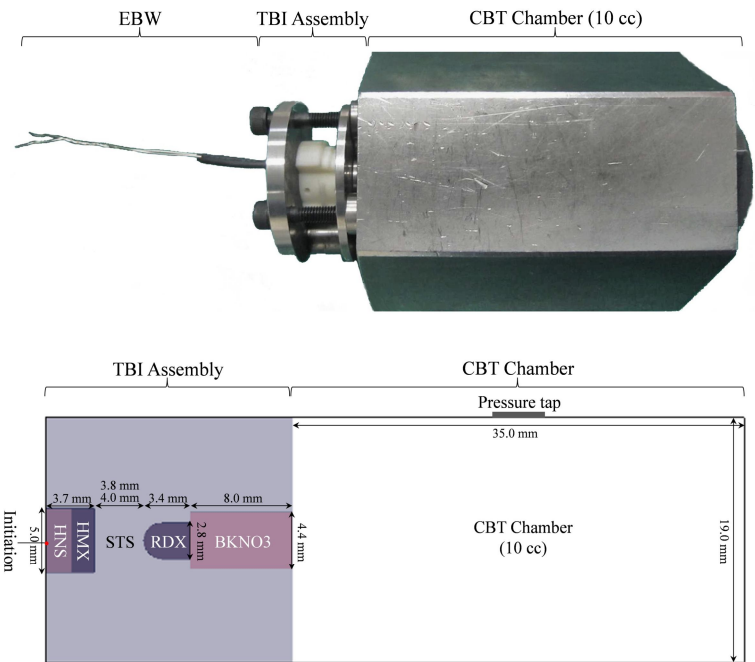


Fig. 5.11 Test specimen (upper) and computational domain (lower) for closed bomb test.

Table 5.6 Closed bomb test result

Exp. num.	STS bulkhead thickness	Go / No go
1	3.2 mm	Go (3)
2	3.4 mm	Go (3)
3	3.6 mm	Go (3)
4	3.8 mm	Go (13) / No-go (3)
5	3.9 mm	Go (2) / No-go (8)
6	4.0 mm	No-go (16)
7	5.0 mm	No-go (3)

Table 5.6 summarizes the results of the CBT explosion test according to the bulkhead thickness. Go / No-go was judged to be a Go response if an increase in pressure was observed but No-go was judged when pressure signal did not increase. The test was repeated three times until 3.7 mm bulkhead thickness showing the Go reaction and more samples were used to ensure the reliability of the result between 3.8 mm and 4.0 mm which showed Go and No-go tendency. A total of 16 trials were performed at 3.8 mm, and 3 trials were No-go. Eight out of 10 were delivered at 3.9 mm. No-go reaction was observed in all samples from 4.0 mm.

Figure 5.12 shows the chamber pressure curves over time at bulkhead thickness of 3.8 mm and 4.0 mm. In the case of the Go reaction, a pressure increase due to the combustion gas injection was observed. The maximum pressure in the 10 cc chamber was increased to about 5 to 6 MPa. In case of

No-go, oscillation due to ignition is observed while maintaining the initial pressure. Therefore, it can be seen that there is an operating critical point of the pyrotechnic device between the bulkhead thickness of 3.8 mm and 4.0 mm. In order to observe the initial reaction of the assembly, the sampling rate was measured for precision up to 2000 μ s at 20 GHz as shown in Fig. 5.13. Raw data and the low-pass filtered pressure measurement are shown. The pressure perturbation is clearly observed in the downstream when the cut-off frequencies $\omega_n = 300$ KHz and $\omega_n = 100$ KHz are applied. The filtered data is derived by the following equation, where τ is the inverse of the cut-off frequency ω_n as a filtering time constant. s and K are respectively a Laplace transform variable and a gain in the passband.

$$\frac{\text{Output}}{\text{Input}} = \frac{Y}{X} = \frac{K}{\tau s + 1} \quad (61)$$

From the results, it can be seen that the combustion gas of BKNO₃ flow into the CBT chamber when the pressure rises at about 100 μ s from the start of the explosion. After 500 μ s, we can observe a swirling flow which seems to be due to the propagation of oscillating reacting waves in the CBT interior space. The FFT results obtained by converting the pressure signal with time into the frequency domain are shown in Fig. 5.14. The observed frequency was about $\omega_c = 8.3$ kHz. This particular frequency is due to the time characteristics of the oscillating flow bouncing inside the chamber.

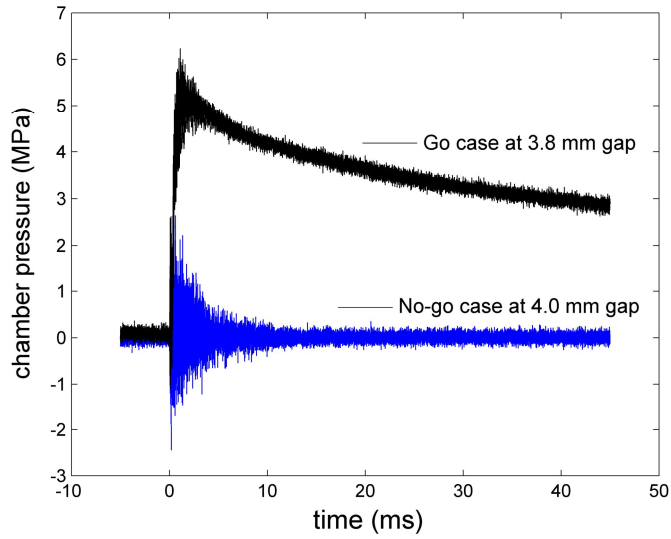


Fig. 5.12 CBT chamber pressure histories for Go / No-go reaction.

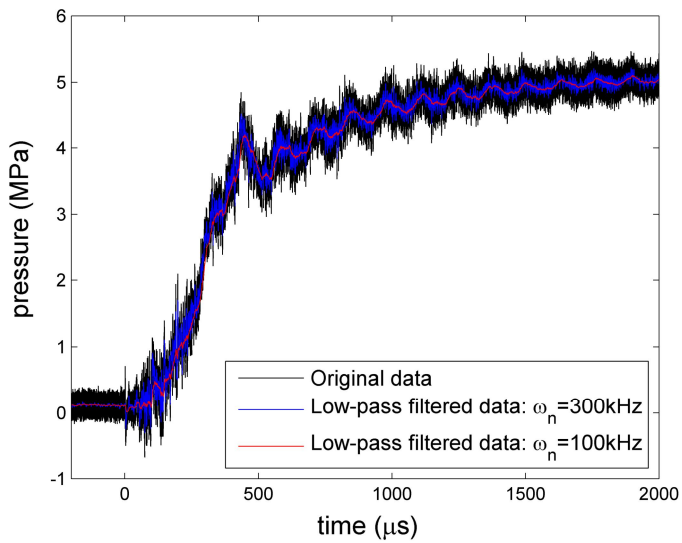


Fig. 5.13 Measured raw and filtered pressure profiles.

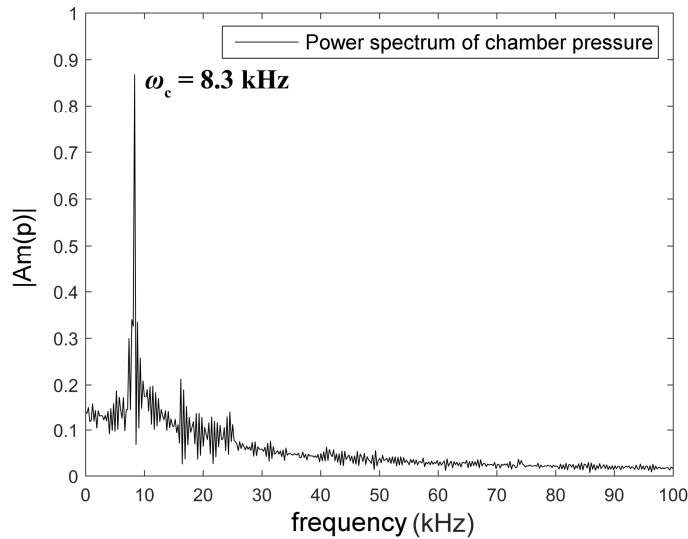


Fig. 5.14 Power spectral densities of closed bomb test data.

Figure 5.15 shows the calculation results on Go / No-go reactions in the explosive train configuration with the bulkhead thickness. In this calculation, bulkhead thicknesses of 3.8 mm and 4.0 mm were considered. This reflects the observation of positive and negative responses at around 3.9 mm in the CBT test. The sequential reaction of the explosives to donor (HNS+HMX) / bulkhead (STS) / acceptor (RDX) occurs by the shock wave propagation. When a high-pressured wave front reaches the acceptor, the chemical reaction is initiated and the thermal energy generated by the reaction supports the propagation of detonation wave. The peak pressure of shock wave is gradually decreased when it passes through the non-reactive material STS because the compression consumes energy. The Go reaction can be observed if the shock

wave with the minimum pressure to ignite the acceptor reaches, otherwise a No-go reaction appears. In the hydrodynamical analysis, the arrival time of the wave front of HNS to HMX was 0.35 μs , and the total burning time of HNS is 0.6 μs . The reaching time of the wave front of HMX to STS was 0.7 μs , and the total burning time of all HMX is 0.8 μs . The pressure wave passing through the STS then reaches the acceptor RDX at 1.7 μs . At this time, a Go (3.8 mm) reaction was obtained when sufficient pressure was applied to acceptor, and a No-go (4.0 mm) reaction was observed. This result is attributed to the pressure attenuation occurring more as the bulkhead thickness increases. The pressure profile along the centerline of the explosive train configuration is shown in Fig. 5.16. The ZND pressure of the donor is about 45 GPa, and the pressure gradually decreases as it passes through the STS bulkhead. The acceptor is initiated or not around 1 GPa. Therefore, the energy loss caused by the shock wave passing through the STS and critical initiating pressure of the high explosive are important factors for determining the operating mechanism of the explosive train configuration or pyrotechnic system.

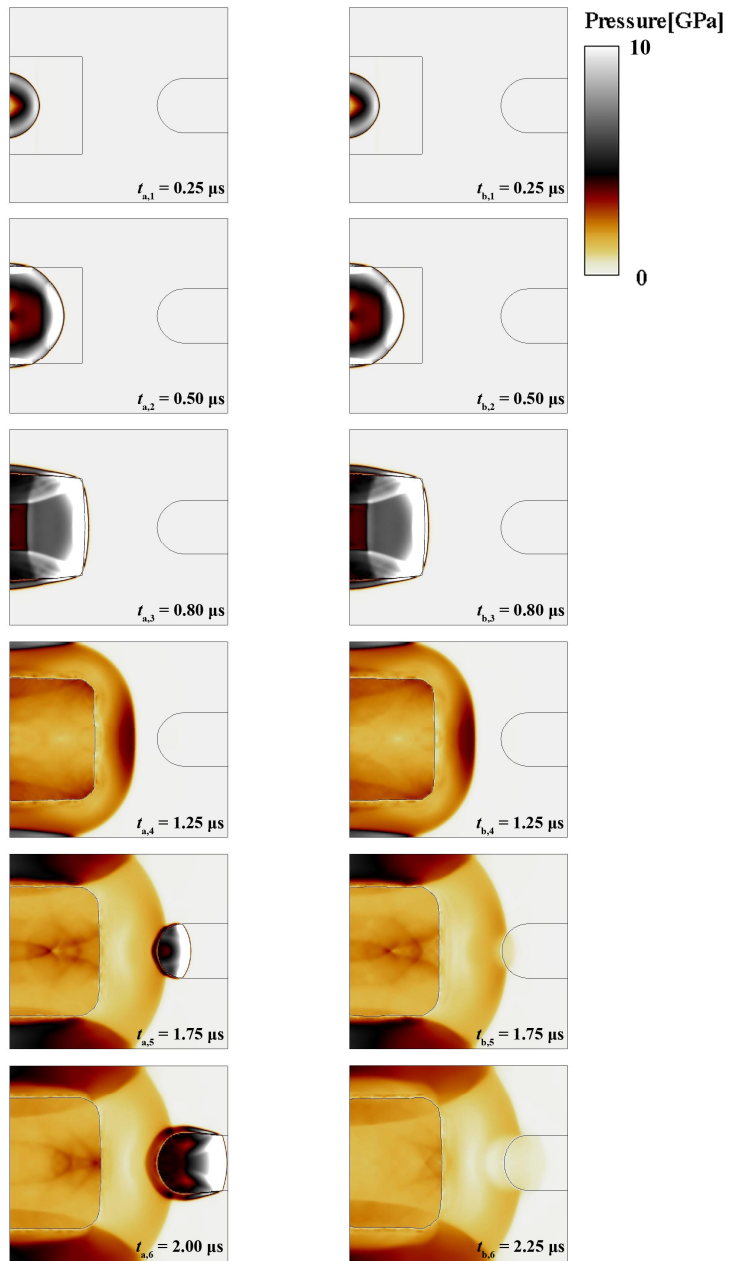


Fig. 5.15 Timed images of pressure contour at 3.8 mm (left), and 4.0 mm (right) bulkhead thickness of the explosive train configuration.

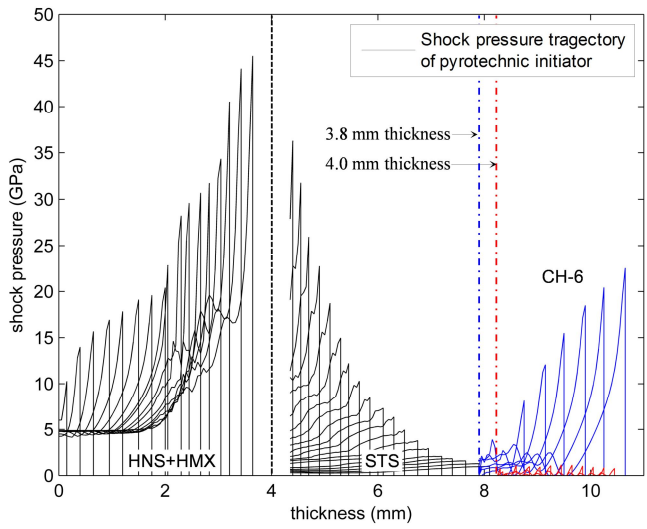


Fig. 5.16 Shock pressure trajectory in donor / bulkhead / acceptor of the explosive train configuration.

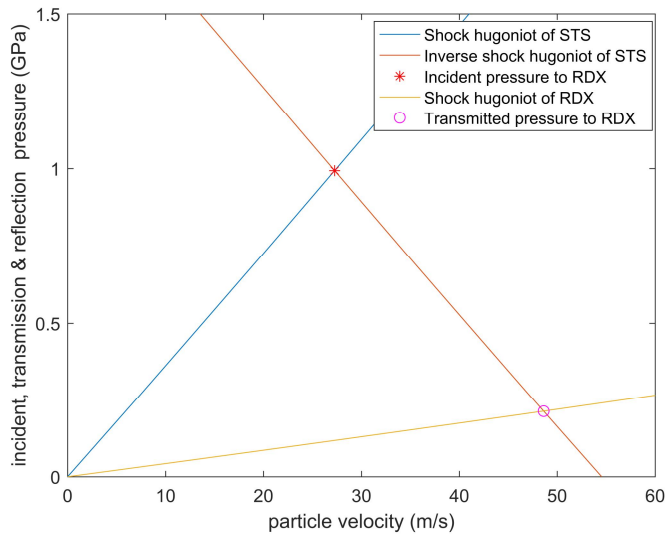


Fig. 5.17 Shock impedance matching of STS and RDX.

When an acoustic wave traveling in one medium encounters the boundary of a second medium, reflected and transmitted waves are generated. The shock impedance is a measure of the amount by which the motion induced by a pressure applied to a surface is impeded. Reflection and transmission of a wave normally incident on the interface between materials with different impedance characteristic. In linearized homentropic planar wave, characteristic shock impedance is defined as the multiplication of density and sound speed in the material. As the wave is propagating from material 1 to material 2, the reflection and transmission is found as follows [27].

$$T = \frac{p_t}{p_i} = \frac{2\rho_2c_2}{\rho_2c_2 + \rho_1c_1} = \frac{Z_2 + Z_1}{Z_2 + Z_1} \quad (62)$$

$$R = \frac{p_r}{p_i} = \frac{\rho_2c_2 - \rho_1c_1}{\rho_2c_2 + \rho_1c_1} = \frac{Z_2 - Z_1}{Z_2 + Z_1} \quad (63)$$

The gap test can be, ideally, regarded as the sequence of two processes. Firstly, wave propagates from reacting energetic material (material 1) to bulkhead material (material 2). And then, wave from bulkhead material (material 2) propagates to unreacted energetic material (material 3). The resulting transmission from this sequence of two transmissions can be reduced by applying eq. (62) twice. The resulting transmission is as follows.

$$T = T_{1 \rightarrow 2} \cdot T_{2 \rightarrow 3} = \frac{2\rho_2 c_2}{\rho_2 c_2 + \rho_1 c_1} \cdot \frac{2\rho_3 c_3}{\rho_3 c_3 + \rho_2 c_2} \quad (64)$$

The shock speed relations are

$$U_{shock} = c_0 + S U_{particle} \quad (65)$$

c_0 and S are bulk sound speed and linear Hugoniot slope coefficient, respectively.

$$S = dU_{shock} / dU_{particle} \quad (66)$$

where the shock velocity is U_{shock} and the material particle velocity is $U_{particle}$. The shock velocity and particle velocity were assumed to follow a linear relationship, and $\rho\Gamma$ was assumed to be a constant.

The impedance matching equation is given by

$$p = \rho_0 (c_0 + S_0 U_{particle}) U_{particle} \quad (67)$$

Figure 5.17 shows shock impedance matching of STS and RDX. The shock Hugoniot parameters of solid state of RDX explosive are $c_0 = 2600$ m/s and S_0

= 1.86. When the incident pressure of 1.0 GPa is applied to RDX acceptor, the transmitted pressure is about 0.2 GPa. Transmission coefficient being the ratio between incident pressure and transmitted pressure is calculated to be 0.2 while reflection coefficient is -0.8.

Figure 5.18 shows that reactive flow motion generated by the pyrotechnic initiator composed of detonator (HNS+HMX) / bulkhead (STS) / acceptor (RDX) / pyrotechnic propellant (BKNO₃) flowed into a 10 cc enclosed chamber. The initiation of energetic materials was derived considering the bulkhead thickness of 3.8 mm.

The explosive train consisting of detonator, bulkhead and acceptor completes its reaction in about 2.0 μ s. Then, another 40 μ s is consumed to fully deflagrate BKNO₃. The hot product gas fills the CBT chamber from about 50 μ s and on.

In the figure, a shadowgraph shown in the upper and pressure is shown in the lower half of each timed image. The release pressure wave into the chamber starts to bounce off of the right-end wall, which is repeating at every 130 μ s. This time characteristic is in striking agreement with the dominant frequency measurement from Fig. 5.14 ($\omega_c = 8.3$ KHz). More intensive analysis is needed to reveal the effect of various types of wave superposition on the combustion field.

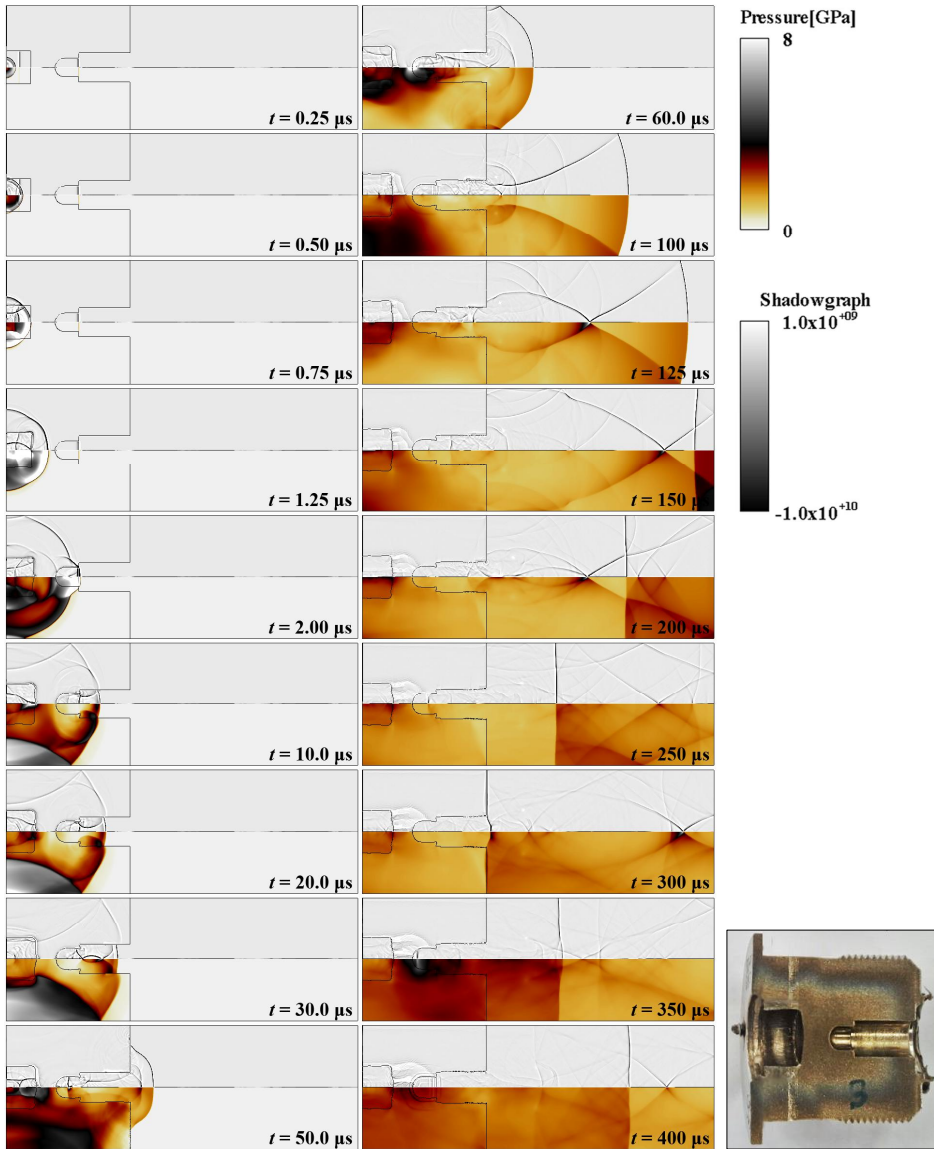


Fig. 5.18 Shown schlieren (top) and pressure (bottom) fields for entire PMD-chamber assembly that shows the detonator (HNS+HMX), bulkhead (STS), acceptor (RDX), and propellant (BKNO₃). Right lower corner is a cross cut of the actual device after single use for comparison with numerical prediction of deformed boundaries.

The shape change of STS bulkhead during the test is quite interesting. As the pressure is attenuated in the bulkhead as such most of the donor pressure is transmitted to the acceptor, causing a higher compression of the gap during successive acceptor initiation. Donor and acceptor expand in all directions due to the internal pressure buildup. A cross sectional view of a cut-off sample after the test is shown at the rightmost bottom in Fig. 5.18. The transmitted shock pressure becomes increasingly high near the central axis of the donor and acceptor due to highly reactive detonation front in the center. The resulting curvature of STS is therefore concave up and it seems to have evolved into a very similar shape between the experiment and calculation. The dynamic shape change of the stainless casing for donor, acceptor, and propellant is also compared between actual photographic image and numerical result from the level-sets. The donor and acceptor cavities are expanded in all directions due to detonation pressure buildup. The resulting curvature of STS cavities is in good agreement with the simulation result as depicted in Fig. 5.19.

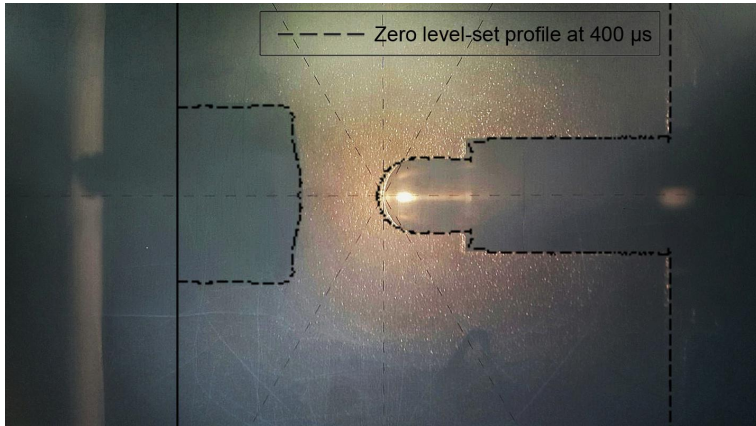


Fig. 5.19 Shape comparison of deformed boundaries of STS with zero level-set lines.

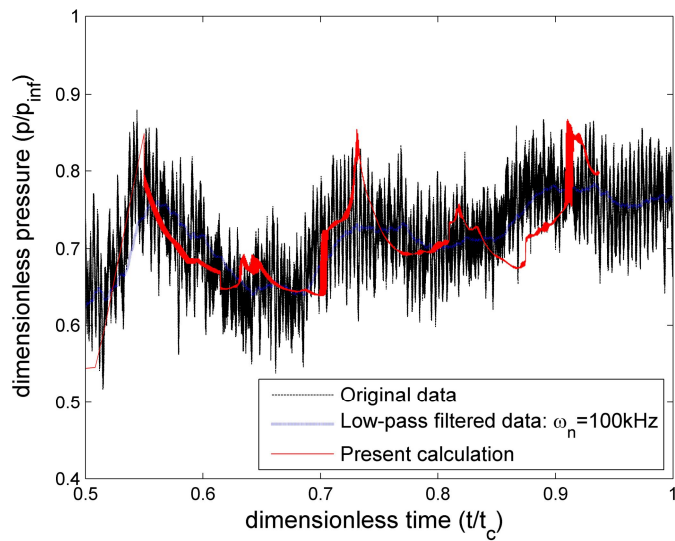


Fig. 5.20 Comparison of pressure fluctuation between test and calculation in closed bomb chamber.

Figure 5.20 shows the comparison of the pressure fluctuation measured from experiment and calculation in the chamber. One can confirm that the periods of the longitudinal wave motion and the periods of the peaks in the chamber match quite well. This means the originality of the acoustic wave is the captured wave inside the chamber, which keep bumping top and bottom side of the chamber to generate acoustic wave toward domain inside.

5.4 Conclusion

In order to analyze the chamber flow of Closed Bomb Test (CBT) using pyrotechnic initiator, a hydrodynamic calculation capable of simulating shock-to-detonation transition and attenuating phenomenon was conducted. We predicted the initiating response of the target explosive by shock loading. The test was performed by connecting the pyrotechnic initiator to a 10 cc chamber. A numerical analysis was used to quantify the critical gap thickness of the small-scale gap test (SSGT). It was found that the shock wave propagation through the explosive train configuration composed of reactive / non-reactive / reactive materials and the interactions between the materials are the important mechanisms for operating the pyrotechnic initiator system. We studied the thermo-physical response of pressure build-up, shock attenuation, and threshold initiating pressure of the explosives. Finally, it was confirmed that combustion gas introduced into the chamber is a major factor causing the

behavior of pressure perturbation with rarefaction waves due to combustion of pyrotechnic propellant (BKNO₃). Since the present methodology for analyzing the energetic component system involving detonation of high explosives, deflagration of propellant, and deformation of confinement system is quite straight forward, one needs to properly implement the outlined formulation into a shock physics code for a state-of-the art full scale hydrodynamic simulation involving such energetic components.

CHAPTER 6

CONCLUSION

A reactive flow model aimed at quantifying the detonation response of energetic materials subjected to an external shock impact is presented. A detailed explanation for determining the free parameters of the model is provided. Two validation experiments are performed using a heavily aluminized RDX. The unconfined rate stick experiment offered detonation velocity as a function of the charge radius. A pressure chamber test offered the time delay between first and subsequent reaction peak. The hydrocode simulation that utilized the present chemical mechanism confirmed that the proposed reactive flow model reproduced the experimental measurements, and it can overcome the limitations set by the earlier reactive flow models.

A sympathetic detonation modeling that involves an explosive donor (PBXN-109), explosive or inert acceptors (sand), and AISI 9260 casing is investigated. The detonation of donor charge and the ensuing responses of nearby acceptors subjected to fragment impact and blast shock waves are simulated by a hydrodynamics with a set of constitutive equations for both reactive and inert components of the system. The modeling approach constructs a hydrodynamic model using the CHEETAH code while the constitutive relations were provided by JWL equation of state, and the

chemical kinetics was elucidated through rate stick simulation. The stochastic failure model based on the Mott probability function is used to describe the fragmentation of steel casing as the impact of blast fragments and strong shock waves give rise to the initiation of acceptor charges. The pressure data and retrieved fragment size distribution from a full size sympathetic detonation test confirm the reliability of the present models.

We have presented a modeling strategy necessary for accurately reproducing the large scale gap test result for characterizing the heavily aluminized RDX. The methodology for such numerical calibration of shock pressure attenuation within the gap is quite straight forward assuming the models are properly implemented and solved in the well-formulated hydrodynamic shock physics code. The present strategy can also accommodate any other type of non-ideal energetic materials (acceptor) subject to a precise characterization.

In order to analyze the chamber flow of closed bomb test (CBT) using pyrotechnic initiator, a hydrodynamic calculation capable of simulating shock-to-detonation transition and attenuating phenomenon was conducted. We predicted the initiating response of the target explosive by shock loading. The test was performed by connecting the pyrotechnic initiator to a 10 cc chamber. A numerical analysis was used to quantify the critical gap thickness of the small-scale gap test (SSGT). It was found that the shock wave propagation through the explosive train configuration composed of reactive /

non-reactive / reactive materials and the interactions between the materials are the important mechanisms for operating the pyrotechnic initiator system. We studied the thermo-physical response of pressure build-up, shock attenuation, and threshold initiating pressure of the explosives. Finally, it was confirmed that combustion gas introduced into the chamber is a major factor causing the behavior of pressure perturbation with rarefaction waves due to combustion of pyrotechnic propellant (BKNO₃). Since the present methodology for analyzing the energetic component system involving detonation of high explosives, deflagration of propellant, and deformation of confinement system is quite straight forward, one needs to properly implement the outlined formulation into a shock physics code for a state-of-the art full scale hydrodynamic simulation involving such energetic components.

REFERENCES

CHAPTER 1

- [1] Lee, E. L. and Tarver, C. M., "Phenomenological model of shock initiation in heterogeneous explosives", *Physics of Fluids*, Vol. 23, No. 12, 1980, pp.2362-2372.
- [2] Souers, P. C., Anderson, S., Mercer, J., McGuire, E. and Vitello, P., "JWL++: A Simple Reactive Flow Code Package for Detonation", *Propellants, Explosives, Pyrotechnics*, Vol. 25, No. 2, 2000, pp.54-58.
- [3] Whitworth, N., "Mathematical and Numerical Modelling of Shock Initiation in Heterogeneous Solid Explosives", PhD Thesis, Cranfield University, 2008.

CHAPTER 2

- [1] Lee, E. L. and Tarver, C. M., "Phenomenological model of shock initiation in heterogeneous explosives", *Physics of Fluids*, Vol. 23, No. 12, 1980, pp.2362-2372.
- [2] Souers, P. C., Anderson, S., Mercer, J., McGuire, E. and Vitello, P., "JWL++: A Simple Reactive Flow Code Package for Detonation", *Propellants, Explosives, Pyrotechnics*, Vol. 25, No. 2, 2000, pp.54-58.
- [3] Souers, P. C. and Vitello, P., "Analytic Model of Reactive Flow", *Propellants, Explosives, Pyrotechnics*, Vol. 30, No. 5, 2005, p.381-385.
- [4] Tarver, C. M., Hallquist, J. O. and Erickson, L. M., "Modeling short pulse duration shock initiation of solid explosives", *Proceedings of the 8th Symposium on Detonation*, 1985, pp.951-961.
- [5] Guilkey, J. E., Harman, T. B. and Banerjee, B., "An Eulerian-Lagrangian Approach for Simulating Explosions of Energetic Devices", *Computers and Structures*, Vol. 85, 2007, pp.660-674.
- [6] Lee, E. L., Hornig, H. C. and Kury, J. W., "Adiabatic Expansion of High Explosive Detonation Products", LLNL, UCRL-50422, 1968, pp.1-21.
- [7] Wackerle, J., Johnson, J. O. and Halleck, P. M., "Shock Initiation of High-Density PETN", *6th Symposium on Detonation*, ACR-221, LA-UR-76-1201, 1976, pp.20-29.
- [8] Wackerle, J., Rabie, R. L., Ginsberg, M. G. and Anderson, A. B., "A Shock Initiation Study of PBX-9404", in *Proceedings of the Symposium on High Dynamic Pressures*, LA-UR-78-1219, 1978, pp.127-139.
- [9] Eyring, H., Powell, R. M., Duffey, G. E. and Parlin, R. B., "The Stability of Detonation", *Chemical Reviews*, Vol. 45, No. 144, 1949, pp.69-181.
- [10] Vitello, P. and Souers, P. C., "The Piece Wise Linear Reactive Flow Rate Model", *Shock Compression of Condensed Matter*, CP845, 2005, pp.507-510.
- [11] Kim, K. and Yoh, J. J., "A particle level-set based Eulerian method for multi-material detonation simulation of high explosive and metal confinements", *Proceeding of the Combustion Institute*, Vol. 34, 2013, pp.2025-2033.
- [12] Souers, P. C., Anderson, S., McGuire, E., Murphy, M. J. and Vitello, P., "Reactive Flow and the Size Effect", *Propellants, Explosives, Pyrotechnics*, Vol. 26, 2001, pp.26-32.
- [13] Yoh, J. J. and Kim, K., "Shock Compression of Condensed Mat

- ter using Eulerian Multi-material Method: Applications to multidimensional shocks, deflagration, detonation, and laser ablation", *Journal of Applied Physics*, Vol. 103, No. 11, 113507, 2008.
- [14] Enright, D., Fedkiw, R., Ferziger, J. and Mitchell, I., "A Hybrid Particle Level Set Method for Improved Interface Capturing", *Journal of Computational Physics*, Vol. 183, No. 1, 2002, pp.83-116.
- [15] Fried, L. E., Howard, W. M. and Souers, P. C., "Cheetah 2.0 User's Manual", UCRL-MA-117541 Rev. 5, Lawrence Livermore National Laboratory, Livermore, CA, USA, 1998.
- [16] Kim, K., Wilson, W., Peiris, S., Needham, C., Watry, C., Ortle, D. and Zhang, F., "Effects of particle damage during detonation of thermobarics on subsequent reactions", *21st International Colloquium on the Dynamics of Explosions and Reactive Systems (ICDERS)*, 2007.
- [17] Loboiko, B. G. and Lubyatinsky, S. N., "Reaction Zones of Detonating Solid Explosives", *Combustion, Explosion and Shock Waves*, Vol. 36, No. 6, 2000, pp.716-733.
- [18] Litzinger, T. A., Lee, Y. and Tang, C. J., "Experimental studies of Nitramine/Azide propellant combustion", *Solid Propellant Chemistry, Combustion, and Motor Interior Ballistics*, Progress in Astronautics and Aeronautics, Vol. 185 (edited by V. Yang, T. B. Brill, and W. -Z. Ren), AIAA, New York, 2000, pp.355-379.
- [19] Balakrishnan, K., Kuhl, A. L., Bell, J. B. and Beckner, V. E., "Ignition of aluminum particle clouds behind reflected shock waves," *23rd International Colloquium on the Dynamics of Explosions and Reactive Systems (ICDERS)*, 2011
- [20] Kuhl, A. L., Bell, J. B. and Beckner, V. E., "Heterogeneous continuum model of aluminum particle combustion in explosions," *Combustion, Explosion, and Shock Waves*, Vol. 46, No. 4, 2010, pp.433-448.

CHAPTER 3

- [1] Victor, A. C., "A Simple Method for Calculating Sympathetic Detonation of Cylindrical, Cased Explosive Charges", *Propellants, Explosives, Pyrotechnics*, 21 (2) (1996) 90-99.
- [2] Lochert, L. J., Franson, M. D. and Hamshere, B. L., "Reduced Sensitivity RDX (RS-RDX) Part II: Sympathetic Reaction", DSTO-TR-1941, AR-013-794, (2006) 1-26.
- [3] Son, G., Park, J. and Kim, S., "A Study on NON-MASS DETONATOR", *Journal of the Korea Society for Explosives and Blasting Engineering*, 9 (2) (1991) 31-36.
- [4] Fisher, S. D., Baker, E. L., Wells, L., Quigley, G. and Lew, A., "XM982 Excalibur Sympathetic Detonation Modeling and Experimentation", *Armament Research Center, IMEMG, Bristol*, (2006) 1-11.
- [5] Chen, L., Wang, C., Feng, C., Lu, F., Lu, J., Wang, X. and Guo, X., "Study on Random Initiation Phenomenon for Sympathetic Detonation of Explosive", *Defence Technology*, 9 (4) (2013) 224-228.
- [6] Benjamin, K. J. and John, S., "Simulating Sympathetic Detonation of 105-mm Artillery Projectiles with CTH", *ARL-TR-1365, ADA326855*, (1997) 1-35.
- [7] Kim, K., Kim, B. and Yoh, J. J., "A particle level-set based Eulerian method for simulating explosively driven metal pipe", *48th AIAA/ASME/SAE/ASEE Joint Propulsion Conference & Exhibit*, (2012) 1-17.
- [8] Lee, E. L., Hornig, H. C. and Kury, J. W., "Adiabatic Expansion of High Explosive Detonation Products", *UCRL-50422, TID-4500*, (1968) 1-21.
- [9] Fried, L. E., Howard, W. M. and Souers, P. C., "Cheetah 2.0 User's Manual", *UCRL-MA-117541 Rev. 5, Lawrence Livermore National Laboratory, Livermore, CA, USA*, (1998).
- [10] Kim, B., Park, J., Lee, K. and Yoh, J. J., "A reactive flow model for heavily aluminized cyclotrimethylene-trinitramine", *Journal of Applied Physics*, 116 (2) (2014) 1-9.
- [11] Guilkey, J. E., Harman, T. B. and Banerjee, B., "An Eulerian-Lagrangian Approach for Simulating Explosions of Energetic Devices", *Computers and Structures*, 85 (2007) 660-674.
- [12] Johnson, G. R. and Cook, W. H., "Fracture characteristics of three metals subjected to various strains, strain rates, temperatures and pressures", *Engineering Fracture Mechanics*, 21 (1) (1985) 31-48.
- [13] Mott, N. F., "Fragmentation of Shell Cases", *Proceedings of the Royal Society of London (A)*, 189 (1018) (1947) 300-308.

CHAPTER 4

- [1] Storm, C. B., Stine, J. R. and Kramer, J. F., “Sensitivity Relationships in Energetic Materials”, in: S.N. Bulusu (Ed.), *Chemistry and Physics of Energetic Materials*; Kluwer Academic Publisher: Dordrecht, 1990, pp. 605-309.
- [2] Kubota, S., Ogata, Y., Wada, Y., Katoh, K., Saburi, T., Yoshida, M. and Nagayama, K., “Observation of shock initiation process in gap test”, *AIP Conference Proceedings*, Vol. 845, 2006, pp. 1085-1088.
- [3] Keshavarz, M. H., Motamedoshariati, H., Pouretedal, H. R., Tehrani, M. K. and Semnani, A., “Prediction of shock sensitivity of explosives based on small-scale gap test”, *Journal of Hazardous Materials*, Vol. 145, 2007, pp. 109-112.
- [4] Macek, A., “Sensitivity of explosives”, *Chemical Reviews*, Vol. 62, No. 1, 1962, pp. 41-63.
- [5] Davies, P. A., “Accidental initiation of condensed phase explosives during road and rail transport”, *Journal of Hazardous Materials*, Vol. 38, 1994, pp. 75-88.
- [6] Kim, K. and Yoh, J.J., “A particle level-set based Eulerian method for multi-material detonation simulation of high explosive and metal confinements”, *Proceedings of the Combustion Institute*, Vol. 34, 2013, pp. 2025-2033.
- [7] Kim, B., Park, J., Lee, K. and Yoh, J. J., “A reactive flow model for heavily aluminized cyclotrimethylene-trinitramine”, *Journal of Applied Physics*, Vol. 116, No. 2, 023512, 2014, pp. 1-9.
- [8] Kim, K. and Yoh, J. J., “Shock compression of condensed matter using multimaterial reactive ghost fluid method”, *Journal of Mathematical Physics*, Vol. 49, 043511, 2008, pp. 1-16.
- [9] Piacesi, D. Jr., “Numerical Hydrodynamic Calculations of the Flow of the Detonation Products from a Point-initiated Explosive Cylinder”, *Naval Ordnance Laboratory, NOLTR-66-150*, 1967, pp. 1-27.
- [10] Souers, P. C., Anderson, S., Mercer, J., McGuire, E. and Vitello, P., “JWL++: A Simple Reactive Flow Code Package for Detonation”, *Propellants, Explosives, Pyrotechnics*, Vol. 25, No. 2, 2000, pp.54-58.
- [11] Steinberg, D. J., “Equation of State and Strength Properties of Selected Materials”, *Lawrence Livermore National Laboratory, UCRL-MA-106439*, 1996, pp.1-7.
- [12] Guilkey, J. E., Harman, T. B. and Banerjee, B., “An Eulerian-Lagrangian approach for simulating explosions of energetic device

- s”, *Computers and Structures*, Vol. 85, 2007, pp. 660-674.
- [13] Kim, B., Park, J. and Yoh, J. J., “Development of new detonation rate model for selective energetic materials”, 24th International Colloquium on the Dynamics of Explosions and Reactive Systems, ICDERS-0155, 2013, pp. 1-6.
- [14] Kim, K., Gwak, M. and Yoh, J. J., “An Enhanced Particle Reseding Algorithm for the Hybrid Particle Level Set Method in Compressible Flows”, *Journal of Scientific Computing*, Vol. 65, 2015, pp. 431-453.
- [15] Eright, D., Fedkiw, R., Ferziger, J. and Mitchell, I., “A Hybrid Particle Level Set Method for Improved Interface Capturing”, *Journal of Computational Physics*, Vol. 83, 1989, pp. 32-78.
- [16] Yoo, S. and Stewart, D. S., “A hybrid level set method for modelling detonation and combustion problems in complex geometries”, *Combustion Theory and Modeling*, Vol. 9, 2005, pp. 219-254.
- [17] Shu, C. W. and Osher, S., “Efficient Implementation of Essentially Non-Oscillatory Shock-Capturing Scheme, II”, *Journal of Computational Physics*, Vol. 83, 1989, pp. 32-78.
- [18] Hu, X. Y. and Khoo, B. C., “An Interface Interaction Method for Compressible Multifluids”, *Journal of Computational Physics*, Vol. 198, 2004, pp. 35-64.
- [19] Fedkiw, R., Aslam, T., Merriman, B. and Osher, S., “A Non-oscillatory Eulerian Approach to Interfaces in Multimaterial Flows (the Ghost Fluid Method)”, *Journal of Computational Physics*, Vol. 152, 1999, pp. 457-492.
- [20] Fried, L. E., Howard, W. M. and Souers, P. C., “Cheetah 2.0 User’s Manual”, UCRL-MA-117541 Rev. 5, Lawrence Livermore National Laboratory, Livermore, 1998.
- [21] Wall, C. and Franson, M., “Validation of a Pressed Pentolite Donor for the Large Scale Gap Test (LGST) at DSTO”, Defence Science and Technology Organisation, DSTO-TN-1172, AR-015-586, 2013, pp. 1-15.
- [22] Bourne, N. K., Cooper, G. A., Burley, S. J., Fung, V. and Hollands, R., “Re-Calibration of the UK Large Scale Gap Test”, *Propellants, Explosives, Pyrotechnics*, Vol. 30, No. 3, 2005, pp. 196-198.
- [23] Erkman, J. O., Edwards, D. J., Clairmont, A. R. and Price, D., “Calibration of the NOL Large Scale Gap Test; Hugoniot Data for Polymethyl Methacrylate”, Naval Ordnance Laboratory, NOLT R-73-15, 1973, pp. 1-65.
- [24] Braithwaite, C. H., Pachman, J., Majzlik, J. and Williamson, D. M., “Recalibration of the Large Scale Gap-Test to a Stress Scale”, *Propellants, Explosives, Pyrotechnics*, Vol. 37, 2012, pp. 614-

620.

- [25] Rienstra, S. W. and Hirschberg, A., “An Introduction to Acoustics”, Eindhoven University of Technology, pp. 65-67, 2012.
- [26] Lawrence E. K., Austin R. F., Alan B. C. and James V. S., “Fundamentals of Acoustics”, 4th Edition, John Wiley & Sons, pp. 149-165, 2009.

CHAPTER 5

- [1] Rider W. J. and Kothe D. B., “Reconstructing Volume Tracking”, *Journal of Computational Physics*, Vol. 141, 1998, pp. 112-152.
- [2] Benson D. J., “Volume of fluid interface reconstruction methods for multi-material problems”, *Applied Mechanics Reviews*, Vol. 55, No. 2, 2002, pp. 151-165.
- [3] Harman T., Guilkey J. E., Kashiwa B. and Schmidt J., “An Eulerian-Lagrangian approach for large deformation fluid structure interaction problems, Part 2: multi-physics simulations within a modern computational framework”, *Transactions on the Built Environment*, Vol. 71, 2004, pp. 1-10.
- [4] Kashiwa B. Lewis M. and Wilson T., “Fluid-structure interaction modeling”, Technical report LA-13111-PR, Los Alamos National Laboratory, 1996.
- [5] Gulikey J. E., Harman T., Xia A. Kashiwa B. and Mcurtry P., “An Eulerian-Lagrangian approach for large deformation fluid structure interaction problems: Algorithm development”, *Proceedings of the Second International Conference on Fluid Structure Interaction*, 2003.
- [6] Guilkey J. E., Harman T. B. and Banergee B., “An Eulerian–Lagrangian approach for simulating explosions of energetic devices”, *Computers and Structures*, Vol. 85, 2007, pp. 660-674.
- [7] Shang M., Xiong Z., Yanping L. and Xu Z., “Simulation of high explosive explosion using adaptive material point method”, *Computer Modeling in Engineering and Sciences*, Vol. 39, No. 2, 2009, pp. 101-124.
- [8] Kim K. and Yoh J. J., “A particle level-set based Eulerian method for multi-material detonation simulation of high explosive and metal confinements”, *Proceedings of the Combustion Institute*, Vol. 34, 2013, pp. 2025-2033.
- [9] Kapahi A., Mousel J., Sambasivan S. and Udaykumar H. S., “Parallel, sharp interface Eulerian approach to high-speed multi-material flows”, *Computers and Fluids*, Vol. 83, 2013, pp. 144-156.
- [10] Price D. and Liddiard T. P., “The Small Scale Gap Test: Calibration and Comparison with the Large Scale Gap Test,” *NOLTR* 66-87, 1966.
- [11] Souers P. C. and Vitello P., “Initiation Pressure Thresholds from

- Three Sources," Propellants, Explosives, Pyrotechnics, Vol. 32, 2007, pp. 288-295.
- [12] Kim B., Park J. and Yoh J. J., "Analysis on shock attenuation in gap test configuration for characterizing energetic materials," Journal of Applied Physics, Vol. 119, 145902, 2016.
- [13] Kim K. and Yoh J. J., "Shock compression of condensed matter using multimaterial reactive ghost fluid method," Journal of Mathematical Physics, Vol. 49, 043511, 2008, pp. 1-16.
- [14] Enright D., Fedkiw R., Ferziger J. and Mitchell I., "A Hybrid Particle Level Set Method for Improved Interface Capturing," Journal of Computational Physics, Vol. 183, No. 1, 2002, pp. 83-116.
- [15] Kim K., Gwak M. and Yoh J. J., "An Enhanced Particle Reseeding Algorithm for the Hybrid Particle Level Set Method in Compressible Flows," Journal of Scientific Computing, Vol. 65, 2015, pp. 431-453.
- [16] Enright D., Fedkiw R., Ferziger J. and Mitchell I., "A Hybrid Particle Level Set Method for Improved Interface Capturing", Journal of Computational Physics, Vol. 83, 1989, pp. 32-78.
- [17] Yoo S. and Stewart D. S., "A hybrid level set method for modelling detonation and combustion problems in complex geometries", Combustion Theory and Modeling, Vol. 9, 2005, pp. 219-254.
- [18] Shu C. W. and Osher S., "Efficient Implementation of Essentially Non-Oscillatory Shock-Capturing Scheme, II", Journal of Computational Physics, Vol. 83, 1989, pp. 32-78.
- [19] Hu X. Y. and Khoo B. C., "An Interface Interaction Method for Compressible Multifluids", Journal of Computational Physics, Vol. 198, 2004, pp. 35-64.
- [20] Fedkiw R., Aslam T., Merriman B. and Osher S., "A Non-oscillatory Eulerian Approach to Interfaces in Multimaterial Flows (the Ghost Fluid Method)", Journal of Computational Physics, Vol. 152, 1999, pp. 457-492.
- [21] Souers P. C., Anderson S., Mercer J., McGuire E. and Vitello P., "JWL++: A Simple Reactive Flow Code Package for Detonation", Propellants, Explosives, Pyrotechnics, Vol. 25, No. 2, 2000, pp. 54-58.
- [22] Fried L. E., Howard W. M. and Souers P. C., "Cheetah 2.0 User's Manual", UCRL-MA-117541 Rev. 5, Lawrence Livermore National Laboratory, Livermore, 1998.
- [23] Steinberg D. J., "Equation of State and Strength Properties of

- Selected Materials”, Lawrence Livermore National Laboratory, UCRL-MA-106439, 1996.
- [24] Johnson G. R. and Cook W. H., “Fracture characteristics of three metals subjected to various strains, strain rates, temperatures and pressures”, *Engineering Fracture Mechanics*, Vol. 21, No. 1, 1985, pp. 31-48.
- [25] Kim B., Park J., Lee K. and Yoh J. J., “A reactive flow model for heavily aluminized cyclotrimethylene-trinitramine”, *Journal of Applied Physics*, Vol. 116, No. 2, 023512, 2014, pp. 1-9.
- [26] Lee H. S., "Ignition Delay Investigation in a Pyrotechnic Cartridge with Loosely-Packed Propellant Grains", 45th AIAA/ASME/SAE/ASEE Joint Propulsion Conference & Exhibit, AIAA 2009-5191, pp. 1-11.
- [27] Lawrence E. K., Austin R. F., Alan B. C. and James V. S., “Fundamentals of Acoustics”, 4th Edition, John Wiley & Sons, 2009, pp. 149-165.

초 록

충격파에 의한 고에너지 물질의 폭발 현상은 매우 짧은 시간 (~ μsec) 안에 폭굉으로 천이되므로 정확한 반응속도를 예측하는 것이 중요하다. 본 연구에서는 충격에 의한 화약의 폭발 현상을 해석하기 위하여 반응 개시항(ignition term)과 폭발 성장항(growth term)으로 구성된 압력기반의 반응속도모델(detonation model)을 사용하여, 35%의 알루미늄이 함유된 RDX 화약의 크기효과 특성을 규명하고자 하였다. 또한 원통형으로 제작된 화약의 반경에 따른 폭굉파의 전파속도 변화 거동을 정의하기 위하여 비구속 반응 스틱에 대한 실험 및 2차원 오일러리안 수치해석을 수행하였다. 계산 결과에 따르면, 폭발파가 가속되는 조주구간 이후 압력의 정상상태 하에서 측정된 폭굉 파속(detonation velocity)이 알루미늄 함유 RDX 화약의 이론 및 실험 데이터와 잘 일치하는 것으로 나타났다.

하나의 탄약이 폭발하였을 경우 에너지가 다른 탄약으로 전달되어 폭발을 야기해 최종적으로 연쇄적인 폭발에 이를 수 있다. PBXN-109(64% RDX, 20% Al, 16% HTPB)가 충전된 155 mm 고폭탄의 동조폭발에 대한 2차원 하이드로 시뮬레이션을 수행하여 여폭약과 수폭약간 거리 및 중간 완충제에 따른 순폭 여부를 예측하였다. 계산 결과, 가까운 거리의 화약 간 순폭은 충격 점화로 인해 발생하며, 상대적으로 먼 거리의 경우에는 케이스의 파손으로 발생한 파편과의 충돌이 주요 원인으로 나타났다. 완충제는 폭굉파와 파편의 효과를 억제하여 동조폭발의 발생 확률을 낮출 수 있는 것으로 예측되었다.

감쇠기를 사이에 두고 여폭약과 수폭약으로 충전된 파이프를 착화

기는 격벽의 압력 감쇠 현상과 고에너지 물질의 충격 점화 특성을 갖는다. 고폭약의 폭굉 반응 및 비반응 물질 통과에의 폭압 감쇠와 더불어 격벽의 형상 변화를 모사하기 위해서는 충격 전달에 의한 gap test의 폭굉 모델링이 필요하다. 오일러리안 레벨셋 기법이 적용된 다중물질 하이드로 코드를 사용하여 pentolite 작약과 열폭압 RDX의 폭발 반응 및 PMMA gap을 통과하는 충격과 전달을 해석함으로써 화약-격벽간 상호작용 및 임계 두께, 음향 임피던스, Go / No-go 기폭 점화에 대한 특성을 정량화하였다.

파이로테크닉 착화기의 CBT(Closed Bomb Test) 챔버 연소 유동을 해석하기 위하여 고폭약의 반응 및 비반응 물질의 압력 감쇠 현상을 연동하여 모사할 수 있는 하이드로다이나믹 해석을 수행하였다. 소량의 시약으로 기폭 판단이 가능한 SSGT의 시험 및 전산모사를 수행하여 97.5% RDX로 구성된 수폭약의 충격에 대한 점화 민감도를 정량화하였다. 파이로테크닉 착화기를 형상화 한 여폭약(HNS+HMX) / 격벽(STS) / 수폭약(RDX)으로 구성된 TBI 화약 트레인을 고려하여 충격과 전달을 해석함으로써 반응 및 비반응 물질 간 상호작용에 의한 임계 격벽 두께 및 기폭 압력 간의 관계를 규명하고, 소형 파이로 착화기의 작동특성을 검증하였다. 여폭약(HNS+HMX) / 격벽(STS) / 수폭약(RDX) / 파이로추진제(BKNO₃)로 구성된 화약 트레인의 기폭으로 발생하는 연소 유동이 10 cc 체적의 밀폐형 챔버 내부로 유입되었을 때의 압력을 측정함으로써 충격과 저밀도과의 상호작용에 의한 진동 유동의 물리적 특성을 규명하고자 하였다. 반응 유동장의 폭압과 반응과의 전파를 근거로 시간 특성을 갖고 나타나는 압력 요동(fluctuation)을 검증하고, 특정 진동수로 떨리는 챔버 연소 유동의 주파수 특성을 파악하였다.

주요어: 하이드로다이나믹 해석, 충격-폭발 천이 현상, 고에너지
물질, 파이로테크닉 연소, 반응속도모델, 충격 민감도
학 번: 2012-30168